Raman study of multiferroic $EuTiO_3$

Panagiotis Pappas

March 10, 2015

Dedicated to my parents

Abstract

Multiferroics are a class of materials that combine two or more types of ordering in the same system. The underlying physics of these phenomena is very interesting as they are induced from a combination of two or more correlated order parameters. Multiferroics are promising candidates for many technological applications with emphasis in microelectronic devices and memories. In this thesis we present a Raman study of the perovskite $EuTiO_3$. $EuTiO_3$ is believed to be a multiferroic and also a quantum paraelectric. Quantum paraelectrics are characteristic materials which despite the fact that they have lattice instabilities (and a soft mode), which drives them to ferroelectricity, the quantum fluctuations at low temperatures (near 0 K) do not allow them to reach ferroelectricity and the soft mode saturates in a non zero value. It is obvious that those systems are of great interest as the quantum fluctuations dominate their behavior under certain conditions. Europium titanate resembles strontium titanate, which is a very well studied quantum paraelectric in many of its properties. This fact gave the initial hint that a material such as $EuTiO_3$ would have all the interesting properties of a quantum paraelectric. Besides the fact that it has magnetic anions would introduce a multiferroic nature in the same system. Until now there has been a lot of research on the antiferrodistortive phase transition that seems to be present at $\sim$ 200 K. The fact that at room temperature europium titanate is in a cubic phase gave no Raman active modes, so until now its Raman spectrum has not been presented nor did the Raman spectrum of its lower apparently tetragonal symmetry phase. In this thesis we induced a symmetry lowering with various methods such as application of electric field, lowering of the temperature and high pressure in order to observe the Raman spectrum. The Raman spectrum can give us better insight to the structure and phase dynamics of this material under various conditions.

Acknowledgments

I would like to thank Prof. E.Liarokapis who was keen to supervise me. I cannot express enough how i benefited from his scientific ideas, guidance and unique approaches to physics. I would like to thank Prof. L.Tsetseris and Prof. I.Raptis, who were co-supervising, for their helpful comments and ideas on my thesis. Also i would like to thank Dr.E.Siranidi for her great help during my first days to the lab. Last but not least i would like to thank all my friends for their great support and company all these years.

Contents

1 Raman scattering **4**
- 1.1 Electromagnetic radiation 4
  - 1.1.1 Multipole moments 5
  - 1.1.2 Some aspects of the interaction of electromagnetic radiation and matter 8
- 1.2 Formulation of the scattering tensor 9
  - 1.2.1 The scattering tensor 12
  - 1.2.2 Symmetry of the scattering tensor 15
- 1.3 The scattering operator 16
  - 1.3.1 Symmetry considerations 17

2 Ferroelectricity **19**
- 2.1 Introduction 19
- 2.2 Phenomenological approach to ferroelectricity 20
  - 2.2.1 Coupling of stress and spontaneous polarization 23
  - 2.2.2 Deviation from perfect polarization 25
  - 2.2.3 Lattice instabilities and ferroelectricity 27
  - 2.2.4 More about soft modes 28
  - 2.2.5 Some aspects of quantum criticallity in ferroelectrics . 30

3 What is a Multiferroic material? **32**
- 3.1 Introduction 32
  - 3.1.1 Type I multiferroics 33
  - 3.1.2 Type II mulriferroics 35

4 Review of the material **37**
- 4.1 Crystallographic structure 37
- 4.2 Magnetic and dielectric properties 38
  - 4.2.1 Magnetic properties 38
  - 4.2.2 Dielectric properties 42
- 4.3 Structural phase transition 44

4.4 Spin-lattice coupling 56

5 Experimental methods **62**
5.1 Experimetal apparatus 62
5.2 Direct current apparatus 66
5.3 High electric field measurements 68

6 Results and discussion **73**
6.1 The sample 73
6.2 Intrinsic spectrum and first efforts 73
6.3 High voltage measurements 75
6.4 Discussion 93
6.5 Conclusions 95

Chapter 1

Raman scattering

1.1 Electromagnetic radiation

According to the classical theory of electromagnetic radiation the intensity per second radiated by an oscillating dipole is:

$$I = \frac{2}{3c^2}\ \bar{\ddot{M}}^2 \tag{1.1}$$

where $\bar{\ddot{M}}^2$ is the time average of the second derivative of the dipole moment. The total intensity is considered as the power radiated from the dipole in all space directions and is averaged over all dipoles if we have more than one oscillating dipole.

Let us now assume that we have a plane polarized electromagnetic wave with frequency f_0 traveling along the x-axis

$$\mathbf{E} = \mathbf{E}_z = E_0 \cos(2\pi f_0 t - x/c) \tag{1.2}$$

We assume that the electric field induces an oscillating dipole moment such as

$$M = \alpha E_0 \cos(2\pi f_0 t - x/t) \tag{1.3}$$

and so

$$\ddot{M}^2 = 16\pi^4 f_0^4 \alpha^2 E_0^2 \cos^2(2\pi f_0 t - x/c) \tag{1.4}$$

$$\bar{\ddot{M}}^2 = 8\pi^4 f_0^4 \alpha^2 E_0^2 \tag{1.5}$$

Combining (1.1),(1.5) we obtain the total intensity of the radiation emitted

$$I = \frac{16\pi^4 f_0^4}{3c^3} \alpha^2 E_0^2 \tag{1.6}$$

If we integrate with respect to the solid angle of 4π radians we obtain

$$I = \frac{128\pi^5 f_0^4}{3c^4}\alpha^2 I_0 \tag{1.7}$$

where I_0 is the radiation density for a linear polarized electromagnetic wave

$$I_0 = \frac{c}{4\pi}E_z^2 = \frac{c}{8\pi}E_0^2 \tag{1.8}$$

The radiation field produced by a dipole is being perceived as the consequence of an accelerating charge if we consider Maxwell's equations. For example if we assume a harmonically oscillating positive and negative charge with frequency ω the dipole moment is $\mathbf{p} = e\mathbf{r} = \mathbf{p}_0\cos(\omega t)$ where $\mathbf{r}$ is the distance between the two charges. The absolute values of the corresponding electric and magnetic field is

$$|E| = |H| = \frac{\omega^2}{r_0 c^2}p\sin(\theta) \tag{1.9}$$

It is obvious that at a 90^0 angle of the axis of the dipole the electric field (and the magnetic) is maximum and consequently parallel to the axis of the dipole no radiation is emitted. The energy density of the electromagnetic field is:

$$\varrho = \frac{1}{4\pi}\frac{\omega^4}{r_0^2 c^4}p^2\sin^2(\theta) \tag{1.10}$$

Another way of expressing the electromagnetic flux in a given direction, which corresponds to an angle θ is $I(\theta) = \varrho c$. By substituting to (1.10) we have

$$I(\theta) = \frac{\omega^4 p^2}{4\pi r_0^2 c^3}\sin^2(\theta) \tag{1.11}$$

By integrating (1.11) over a sphere with radius ρ_0 we obtain

$$I = \frac{\omega^4 p^2}{3c^3} \tag{1.12}$$

Equations (1.12) and (1.6) are identical if we substitute to the latest αE_0 with $p = p_0 cos(\omega t)$

1.1.1 Multipole moments

When studying the scattering of electromagnetic radiation by atoms or molecules, the induced dipole moment (discussed in the previous section)

plays a crucial role, but there are some cases where electric moments from clusters of more than two electric charges take place and so one must take into account higher order (electric or magnetic) moments. The multipole expansion of the potential is given by the well known formula

$$V = \frac{A_0}{r} + \frac{1}{r^2}(A_{1x}p_x + A_{1y}p_y + A_{1z}p_z)$$
$$+\frac{1}{r^3}(A_{2xy}d_{xy} + A_{2z^2}d_{z^2} + A_{2xz}d_{xz} + A_{2yz}d_{yz} + A_{2(x^2-y^2)}d_{x^2-y2})$$
$$+\frac{1}{r^4}(4forbitals) \quad (1.13)$$

We have chosen this form of representing the multipole expansion because it gives a good idea of what is the nature of each term and also presents very clearly the spatial analogy of each term with the atomic orbitals. Specifically the first term is the electric monopole, which has the spatial distribution of an s-orbital, the second term is the electric dipole with a p-orbital spatial distribution and the third term is the quadrupole which has a d-orbital spatial distribution. It is obvious that the dipole moment has vector properties, whereas the quadrupole moment is a tensor. The importance of higher order electric multipoles is rather low in the examination of light scattering effects. On the contrary, it is not rare to encounter magnetic dipole moment contributions in light scattering processes.

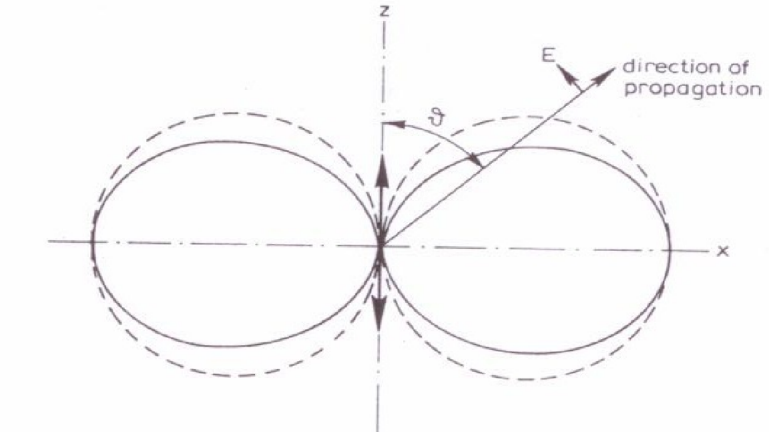

Figure 1.1: The spatial distribution of the radiation intensity and amplitude of a dipole [1]

The origin of a magnetic dipole moment is an electric current and particularly in our case this current comes from the orbital moment of electrons in atoms. If we imagine the movement of electrons in their orbitals as a

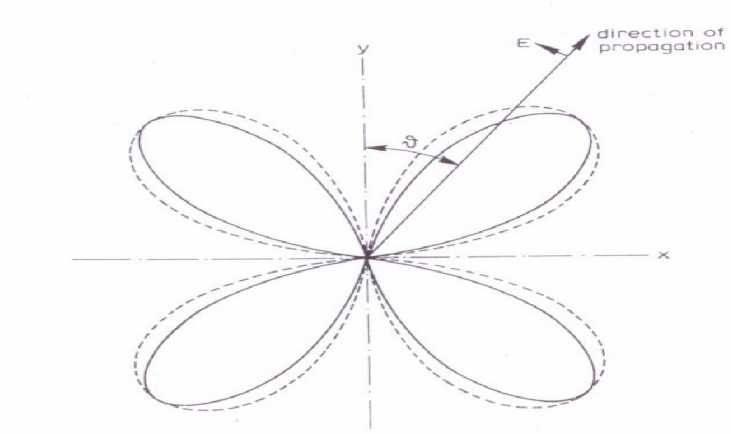

Figure 1.2: The spatial distribution of the radiation intensity and amplitude of a quadrupole

current passing through a ring, we obtain $|\mu| = \pi I \frac{\alpha^2}{c}$ for the magnetic dipole moment where α is the radius of the ring and I is the current. For an electron with mass m_e moving in the ring with velocity v the momentum is $\mathbf{M} = m_e v \alpha = \sqrt{l(l+1)}\hbar$. The corresponding current is $I = \frac{-ev}{2\pi\alpha}$ and so the magnetic moment would be $|\mu| = \frac{-ev\alpha}{2c}$. By combining the expressions for

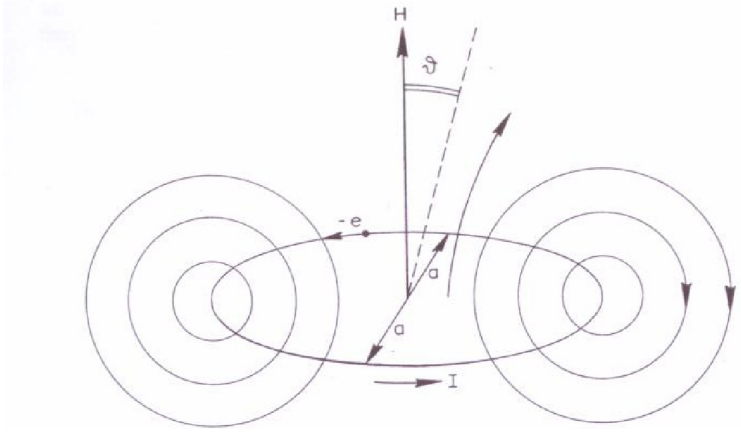

Figure 1.3: The spatial distribution of the radiation intensity and amplitude of a magnetic dipole

the momentum and the magnetic dipole moment we obtain

$$|\mu| = \frac{-e\hbar}{2m_e c}\sqrt{l(l+1)} = \frac{-e}{2m_e c}\mathbf{M} \tag{1.14}$$

Because of the negative sign of the electrons charge, the angular momentum

and the magnetic moment are antiparallel and both perpendicular to the "ring" as shown in the figure. Now let us assume as before that we have an oscillating dipole, which of course will emit electromagnetic radiation. In our case the electron following the orbit has displacement $x = x_0 \cos(2\pi f_0 t)$ and velocity $\upsilon = -2\pi f_0 x_0 \sin(2\pi f_0 t)$ The spatial distribution of the field (electric and magnetic) is easily obtained if we assume a magnetic dipole moment of the form $\mu = \mu_0 \sin(2\pi f_0 t)$ where μ_0 is equal to $|\mu_0| = \frac{e x_0 f_0 \alpha}{c}$. So the radiated field is:

$$|E| = |H| = \frac{-8\pi^3 e x_0 f_0^3 \alpha}{r c^3} \sin(\theta) \sin[2\pi f_0 (t - r/c)]. \tag{1.15}$$

1.1.2 Some aspects of the interaction of electromagnetic radiation and matter

During every spectroscopic measurement what really happens is a transition between two or more (not necessarily electronic) states. These transitions are induced by the interaction of the incident electromagnetic field with an atom or a molecule. In order for such an interaction to occur, there must be some charge distribution to interact with the electromagnetic field. Depending on the type of charge distribution (and consequently on the way it interacts with the field) we have dipole, quadrupole or magnetic dipole transitions with the latter being much weaker than the others. Let us assume that we have two states (with wavefunctions ψ_n, ψ_k and energies E_n and E_k), which participate in the transition and are occupied by N_n and N_k number of particles, respectively. There are three different processes that may occur during the interaction of our system with an electromagnetic wave. We can have spontaneous emission, induced absorption and induced emission. Some aspects of those processes are the following:

(i) Spontaneous emission During this process we have a transition of the type $n \to k$ where $E_n > E_k$. This process is characterized by the formula

$$-\frac{dN_n}{dt} = N_n A_{n\to k} \tag{1.16}$$

where $A_{n\to k}$ is the Einstein transition probability of the spontaneous emission and represents the probability of a system in n state to spontaneously pass to the lower k state by emitting radiation (or in general to lose energy in some way).

(ii) Induced absorption The formula representing this process is

$$-\frac{dN_k}{dt} = N_k B_{k\to n}\varrho(f_{nk}) \tag{1.17}$$

Where $B_{k\to n}$ is the Einstein transition probability of induced absorption. Here we see that the rate of transitions depends on the radiation density due to incident electromagnetic radiation of energy $h(f_n - f_k)$.

(iii) Induced emission If we have a radiation field of density $\varrho(f_{nk})$ it might also induce the transition of the system from the higher k state to the lower n accompanied by the emission of radiation of energy $h(f_k - f_n)$. The formula of this process is quiet similar to that of the previous one:

$$-\frac{dN_n}{dt} = N_n B_{n\to k}\varrho(f_{nk}) \tag{1.18}$$

1.2 Formulation of the scattering tensor

In order to obtain a clear picture of the problem of light scattering by matter we need to investigate the interaction of atoms (it is a good approximation to neglect the contribution of the nucleus and account only for electrons) with the incident photons. We are going to examine this in a semi-classical way meaning that we are treating the electrons quantum mechanically but we will stick to the classical description of the electromagnetic field [1]. Let us assume that the wavefunction of the electrons of our system has the form:

$$\psi^0(q,t) = \sum_n \alpha_n \psi_n(q) e^{-iE_n t/\hbar} \tag{1.19}$$

where q is the coordinates (x,y,z) and the superscript 0 denotes that this wavefunction refers to the unperturbed system when the interaction with the electromagnetic field is absent. The next step is to account for the presence of the electromagnetic field. The perturbation potential arising from the electromagnetic field can be written as :

$$H^1 = -ME, \overrightarrow{M} = \sum_j e_j \overrightarrow{r_j} \tag{1.20}$$

Where e_j is the charge of the jth electron and $\overrightarrow{r_j}$ is its position vector. The superscript 1 on the H denotes that this is a first order perturbation. The time dependent Schrödinger equation of the perturbed system is:

$$(H^0 - ME)\psi^0(q,t) = -\frac{\hbar}{i}\frac{\partial \psi^0}{\partial t}(q,t). \tag{1.21}$$

In 1^{st} order perturbation we obtain the wave function $\psi_k(q,t)$ of the k state which has the formula:

$$\psi_k(q,t) = \psi_k^0(q,t) + \psi_k^1(q,t) \tag{1.22}$$

if we substitute (1.22) to (1.21) we obtain:

$$(H^0 - \frac{\hbar}{i}\frac{\partial}{\partial})\psi_k^1(q,t) = (EM)\psi_k^0(q,t) \tag{1.23}$$

and the solution of the differential equation is:

$$\psi_k^1 = \psi_k^+(q)e^{-i/\hbar(E_n+hf_0)t} + \psi_k^-(q)e^{-i/\hbar(E_n-hf_0)t} \tag{1.24}$$

If we assume that the electromagnetic wave is unpolarized and has a form $E = Ae^{2\pi i f_0 t} + A^* e^{-2\pi i f_0 t}$, and combining this with (1.24), (1.23) we obtain a set of equations that depend only on the coefficients with the same time dependent part:

$$H^0\psi_k^+(q) - (E_k + hf_0)\psi_k^+(q) = (AM)\psi_k(q) = \sum_r (AM_{kr})\psi_r \tag{1.25}$$

$$H^0\psi_k^-(q) - (E_k - hf_0)\psi_k^-(q) = (A^*M)\psi_k(q) = \sum_r (A^*M_{kr})\psi_r \tag{1.26}$$

where $\psi_k(q,t) = \psi_k^0(q)e^{-i/E_k\hbar t}$ is the wavefunction of the state k and $M_{kr} = \int \psi_r^* M \psi_k$,with ψ_r being also a solution of the $H_0\psi_r = E_r\psi_r$

From (1.25), (1.26) we obtain:

$$\psi_k^+ = \sum_r \frac{(AM_{kr})}{E_r - E_k - hf_0}\psi_r \tag{1.27}$$

$$\psi_k^- = \sum_r \frac{(A^*M_{kr})}{E_r - E_k + hf_0}\psi_r \tag{1.28}$$

So the wavefunction ψ_k^1 is given by :

$$\psi_k^1 = \frac{1}{h}\sum_r \psi_r \left[\frac{(AM_{kr})}{f_{rk} - f_0}e^{-i/\hbar(E_k+hf_0)t} + \frac{(A^*M_{kr})}{f_{rk} + f_0}e^{-i/\hbar(E_k-hf_0)t}\right] \tag{1.29}$$

It is of paramount importance to calculate the moment M of the electrons when they are under the influence of the electric field. If during the interaction of the particle with the electric field, we had an elastic scattering

then the particle would return to its initial state after the interaction. The expectation value of the moment corresponding to this case is the following:

$$M_{kk} = \int (\psi_k^0 + \psi_k^1)^* M (\psi_k^0 + \psi_k^1) d\tau \tag{1.30}$$

and by substitution of ψ_k^1 and ψ_k^{1*}:

$$\begin{aligned} M_{kk} = M_{kk}^0 + \frac{1}{h} \sum_r \left[\frac{(AM_{kr})M_{kr}}{f_{kr} - f_0} + \frac{M_{kr}(AM_{rk})}{f_{rk} + f_0} \right] e^{-2\pi i f_0 t} \\ + \frac{1}{h} \sum_r \left[\frac{(A^* M_{kr})M_{kr}}{f_{kr} + f_0} + \frac{M_{kr}(A^* M_{rk})}{f_{rk} - f_0} \right] e^{2\pi i f_0 t} \end{aligned} \tag{1.31}$$

where $M_{kk}^0 = \int \psi_k^0 M_k^0 d\tau$ is the static term and has nothing to do with the radiation. It expresses the intrinsic moment that the system might have in state k.The other two terms of (1.31) can be simplified as,

$$M_{kk}^{(1)} = C_{kk} e^{-2\pi i f_0 t} + C_{kk}^* e^{2\pi i f_0 t} \tag{1.32}$$

where

$$C_{kk} = \frac{1}{h} \sum_r \left[\frac{(AM_{kr})M_{kr}}{f_{kr} - f_0} + \frac{M_{kr}(AM_{rk})}{f_{rk} + f_0} \right] e^{-2\pi i f_0 t} \tag{1.33}$$

It is important that equation (1.32) is real and the time dependent part is identical to that of the incident radiation. Also, if we assume a plane polarization of the incident light, meaning that $A = E_0 e^{i\phi}$ the scattered light will have the same polarization. This can be deduced by substitution of the expression of A and by the absence of phase difference between incident and scattered light. So, it is obvious that (1.32) represents a scattered radiation which is collinear, in phase, and has the same frequency as the incident one. This phenomenon is called Rayleigh scattering. Let us now formulate the type of the induced dipole moment for transitions, which do not end up at the initial state of the system. The derivation would be in the same manner as was done for Rayleigh scattering right above:

$$\begin{aligned} M_{kn} &= \int (\psi_n^0 + \psi_n^1)^* M (\psi_k^0 + \psi_k^1) d\tau \\ &= M_{kn}^{(0)} + M_{kn}^{(1)} + M_{kn}^{(2)} \end{aligned} \tag{1.34}$$

where

$$M_{kn}^{(0)} = M_{kn} e^{-2\pi i f_{kn} t} \tag{1.35}$$

$$M_{kn}^{(1)} = \frac{1}{h}\sum_r \left[\frac{(AM_{kr})M_{rn}}{f_{rk}-f_0} + \frac{M_{kr}(AM_{rn})}{f_{rn}+f_0}\right] e^{-2\pi i(f_{kn}+f_0)t} + \frac{1}{h}\sum_r \left[\frac{(A^*M_{kr})M_{rn}}{f_{rk}+f_0} + \frac{M_{kr}(A^*M_{rn})}{f_{rn}-f_0}\right] e^{2\pi i(f_{kn}-f_0)t} \tag{1.36}$$

$$M_{kn}^{(2)} = \frac{1}{h^2}\sum_{r,p} \left[\frac{(A^*M_{kp})M_{pr}(A^*M_{rn})}{(f_{pk}-f_0)(f_{rn}-f_0)} + \frac{(A^*M_{kp})M_{pr}(A^*M_{rn})}{(f_{pk}-f_0)(f_{rn}+f_0)}\right] e^{-2\pi i f_{kn} t} + \frac{1}{h^2}\sum_{r,p} \left[\frac{(A^*M_{kp})M_{pr}(A^*M_{rn})}{(f_{rn}+f_0)(f_{kp}-f_0)}\right] e^{-2\pi i(f_{kn}-2f_0)t} + \frac{1}{h^2}\sum_{r,p} \left[\frac{(AM_{kp})M_{pr}(AM_{rn})}{(f_{rn}-f_0)(f_{pk}+f_0)}\right] e^{-2\pi i(f_{kn}+2f_0)t} \tag{1.37}$$

where $(f_{kn})(etc.)$ $f_{kn} = f_k - f_n$. The first part of (1.34) represents scattered photons with energy equal to $h(f_k - f_n)$. This energy corresponds to transition $n \to k$, which is induced by the presence of the electromagnetic field. The second part ($M_{kn}^{(1)}$) represents radiation scattering of frequency $f_{kn} + f_0$ (which means that $E_n < E_k + hf_0$) and $f_{kn} - f_0$ (which means $E_k > E_n + hf_0$). These processes correspond to the Raman scattering. The first one is the Anti-Stokes and the second one is the Stokes part of the Raman spectrum.

It is important to point out that r, p are real states of the scattering particle, their eigenvectors span an orthonormal base, and the induced dipole moment depends on them. This dependence is not random, meaning that not any given state r or p can play this role.

1.2.1 The scattering tensor

As we know, the Rayleigh scattering is related to the following moment [1]

$$M_{kk}^1 = C_{kk} e^{-2\pi i f_0 t} + C_{kk} e^{2\pi i f_0 t} \tag{1.38}$$

where

$$C_{kk} = \frac{1}{h}\sum_r \left[\frac{(AM_{kr})M_{rk}}{f_{rk}-f_0} + \frac{M_{kr}(AM_{rk})}{f_{rk}-f_0}\right] \tag{1.39}$$

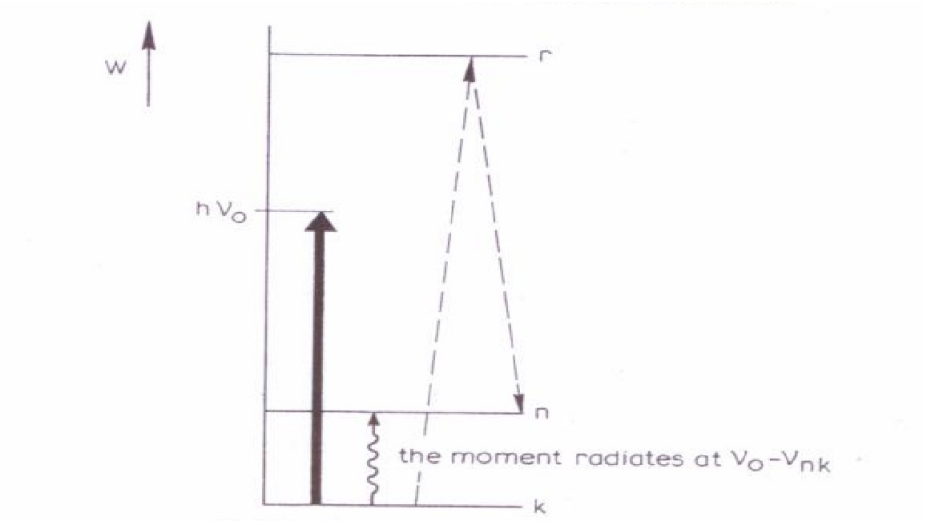

Figure 1.4: Stokes scattering

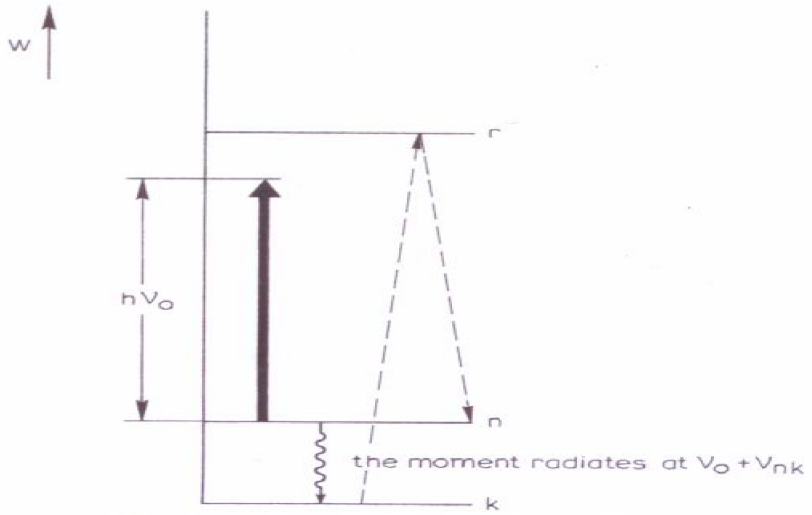

Figure 1.5: Anti-Stokes scattering

Following the same approach for the coefficients of the moment expression of the Raman effect we have:

$$C_{kn} = \frac{1}{h} \sum_r \left[\frac{(AM_{kr})M_{rn}}{f_{rk} - f_0} + \frac{M_{kr}(AM_{rn})}{f_{rk} - f_0} \right] \tag{1.40}$$

which is a 3^{rd} order tensor. Its coordinates in the Cartesian basis can be written in a more general form as:

$$(C_\varrho)_{kn} = \frac{1}{h} \sum_r \left[\frac{\sum_\sigma A_\sigma (M_\sigma)_{kr}(M_\varrho)_{rn}}{f_{rk} - f_0} + \frac{\sum_\sigma (M_\varrho)_{kr} A_\sigma (M_\sigma)_{rn}}{f_{rk} - f_0} \right] \tag{1.41}$$

so (1.41) can be expressed as:

$$(C_\varrho)_{kn} = \sum_\sigma (\alpha_{\varrho\sigma})_{kn} A_\sigma \tag{1.42}$$

where

$$(\alpha_{\varrho\sigma})_{kn} = \frac{1}{h} \sum_r \left[\frac{(M_\sigma)_{kr}(M_\varrho)_{rn}}{f_{rk} - f_0} + \frac{(M_\varrho)_{kr}(M_\sigma)_{rn}}{f_{rn} - f_0} \right] \tag{1.43}$$

From (1.42) we can formulate expressions associating the spatial orientation of the incident electromagnetic field and the spatial components of the $(C_\varrho)_{kn}$ coefficients, which in fact determine the induced dipole moments along three polarization axes, the Cartesian axes:

$$\begin{aligned} (C_x)_{kn} &= (\alpha_{xx})_{kn} A_x + (\alpha_{xy})_{kn} A_y + (\alpha_{xz})_{kn} A_z \\ (C_y)_{kn} &= (\alpha_{yx})_{kn} A_x + (\alpha_{yy})_{kn} A_y + (\alpha_{yz})_{kn} A_z \\ (C_z)_{kn} &= (\alpha_{zx})_{kn} A_x + (\alpha_{zy})_{kn} A_y + (\alpha_{zz})_{kn} A_z \end{aligned} \tag{1.44}$$

It is obvious that α is a rank two tensor, which determines the spatial orientation of the induced moments for a given incident electromagnetic field and it is called scattering tensor. Obviously as a rank two tensor it has the form:

$$\begin{pmatrix} \alpha_{xx} & \alpha_{xy} & \alpha_{xz} \\ \alpha_{yx} & \alpha_{yy} & \alpha_{yz} \\ \alpha_{zx} & \alpha_{zy} & \alpha_{zz} \end{pmatrix} \tag{1.45}$$

The intensity of the emitted radiation associated with Raman scattering is:

$$I = \frac{64\pi^4 (f_0 + f_{kn})^4}{3C^3} |C_{kn}|^2 \tag{1.46}$$

combining (1.46),(1.43),(1.42) and a plain polarized incident light we obtain:

$$I_{kn} = \frac{128\pi^5(f_0 + f_{kn})^4}{3c^4}\left(\sum_{\sigma}(\alpha_{\varrho\sigma})_{kn}\right)^2 I_0, \qquad I_0 = \frac{c}{8\pi}E_0^2 \tag{1.47}$$

or in a more simplified manner

$$I_{kn} = Q_{kn}I_0 \tag{1.48}$$

where

$$Q_{kn} = \frac{128\pi^5(f_0 + f_{kn})^4}{3c^4}\left|\sum_{\sigma}(\alpha_{\varrho\sigma)_{kn}}\right|^2 \tag{1.49}$$

The quantity Q_{kn} is called cross section of the scattered radiation and depends on the polarizability tensor elements and consequently on the polarization of the incident light. We can follow the same procedure for the Raman component of the expansion of the induced moment. The tensor for the hyper Raman effect is more complicated, though it can be formulated with the same technique used above. So, the corresponding moments are:

$$D_{kn} = \frac{1}{h^2}\sum_{r,p}\left[\frac{(AM_{kp})M_{pr}(AM_{rn})}{(f_{rn} - f_0)(f_{pk} + f_0)}\right] \tag{1.50}$$

The expression for the three components of the moment is

$$(D_\sigma)_{kn} = \frac{1}{h^2}\sum_{r,p}(M_\sigma)_{pr}[\sum_{\sigma}(A_\sigma A_\sigma(M_\sigma)_{pr}(M_\sigma)_{rn}) + \sum_{\sigma\neq\varrho}A_\sigma A_\varrho(M_\sigma)_{rn}(M_\varrho)_{pr}] \tag{1.51}$$

so

$$(D_\varrho)_{kn} = \beta_{\varrho\sigma\sigma'}A_{\sigma'}A_\sigma \tag{1.52}$$

and $\beta_{\varrho\sigma\sigma'}$:

$$\beta_{\varrho\sigma\sigma'} = \frac{1}{h^2}\sum_{r,p}\frac{(M_{\sigma'})_{rk}(M_\sigma)_{pr}(M_\varrho)_{kp}}{(f_{rk} + f_0)(f_{pn}) - f_0} \tag{1.53}$$

1.2.2 Symmetry of the scattering tensor

The operator M of the induced dipole moment is Hermitian as proved from (1.54) and as an observable of a quantum system :

$$\left[\int \psi_k^* M\psi_r d\tau\right]^* = \int \psi_r^* M\psi_k d\tau$$

which is equal to:

$$[M_{rk}]^* = M_{kr} \tag{1.54}$$

if we substitute (1.54) in the expression of $\alpha_{(\varrho\sigma)_{kr]}}$ (1.43) (with $k = n$) we obtain:

$$(\alpha_{\varrho\sigma})_{kk} = (\alpha_{\sigma\varrho})^*_{kk} \tag{1.55}$$

if the wavefunction of the states r, p are real then from (1.55) $(\alpha_{\varrho\sigma})_{kk} = (\alpha_{\sigma\varrho})_{kk}$, which means that the scattering tensor is symmetric and the nine independent elements of the asymmetric case are reduced to six. For real elements of the scattering tensor and by modifying (1.32) we obtain:

$$M^{(1)}_{kk} = \sum_{\sigma} (\alpha_{\varrho\sigma})_{kk} (A_\sigma e^{-2\pi i f_0} + A^*_\sigma e^{2\pi i f_0})$$

$$M^{(1)}_{kk} = \sum_{\sigma} (\alpha_{\varrho\sigma})_{kk} E_\sigma \tag{1.56}$$

The real elements $(\alpha_{\varrho\sigma})_{kk}$ form the so called polarizability tensor, which is a special case of the more general scattering tensor that might be asymmetric even for real wavefunctions [1], [4].

1.3 The scattering operator

As we know from quantum mechanics if we want to calculate the average value of a physical quantity we must take the inner product of the corresponding operator with the wavefunction that describes the system $P = \int \psi^*_n \hat{P} \psi_k$ or in Dirac formalism $P =< \psi_n | \hat{P} | \psi_k >$. Thus for the average value of the electric dipole operator we have $< \psi_n | \sum_i e_i r_i | \psi_k >$. If this inner product is different from zero we know that an electric dipole transition between k, n states is allowed. Based on the expression for the scattering tensor elements and substitute the dipole moments with the average value of the dipole operator of the corresponding states, we obtain:

$$(\alpha_{\varrho\sigma})_{kn} = \frac{1}{h} \sum \left[\frac{< \psi_k | \sum_i e_i \sigma | \psi_r >< \psi_r | \sum_i e_i \varrho | \psi_n >}{f_{rk} - f_0} + \frac{[\varrho \leftrightarrow \sigma]}{f_{rn} + f_0} \right] \tag{1.57}$$

we can rewrite this equation as an inner product :

$$(\alpha_{\varrho\sigma})_{kn} =< \psi_n | \hat{\alpha}_{\varrho\sigma} | \psi_k > \tag{1.58}$$

where the quantity $\hat{\alpha}_{\varrho\sigma}$ is the scattering operator

$$(\hat{\alpha}_{\varrho\sigma})_{kn} = \frac{1}{h} \sum \left[\frac{| \sum_i e_i \varrho | \psi_r >< \psi_r | \sum_i e_i \sigma |}{f_{rk} - f_0} + \frac{[\varrho \leftrightarrow \sigma]}{f_{rn} + f_0} \right] \tag{1.59}$$

Obviously if we know the behavior of the wavefunctions of the states participating in the scattering process we can write down the scattering tensor and subsequently we can deduce the properties of the scattered light.

1.3.1 Symmetry considerations

It is evident that for a Raman (or Rayleigh) transition to take place two conditions must be satisfied: first $(\alpha_{\varrho\sigma})_{kn} \neq 0$ which simply states that the corresponding elements of the scattering tensor must be nonzero and second $< \psi_n|\hat{\alpha}_{\varrho\sigma|\psi_k} > \neq 0$. In order to examine those two conditions we would benefit a lot if we consider the symmetry of the system and use some results from group theory. Let us assume that we know the irreducible representations of the initial and final states Γ_{ψ_k} and Γ_n respectively and the irreducible representation, which describes the scattering operator. We can check whether a scattering element is nonzero if the triple product below belongs to the fully symmetric representation of a point group:

$$\Gamma_{\psi_n^*} \times \Gamma_{\alpha_{\varrho\sigma}} \times \Gamma_{\psi_k} \tag{1.60}$$

If we want (1.57) to have nonzero elements the inner products inside the summation must not vanish, so:

$$< \psi_n|e\varrho|\psi_k > \neq 0 \quad if \qquad \Gamma_{\psi_n^*} \times \Gamma_{\varrho} \times \Gamma_{\psi_r} \equiv A \tag{1.61}$$

$$< \psi_k|e\sigma|\psi_r > \neq 0 \quad if \qquad \Gamma_{\psi_k^*} \times \Gamma_{\sigma} \times \Gamma_{\psi_r} \equiv A \tag{1.62}$$

where A is the total symmetric representation. By combining (1.61) and (1.62) and doing some elementary calculations we obtain:

$$\Gamma_{\alpha_{\hat{\varrho\sigma}}} \times \Gamma_{\varrho\sigma} \equiv A \tag{1.63}$$

which means that

$$\Gamma_{\hat{\alpha}_{\varrho\sigma}} \equiv \Gamma_{\varrho\sigma} \tag{1.64}$$

The selection rule for Raman scattering becomes rather simple if the initial state of the system transforms as the total symmetric representation. Then the only condition for a transition to be allowed is:

$$\Gamma_{\psi_n} = \Gamma_{\hat{\alpha}} \tag{1.65}$$

which means that the final state and the scattering operator must transform with the same irreducible representation [4].

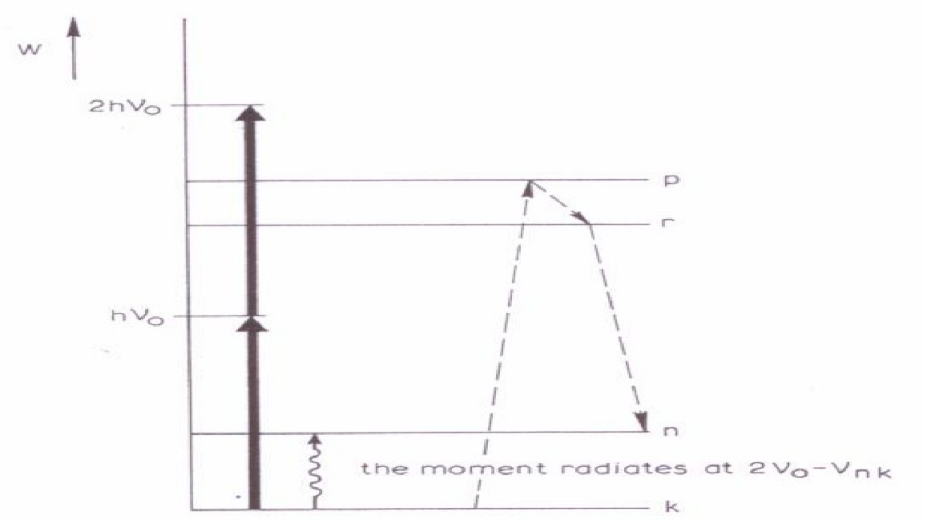

Figure 1.6: hyper Raman Stokes scattering

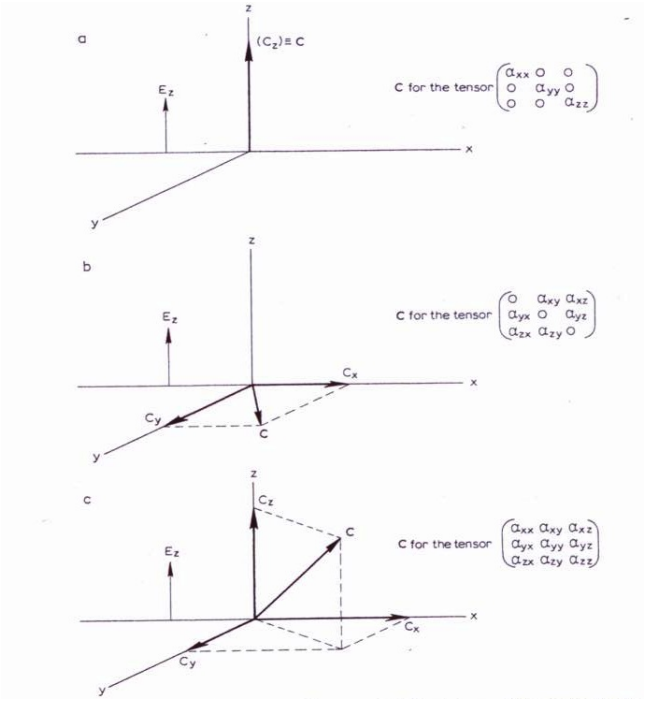

Figure 1.7: The direction of the induced dipole moment for different cases of scattering tensors and for incident light polarized along the z-axis

Chapter 2

Ferroelectricity

2.1 Introduction

Ferroelectricity is the physical property of some materials to exhibit a spontaneous electric polarization without the application of an external field. Furthermore, these materials exhibit a characteristic hysteresis mechanism, meaning that in order to eliminate this polarization an external opposite field must be applied. Ferroelectricity can be considered as the electric analogue to ferromagnetism. Despite the fact that both phenomena describe a spontaneous polarization or magnetization of matter there are three major differences between them. First of all the coupling in a ferromagnetic material is rather weak and the interaction between two magnetic dipoles is short range in comparison with electric dipole interaction which is much stronger. The second difference is the appearance of screening in a ferroelectric material which means that, when such materials are polarized, charges tend to accumulate on their surface in order to cancel the electric field associated with the spontaneous polarization. This is not present in ferromagnetic materials due to the absence (as far as we know) of magnetic monopoles. This is the reason why ferromagnetism was known from ancient times in contrast to ferroelectricity which was observed much later. The third difference is the fact that the polarization is strongly associated with the lattice (its origin is sometimes attributed to lattice instabilities) whereas ferromagnetism has a weaker correlation to lattice phenomena. In the following section we are going to present a phenomenological approach to ferroelectricity using Landau's theory of phase transitions.

2.2 Phenomenological approach to ferroelectricity

Before we proceed it is essential to stress out the limitations of such approach. Fist of all Landau's theory is a phenomenological theory based on symmetry arguments meaning that it does not describe the underlying microscopic mechanism. In general, phenomenological theories link together microscopic models and macroscopic observations. Landau parametrized the symmetry change of systems in equilibrium near the transition point with an order parameter. The free energy of the system is expanded in terms of this order parameter and the properties of the system in the vicinity of the transition are calculated by minimization of the free energy with respect to this order parameter. Landau's theory stands, if the order parameter fluctuations are small compared to the order parameter itself over a volume determined by the correlation length. This implies that it is safe to use this theory in systems with high dimensionality or long range interactions. In the case of ferroelectricity (where long range interactions take place) the Landau theory is applicable under some conditions.

We will start with the simplest case and go on with a more realistic one. Let us assume that we have a bulk ferroelectric crystal which has no impurities and all its dipole moments can be polarized in one direction. We can write the following expression for the free energy density [17]

$$F_P = \frac{1}{2}\alpha P^2 + \frac{1}{4}bP^4 + \frac{1}{6}cP^6 - EP \tag{2.1}$$

The equilibrium demands:

$$\frac{\vartheta F_P}{\vartheta P} = 0 \tag{2.2}$$

so

$$E = \alpha P + bP^3 + cP^4 \tag{2.3}$$

and if we differentiate the equation above and set $P = 0$ we obtain:

$$\frac{1}{\alpha} = \frac{P}{E} = \chi \tag{2.4}$$

it is assumed that α has the following dependence on temperature around the Curie point where $T \sim T_0$

$$\alpha = \alpha_0(T - T_0) \tag{2.5}$$

from (2.4)

$$\kappa = \frac{1}{\chi} = \alpha_0(T - T_0) \tag{2.6}$$

which is the expected Curie-Weiss behavior of dielectric stiffness for $T > T_0$. Going back to (2.1)

$$F_P = \frac{1}{2}\alpha_0(T - T_0)P^2 + \frac{1}{4}bP^4 + \frac{1}{6}cP^6 - EP \tag{2.7}$$

where α_0, c are considered positive. So, the way the free energy transforms across the phase transition is determined by the sign of b.

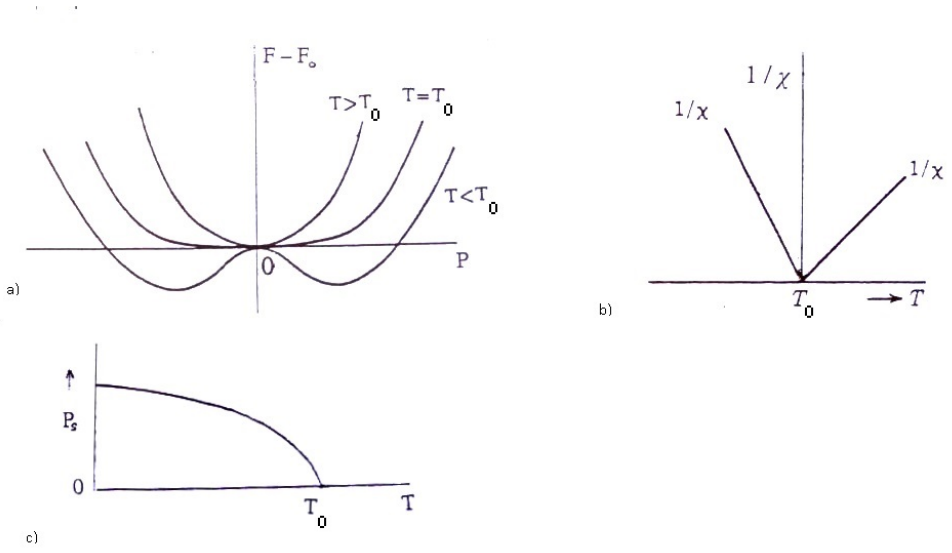

Figure 2.1: Second order phase transition a) The free energy as a function of temperature. We can clearly see that above T_0 the energy favorable state is that with zero polarization, while below the transition temperature two degenerate states with spontaneous polarization exist. b) The dielectric stiffness vanishes at the transition temperature which implies a discontinuous behavior of the susceptibility. c) The spontaneous polarization decreases continuously to zero as we approach the transition temperature from below.[16]

The first option is when $b > 0$; in that case the free energy evolves as a decreasing function of temperature from the case where the minimum is at $P = 0$ for $T > T_0$ to $P = \pm P_s$ as shown in figure (2.1). From (2.3) by setting $E = 0$ and keeping only the first two terms (because all coefficients are positive) the spontaneous polarization will be:

$$P_s = \left[\frac{\alpha_0}{b}(T_0 - T)\right]^{1/2} \tag{2.8}$$

As we see, the spontaneous polarization will increase with decreasing tem-

perature. The dielectric stiffness for $T < T_0$ is

$$\kappa = 2\alpha_0(T_0 - T) \tag{2.9}$$

which means that κ vanishes for $T = T_0$ and the temperature dependence is different above and below T_0. It is obvious that at the vicinity of the transition there will be a divergence of the susceptibility.

As we know, the specific heat is given by $C_\nu = -T\frac{\vartheta^2 F_P}{\vartheta T^2}$ so, if we want to determine how the specific heat changes due to the transition we can write:

$$\Delta C_\nu = C_\nu(T = T_0^+) - C_\nu(T = T_0^-)$$
$$\Delta C_\nu = \frac{\alpha_0^2 T_0}{2b} \tag{2.10}$$

As we see ΔC_ν is a positive quantity which means that there is an increase in the specific heat across the transition. In general, those types of transitions as the one described above are called second order phase transitions and they are associated with a continuous evolution of the order parameter. Also the transition is characterized by a lowering of symmetry from a more symmetric state of the system (for $T > T_0$) to a less symmetric one below the transition temperature.

The other case is when $b < 0$. The fact that the quadratic coefficient is negative implies that the free energy might have a local minimum above T_0 apart from the trivial $P = 0$. As we reduce the temperature (and consequently the α coefficient) the polarized states would become more and more energetically favorable and at the Curie temperature T_c the polarized and unpolarized states are energetically equivalent. The two phases coexist until T_0 is reached. The most important feature of those transitions (which are called first order) is that the order parameter jumps discontinuously to zero when the Curie temperature is approached. We can use the same arguments as for the second order phase transition with the difference that, when we use (2.3) for $E = 0$, we can not neglect the third term because b is now negative. By doing some calculations we can get the value for the spontaneous polarization and the Curie temperature:

$$P_s^2 = -\frac{b}{2c}\left[1 + (1 - \frac{4\alpha c}{b^2}(T - T_0))^{1/2}\right] \tag{2.11}$$

$$T_c = T_0 + \frac{3}{16}\frac{b^2}{ac} \tag{2.12}$$

In the same manner as for the second order transitions the susceptibility above T_c is

$$\frac{1}{\chi} = \alpha_0(T - T_0) \tag{2.13}$$

For $T < T_c$ by differentiation with respect to the polarization of (2.3) and by substitution of (2.11) we obtain:

$$\frac{1}{\chi} = 4\alpha_0(T_c - T_0) \tag{2.14}$$

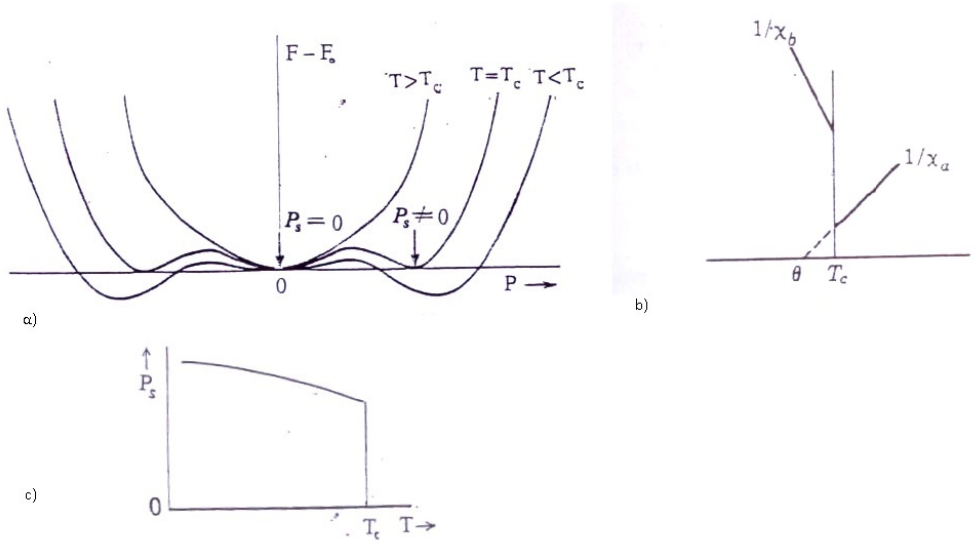

Figure 2.2: First order phase transition a) Free energy as a function of temperature: we clearly see the coexistence of the polarized and unpolarized states above T_0. b) The inverse susceptibility presents a discontinuity at T_c. c) The spontaneous polarization drops to zero with a jump at T_c. [16]

Another interesting feature about first order ferroelectric transitions is that the state that our system would have across the transition is determined by whether the transition point is being approached from below or above. So in the case that we heat the material to reach the Curie temperature from below it would be in the polarized state but if we cool the system from a temperature higher than T_c the favorable state is the unpolarized. This happens despite the fact that at T_c the polarized and unpolarized state are both a minimum of free energy.

2.2.1 Coupling of stress and spontaneous polarization

Generally ferroelectrics are very sensitive to the application of an elastic stress (all ferroelectrics exhibit piezoelectricity also) with respect to their

ferroelectric transition. If we imagine the microscopic mechanism of ferroelectricity we can see more clearly why this coupling takes place. Let us imagine a cubic crystal at its paraelectric phase. If our material undergoes a ferroelectric transition the spontaneous polarization points in one of the high symmetry axis which is no longer equivalent to the other as if the material's symmetry has been lowered to tetragonal. Such distortion can be easily described as a strain ϵ along this axis. The next step is to formulate the free energy with the strain as order parameter and by allowing terms which are coupled to the polarization. These coupled terms must be chosen wisely because they must reflect the symmetry of the problem. For example in our case the lowest order allowed term must be linear to the strain and tetragonal to the polarization. So the free energy should have the form [17]

$$F_\epsilon = \frac{1}{2}K\epsilon^2 + Q\epsilon P^2 - \epsilon\sigma \tag{2.15}$$

The first term is the elastic energy stored to the system due to its deformation, so K is one of the elastic constants. The second term is the coupling between the strain and the polarization. Now we can determine the properties of the equilibrium by minimizing the total free energy $F = F_P + F_\epsilon$,

$$\frac{\vartheta F(P,\epsilon)}{\vartheta P} = \frac{\vartheta F(P,\epsilon)}{\vartheta \epsilon} = 0 \tag{2.16}$$

The second part of the equality gives

$$\frac{\vartheta F(P,\epsilon)}{\vartheta \epsilon} = K\epsilon + QP^2 - \sigma \tag{2.17}$$

For $P = 0$ we get the Hooke's law, but lets assume a more interesting example. Let us say that the applied stress cancels out the strain produced by the ferroelectric transition. It that case we have perfect clamping, as it is said, so $\epsilon = 0$ and the free energy remains unchanged. Another case is when the applied stress is zero so the strain from the transition is:

$$\epsilon = -\frac{QP^2}{K} \tag{2.18}$$

so the free energy can be rewritten as:

$$F(P,\epsilon(P)) = \frac{1}{2}\alpha P^2 + \frac{1}{4}(b - 2Q^2/k)P^4 + \frac{1}{6}cP^6 + ... - EP \tag{2.19}$$

As we can see, a strain affects the quadratic term of the expansion and if we are studying a first order transition (where b is negative) the appearance of strain just enhances the discontinuous nature of the phase transition

(simply "makes" the quadratic term more negative). However if we have a positive b and we decide to "clamp" our system it is obvious that the nature of the transition itself can be altered. In general hydrostatic pressure and biaxial stress from chemical substitution is used widely in material science in order to change the features of the transition and especially the transition temperature.

2.2.2 Deviation from perfect polarization

Domain structures

The case that a bulk ferroelectic becomes fully polarized towards one direction is far from a realistic one. The reason for that are microscopic defects, non-uniform stresses, and the thermal/electrical history of the sample, which contribute to the formation of domains. Moreover, as we would see, even in a perfect crystal the appearance of some sort of domains will be energetically preferable. On the surface of a perfect polarized material we expect free charges to accumulate. It is obvious that if we have domain structure inside a material (assuming that within a domain the polarization is uniform) there would be an accumulation of surface charges on the interfaces between different domains. Those charges would store energy (just like a capacitor) so our system would prefer to adopt a domain structure which minimizes this energy. The interface charge density between two domains is:

$$\sigma = (P_1 - P_2) \cdot \hat{n} \tag{2.20}$$

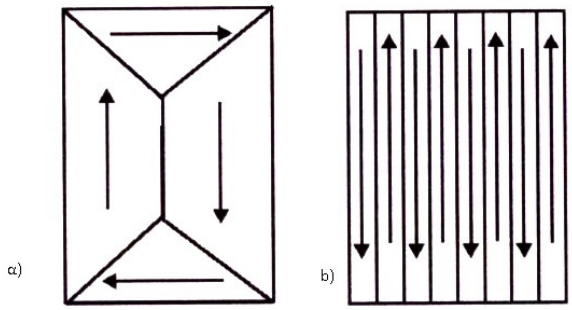

Figure 2.3: a) example of 90^0 domain wall b) 180^0 domain wall [17]

where P_1, P_2 are the polarizations in two neighbor domains and n is the unit vector normal to the domain interface. We can understand that there are two configurations, which lead to the vanishing of the interface charges. The

first is that neighboring domains have antiparallel polarization (namely the 180^0 domain wall) and the second is when the domain wall bisects the angle between two domains that are head-to-tail. The last case is called 90^0 domain wall because in cubic materials two neighboring vectors of polarization are perpendicular. The formation of domains introduces stress inhomogeneities which counteract the energy lowering introduced by forming polarized states. Especially for 90^0 domain wall, inhomogeneities are introduced which behave in complex ways. The form of the domain might deviate significantly from the perfect one in order to relax those stresses. Furthermore dislocations and cracks introduce even more complexity to the real form of the domains.

Non uniform polarization

As stated above the case where we have a perfect polarization is far from realistic so it is essential to have a short discussion on how we treat the case of a spatially nonuniform order parameter (here the polarization) again in a phenomenological framework, which of course would imply some limitations. The first limitation to accept in order to proceed is that the fluctuations of the order parameter along different wavevectors in our material must be uncorrelated. With that in mind we would write the expansion of the free energy (which is the key point of the Landau analysis) in terms of the gradient of polarization. This analysis is generally called Ginzburg-Landau theory. The first orders of the free energy density expansion will be:

$$F = \alpha_0(T - T_0) \int d^3\vec{r}[P(\vec{r})]^2 + \gamma \int d^3\vec{r}[\nabla P(\vec{r})]^2 \tag{2.21}$$

By doing the Fourier transform of the free energy we get:

$$F = \int \frac{d^3\vec{k}}{(2\pi)^3}(\alpha_0(T - T_0) + \gamma k^2)|P(\vec{k})|^2 \tag{2.22}$$

Using the equipartition theorem (and the fact that in our expansion we have two quadratic degrees of freedom) we obtain:

$$(\alpha_0(T - T_0) + \gamma k^2)|P(\vec{k})|^2 = \kappa_B T \tag{2.23}$$

From here we can introduce the correlation function for the polarization which would give us a measure of the spatial fluctuation of the polarization:

$$g(\vec{r}) =< P(\vec{r})P(\vec{0}) > - < P(\vec{0}) >^2 \tag{2.24}$$

Taking the Fourier transform of the equation above (in the parelectric phase where $< P_{\vec{0}} >= 0$ and with no correlation between the modes with different wavevectors) we obtain:

$$g(\vec{q}) =< |P(\vec{q})|^2 > \tag{2.25}$$

Combining (2.25) with (2.23) we obtain the Fourier transform of the correlation function:

$$g(\vec{q}) = \frac{\kappa_B T}{\alpha_0(T - T_0) + \gamma k^2} \tag{2.26}$$

Now we simply take the inverse Fourier transformation

$$g(\vec{r}) \sim \frac{\kappa_B T}{\gamma} \frac{e^{-r/\xi}}{r} \qquad T \neq 0 \tag{2.27}$$

$$g(\vec{r}) \sim \frac{\kappa_B T}{\gamma} \frac{1}{r} \qquad T = 0 \tag{2.28}$$

We see that for $T > T_0$ the correlation function decreases exponentially, at $T = T_0$ it follows a power law and the correlation length is

$$\xi = \sqrt{\frac{\gamma}{\alpha_0 |T - T_0|}} = \sqrt{\frac{\gamma}{\alpha_0 T_0}} \sqrt{\frac{T_0}{|T - T_0|}} \equiv \xi_0 |t|^{-1/2} \tag{2.29}$$

where $t = \frac{T - T_0}{T_0}$ is the reduced temperature. The physical meaning of the correlation length: for $T > T_0$ is the length scale where polarization exist and for $T < T_0$ is the length scale in which the polarization fluctuates from its equilibrium value. The correlation length can help us identify the boundaries where Ginzburg-Landau theory ceases to be valid. The essence of this criterion is that all 'modes' must be "coarse-grained" on a scale of the correlation length.

2.2.3 Lattice instabilities and ferroelectricity

General aspects

Keeping in mind the analysis done in the previous sections one can think that if we take Landau's analysis literately we would form a picture of the problem where the lattice displacements associated with the polarization are equal to zero above T_c and take finite values below it; such a transition can be characterized as a displacive one. Another possibility is that locally there is a symmetry breaking, which induce dipole moments even above T_c but those moments are randomly oriented as long as the transition temperature has not been reached. One question that needs to be answered in the case of displacive ferroelectricity is how much charge redistribution is produced by a displacement of an ion. One way to measure the impact of a transverse optic phonon is a quantity called transverse electric charge Z_T^* and it measures the average dipole moment per unit cell p generated by an ionic displacement u

$$p = Z_T^* e u \tag{2.30}$$

Obviously different optical modes have different Z_T^* or even zero transverse charge if the displacement preserves inversion symmetry. If we assume that for some reason a transverse optic mode "softens" (decreases in frequency until the vibration practically stops) and acquires an amplitude u_0 then a ferroelectric moment would appear with amplitude $Z_T^* e u_0$. This example gives us an idea of the correlation of an instability in the lattice with the appearance of polarization [18].

2.2.4 More about soft modes

Here we are not going to present in full extend the analysis of lattice dynamics and instabilities but we are going to jump to some very interesting results, which support the hypothesis of the correlation of ferroelectric transitions with lattice instabilities. Let us assume a simple ionic crystal (more complicated structures would lead to more complicated equations) so that this simple example would give us the essential information about the physics of the problem. Using the shell model (and in the frame of harmonic approximation) one can write the equation of motion for the positive ion, the core, and the negative shell of the negative. After the system of equations is solved we obtain the following equations for the frequencies of longitudinal and transverse optical modes [2], [18]

$$\mu\omega_T^2 = R_0^{'} - \frac{4\pi(\epsilon_e + 2)(Z^{'}e)^2}{9\upsilon} \tag{2.31}$$

$$\mu\omega_L^2 = R_0^{'} + \frac{8\pi(\epsilon_e + 2)(Z^{'}e)^2}{9\upsilon\epsilon_e} \tag{2.32}$$

where ω_L, ω_T are the frequencies of longitudinal and transverse optic modes, $R_0^{'}$ is the effective force constant between the shells of the negative and the positive ions and $Z^{'}e$ the effective charge of the positive ion. The reason for taking effective values lies on the short range interactions of the lattice vibrations that generate the dipoles. Finally ϵ_e is the high frequency dielectric constant and υ is the volume of the unit cell. From the Lyddane-Sachs-Teller equation :

$$\frac{\omega_L^2}{\omega_T^2} = \frac{\epsilon_s}{\epsilon_e} \tag{2.33}$$

we can see that the static dielectric constant goes to infinity if :

$$R_0^{'} = \frac{4\pi(\epsilon_e + 2)(Z^{'}e)^2}{9\upsilon} \tag{2.34}$$

When this equality holds, the crystal becomes unstable for a zone center ($q = 0$) optic transverse mode (with no need to be unstable for any other normal mode).

In order to deduce the lattice instabilities we must go well beyond the harmonic approximation. Anharmonic effects tend to make parameters as R_0 to depend linearly on temperature. Having this in mind along with (2.31) we get:

$$1 - \frac{4\pi(\epsilon_e + 2)(Z^{'}e)^2}{9\upsilon R_0^{'}} = \frac{\mu\omega_T^2}{R_0^{'}} = \gamma(T - T_c) \tag{2.35}$$

where T_c is the temperature at which the instability just begin to take place.

Combining (2.31) (2.32) (2.33) we obtain:

$$\epsilon_s - \epsilon_e = \frac{4\pi(\epsilon_e + 2)^2(Z^{'}e)^2}{9\upsilon\mu\omega_T^2} \tag{2.36}$$

from (2.35):

$$\epsilon_s = \epsilon_e + \frac{4\pi(\epsilon_e + 2)^2(Z^{'}e)^2}{9\upsilon R_0^{'}\gamma(T - T_c)} \tag{2.37}$$

this remind us of the classic Curie-Weiss law:

$$\epsilon_s = \epsilon^{'} + \frac{4\pi\mathscr{C}}{T - T_c} \tag{2.38}$$

with Curie constant:

$$\mathscr{C} = \frac{4\pi(\epsilon_e + 2)^2(Z^{'}e)^2}{9\upsilon R_0^{'}\gamma} \simeq \frac{(\epsilon_e + 2)}{4\pi\gamma}$$

This is the behavior of our material in the paraelectric phase with the transition temperature being a singular (the physical meaning of this is the instability of the lattice) point of the static dielectric constant as expected.

Continuing our analysis in the anharmonic regime we can stress out an interesting result, which gives us a clear point of view what happens in the crystal in the vicinity of a lattice instability. Lets imagine a restoring force which acts upon the ions due to lattice vibrations of the form:

$$\mathscr{F}_{res} = R_0^{'}u + Bu^2 + B^{'}u^5 \tag{2.39}$$

The anharmonic nature of this force is obvious and for simplicity we can assume that the displacement u is along [001]. The presence of dipole moments would result in long range Coulomb interactions which would be displacive in nature and of the form:

$$\mathscr{F}_{coul} = \frac{4\pi(\epsilon_e + 2)(Z^{'}e)^2u}{9\upsilon} \tag{2.40}$$

So there is an antagonism between the long range coulomb force that drives the system away from stability and the short range restoring forces. This antagonism is depicted in Figure 2.4.

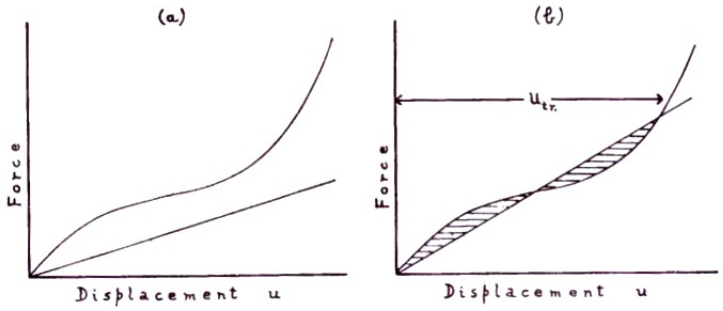

Figure 2.4: Restoring and displacing force as a function of displacement a) before transition temperature b) at the transition temperature [10]

The value of ω_T^2 is proportional to the difference in slope of the two figures at the origin. As the temperature is lowered, the slope of the lower graph (Coulomb force) increases until it intercepts the other at a finite displacement u. At this temperature the instability begins to take place but a full phase transition would not occur until the free energy is minimized. So we can state that a ferroelectric transition (at least the displacive ones which are of our interest) is associated with a low frequency $q = 0$ transverse optic mode resulting from a cancellation of short range and Coulomb interactions.

2.2.5 Some aspects of quantum criticallity in ferroelectrics

In general, a quantum critical point is a special case of a continuous transition which takes place at absolute zero temperature meaning that the quantum fluctuations, which dominate this range of temperatures, play the most important role in those transitions. Ferroelectics are excellent examples for studying quantum critical points because one can force (by pressure, chemical substitution etc) the transition temperature to drop down to zero and hence give us the opportunity to study novel states of matter. This ability of ferroelectrics comes from the fact that their criticallity (in contrast with ferromagents) is a lattice effect. When a quantum critical point is being approached physical quantities take new and unexpected forms. For example the electric susceptibility diverges from the familiar Curie-Weiss form $\chi^{-1} \sim T$ and takes a very different $\chi^{-1} \sim T^{-1}$ in the quantum critical point region.

There is a class of ferroelectrics that exhibit a much more interesting behavior. They are called quantum paraelectrics and the key feature is that their lattice instability is being counteracted by quantum fluctuation, so the soft mode does not really reach zero frequency even at zero temperature. It is profound that quantum paraelectricity is an area for fruitful investigation because we are dealing with systems that quantum fluctuations determine their macroscopic behavior.

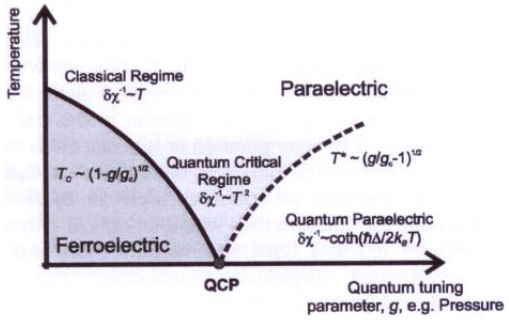

Figure 2.5: Phase diagram with quantum critical region. It is clear how the behavior of the system (for example the susceptibility) changes rapidly in the vicinity of a quantum critical point [10].

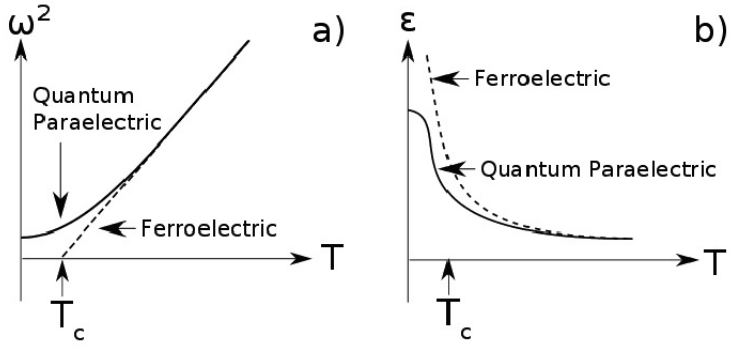

Figure 2.6: Typical behavior of a quantum paraelectric. The behaviour of the a) soft mode frequency and b) dielectric susceptibility deviates from the classic ferroelectric in a profound way.

Chapter 3

What is a Multiferroic material?

3.1 Introduction

Ever since Maxwell's equations electricity and magnetism are being considered as two sides of the same coin. Despite that for many years electric and magnetic ordering in materials had been most often examined separately. One profound reason for that is the fact that electric charges of electrons and ions are responsible for the electric effects whereas electronic spins and their interactions govern most of the magnetic phenomena. Through the ages some cross-links had been found between those two degrees of freedom, especially magnetic and electric coupling in insulators. If we had to trace the origin of this idea of new classes of materials where magnetic and electric phenomena are in strong correlation, we would present a short remark made at 1959 by Landau and Lifshitz at their classic textbook *Course of Theoretical Physics* :

> *Let us point out two more phenomena, which, in principle, could exist. One is piezomagnetism, which consist in linear coupling between a magnetic field in a solid and a deformation (analogous to piezoelectricity). The other is a linear coupling between magnetic and electric fields in a media, which would cause, for example a magnetization proportional to an electric field. Both these phenomena could exist for certain classes of magnetocrystalline symmetry. We will not discuss these phenomena in more detail because it seems that till present, presumably, they have not been observed in any substance [16]*

Soon after this assumption Dzyaloshinskii predicted and Astrov observed this type of coupling, which is nowadays called the magnetoelectric effect.

A new aspect of this problem is the possibility that not only cross-coupling of the responses of a material exist but also two types of ordering, ferroelectricity (spontaneous ordering of electric dipole moments) and ferromagnetism (spontaneous ordering of spin magnetic moments), may coexist in the same system and in fact they might appear spontaneously, without the application of any external filed. Multiferroics represent this new class of materials which bear those elusive properties (in fact there is another possibility of spontaneous deformation, ferroelasticity as it is called, but we will stay to the ferroelectric/ferromagnetic aspects of multiferroics). Ferromagnetism and ferroelectricity have quite different mechanisms. Localized electrons, mostly in partially filled d and f orbitals, give rise to localized magnetic moments, which align under some specific conditions (usually below some critical temperature). The magnetic ordering is due to the exchange interaction between the magnetic moments. On the other hand ferroelectricity originates from many different mechanisms and this gives us different types of multiferroics, which can be organized into two large groups namely type I and type II multiferroics. In type I multiferroics ferroelectricity presents itself largely independent of the ferromagnetism and the two have quite different origins. Particularly those materials exhibit ferroelectricity at higher temperatures than those at which magnetic ordering takes place, and the spontaneous polarization is quite large. The only thing that jeopardize the 'good' properties of those materials is the rather weak coupling between magnetic and electric ordering. On the other hand type II multiferroics have very strongly coupled magnetic and electric ordering and as a matter of fact ferroelectric ordering is driven by ferromagnetism. However the spontaneous polarization is rather weak. It is obvious that a combination of the two types would give an impressive material with strong coupling between the order parameters as well as a large spontaneous polarization.

3.1.1 Type I multiferroics

As stated above multiferroics of this class have 'good' ferroelectric and ferromagnetic properties, with critical temperatures (especially for the ferroelectricity) being in many cases at room temperature or above. Their only weak spot is the small coupling between their order parameters, which reduces the technological applications as well as the scientific appeal of this physical system.

By considering the different mechanisms by which ferroelectricity manifest itself we can subdivide the first class of multiferroics into four subcate-

gories [5]

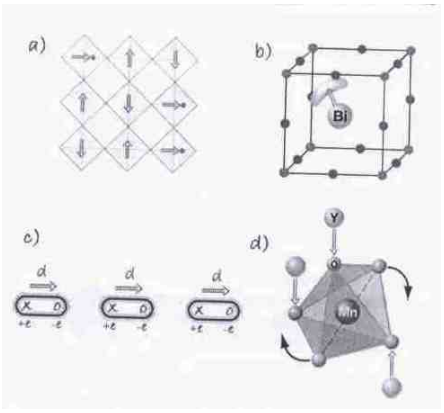

Figure 3.1: Different microscopic mechanisms found in type I multiferroics a) "Mixed" perovskites with ferroelectrically active d^0 ions and magnetic d^n ions. Horizontal arrow depict the shift of the d^0 ions with respect to the oxygen octahedra, which lead to ferroelectricity and the vertical ones correspond to the coexisting magnetic order. b) In those materials the ordering of lone pairs (like the lobe around the Bi ion) lead to the ferroelectricity. c) In charge ordered systems, the coexistence of inequivalent sites with different charges, and inequivalent (long and short) bonds, leads to ferroelectricity d) In "geometric" multiferroics like the one in the picture a structure change (for example a tilting) results to the appearance of dipole moments, which interacts with one another and lead to ferroelectricity.

Multiferroic perovskites

We know many magnetic perovskites and ferroelectric ones but what is striking is that that there is almost zero overlap between these two types of ordering. This rather peculiar incident has its origin at the electronic structure of each one of the two cases of perovskites. Certain perovskites exhibit magnetism due to a partially filled d shell of a transition metal ion. On the other hand ferroelectricity occurs in those systems by an off-center shift of the transition metal ion with respect to the oxygen octahedra due to a softening of a transverse optic phonon. The transition metal is strongly bonded to the oxygens via an empty d shell so this attribute plays a crucial role to the onset of a ferroelectric transition. One might think that a magnetic and a ferroelectric ordering are two mutually exclusive cases at those materials because of the different electronic configurations they demand. But there are other ways around it such as the use of magnetic rare earths elements as an

A-site ion or the production of mixed crystals with two types of transition metals, one with empty and another with partially filled d shells.

Ferroelectricity due to lone pairs

In this type of materials (for example $BiFeO_3$) there are ions with two outer 6s electrons which do not participate in chemical bonding but, due to the fact that they have a high polarizability, they play a major role in the origin of ferroelectricity.

Ferroelectricity due to charge ordering

For some compounds a charge ordering occur under certain conditions. Especially at those compounds, which have transition metals with different valences, there might be after the charge ordering an nonequivalency between both the sites and the bonds and this might lead to ferroelectricity. For example $TbMn_2O_5$ and some nickelates $RNiO_3$ belong to this category.

"Geometrical" ferroelectricity

In those materials (such as $YMnO_3$) there is a geometrical change (tilting, rotation etc), which provides close packing and as a result we have an approach of an anion with a cation. This results to a dipole moment providing the necessary condition for a ferroelectric transition.

3.1.2 Type II mulriferroics

Spiral multiferroics

In this subgroup belong the vast majority of type II multiferroics such as $TbMnO_3$, $Ni_3V_2O_6$ and $MnWO_4$. The occurrence of ferroelectricity in those materials is associated with a spiralling magnetic phase. One type of this spiralling magnetic phase is a sinusoidal spin density wave where all spin point in one direction but their magnitude vary in a sinusoidal manner. Because of the centrosymmetric nature of this type of spin wave it is not compatible with a ferroelectric ordering. Another possibility is a cycloid where the wave vector Q describing the propagation of the spin wave and the rotation of the spin are co-planar. This type of spin wave gives a non zero polarization described by the following formula $P \sim Q \times [S_i \times S_j]$ where S_i, S_j are neighboring spins. The microscopic mechanism of this polarization is associated with spin orbit interaction. This formula was deduced by Katsura, Nagaosa and Balatsky via a microscopic approach and by Mostovoy by a phenomenological one.

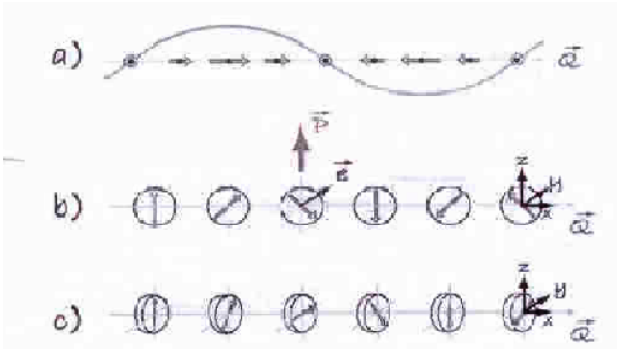

Figure 3.2: Different types of spin waves a) sinusoidal spin wave, in which spins point along one direction but vary in magnitude. This structure is centrosymmetric and consequently not ferroelectric b) The cycloidal spin wave. The spins rotate at x-y plane and there is a non zero P_z polarization. c) In "proper screw" type the inversion symmetry is broken. Despite that, in most cases no polarization is been produced.

Considering this equation the so called "proper screw" where the spins rotate in a plane perpendicular to the one containing the wave vector Q should not give a polarization. That is the case for particular crystal symmetries such as the cubic but, for other symmetries, the equation might not hold and so even proper screw type spin waves might give a non zero polarization.

Multiferroics with collinear magnetic structure

The second group of type II multiferroics have all their magnetic moments aligned to a particular axis and the polarization arises from magnetic striction due to the difference of the magnetic coupling with atomic position. The simplest example of this category is Ca_3CoMnO_6. Specifically when those materials are magnetically ordered a polarization arise due to a difference between ferro- and anti-ferromagnetic bonds with respect to an exchange striction.

Chapter 4

Review of the material

4.1 Crystallographic structure

Europium titanate crystallizes under normal conditions at the cubic perovskite structure with lattice constant a=3.904 A. The europium atoms occupy the simple cubic sites, the oxygens occupy the center of the faces and the titanium atoms are at the center of the oxygen octahedron.

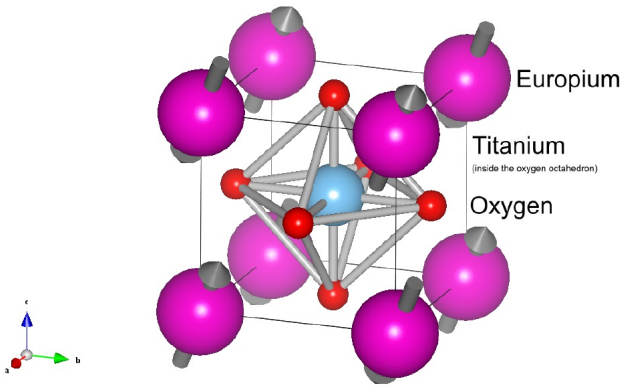

Figure 4.1: Single unit cell of europium titanate. At ambient conditions europium titanate has a cubic perovskithe structure with europium ions at the corners of the cube, oxygens at the center of the faces and the titanium ions in the center of the oxygen octahedron. The arrows represent the magnetic moments of the europium ions [15]

4.2 Magnetic and dielectric properties

4.2.1 Magnetic properties

Europium titanate has been found to order antiferromagnetically with Neel temperature $T_N \approx 5.5 \pm 0.2K$ [15], [26]. At this antiferromagnetic state europium ions occupy two interpenetrating fcc sublattices with each europium ion having 6 antiferromagnetically coupled nearest neighbors and 12 ferromagnetical coupled next nearest neighbors. Antiferromagnetic ordering is believed to arise due to the superexchange interaction via an intermediate ion. Magnetic measurements have indicated a $\chi^{-1} \sim (T - \theta)$ dependence as shown in the next figure. A fit to high temperature data gave a Curie-Weiss temperature with positive value θ=4.5 K and a Curie constant of 7.46 cm^2K/mol. The fact that the Curie-Weiss temperature is positive is a characteristic of ferromagnetic behavior. This unusual positive paramagnetic temperature with the appearance of an antiferromagnetic transition may be understood in terms of the exchange couplings expressed as [15]

$$T_N = \frac{2S(S+1)}{3k_B}(-J_1 z_1 + J_2 z_2)$$
$$\Theta = \frac{2S(S+1)}{3k_B}(J_1 z_1 + J_2 z_2)$$

where J_1 and J_2 are the nearest and next nearest exchange constants whereas z_1 and z_2 are the nearest and next nearest number of neighbors. The nearest neighbor antiferromagnetic is approximately half the strength of the next nearest neighbor ferromagnetic interaction. So we can imagine the antiferromagnetic ordering of $EuTiO_3$ as result of the antagonism of those two mechanisms. Eu^{2+} has half filled 4f configuration which lead to antiferromagnetic superexchange interaction (figure 4.3). This is because the virtual hopping leading to kinetic superexchange can take place only if the two magnetic spins are antipararel. On the other hand the ferromagnetic interaction arises from a virtual 2p to 5d transition from a filled 2pshell to the empty 5d shell and a subsequent 5d-4f interaction between the virtually excited 2p electrons and the 4f spins. For example in EuO the ferromagnetic interaction is induced by virtual transitions from the full 2p shell to the empty (5d-6s) and a subsequent polarization of the f shells in the excited state. This mechanisms dominates the superexchange interaction. On the other hand in Eu^{+2} perovskites (as $EuTiO_3$) the antiferromagentic superexchange interaction competes with the ferromagnetic one.

Below 15K there is a strong anisotropy in the magnetic properties as shown in figure. Also in this figure 4.7 there is a magnetic feature at ∼3K.

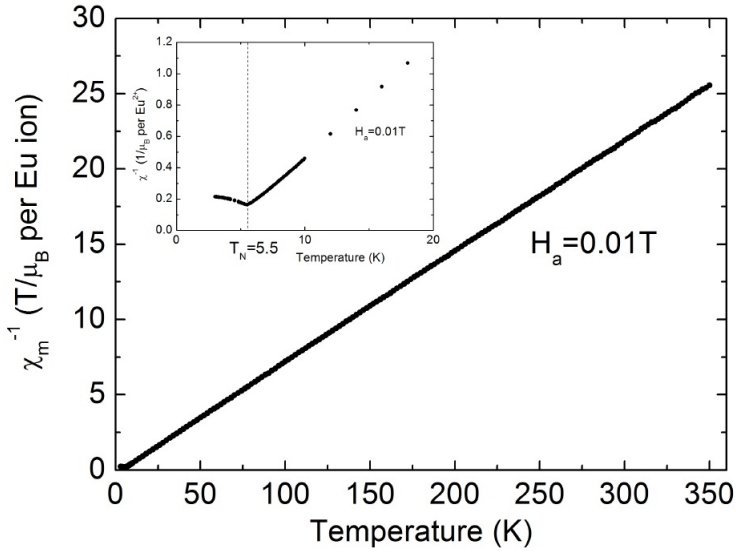

Figure 4.2: Temperature dependence of the inverse magnetic susceptibility in $\mu_0 H_0 = 0.01T$[15]

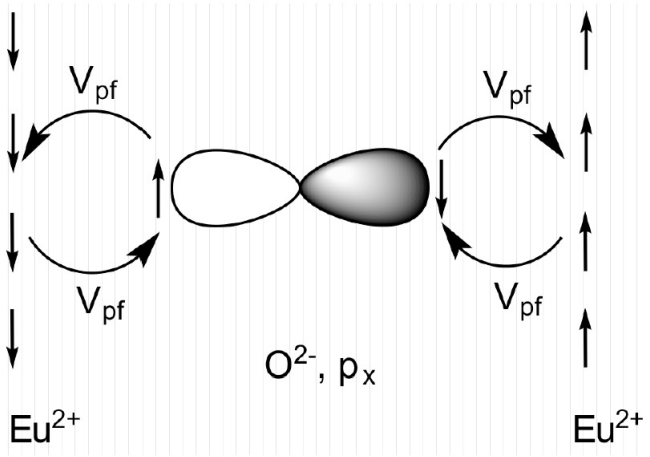

Figure 4.3: Schematic representation of the next nearest neighbors antiferromagnetic superexchange in the 180^0 configuration.

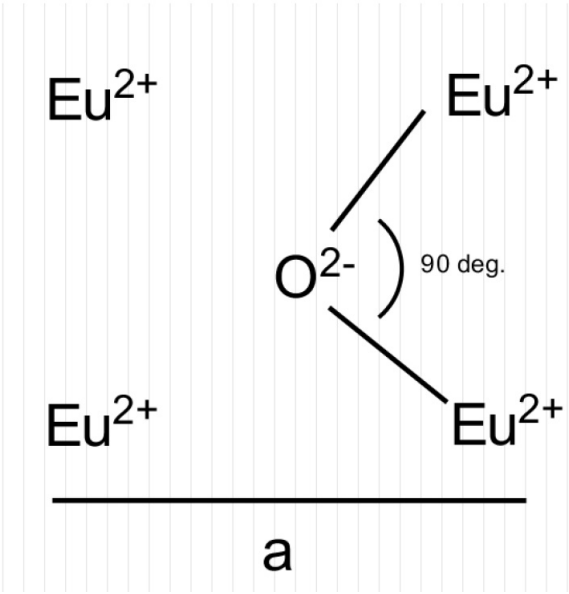

Figure 4.4: Schematic representation of the exchange interaction 90 degree configuration in $EuTiO_3$

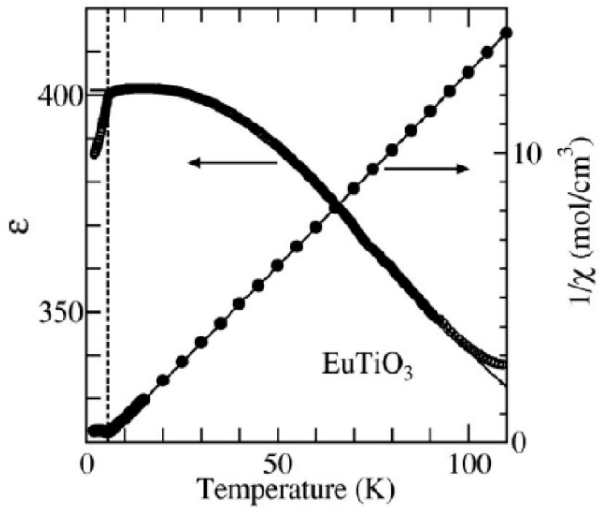

Figure 4.5: Dielectric constant measurement at 100kHz and inverse susceptibility of $EuTiO_3$. [15]

This low temperature feature has been attributed to a first order phase transition from c-axis antiferromagnetic order to ab-plane one [15]. The splitting

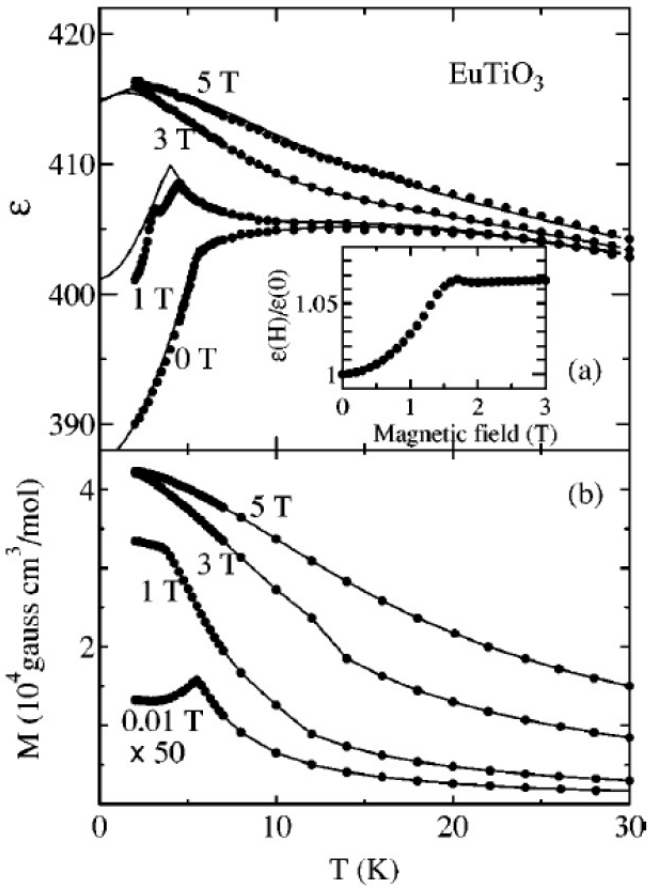

Figure 4.6: Magnetoelectric coupling at low temperatures: a) dielectric constant at 1kHz. b) magnetization in several magnetic fields. The inset shows the magnetic field dependence of the dielectric constant at 2 K normalized to its zero-field value. [15]

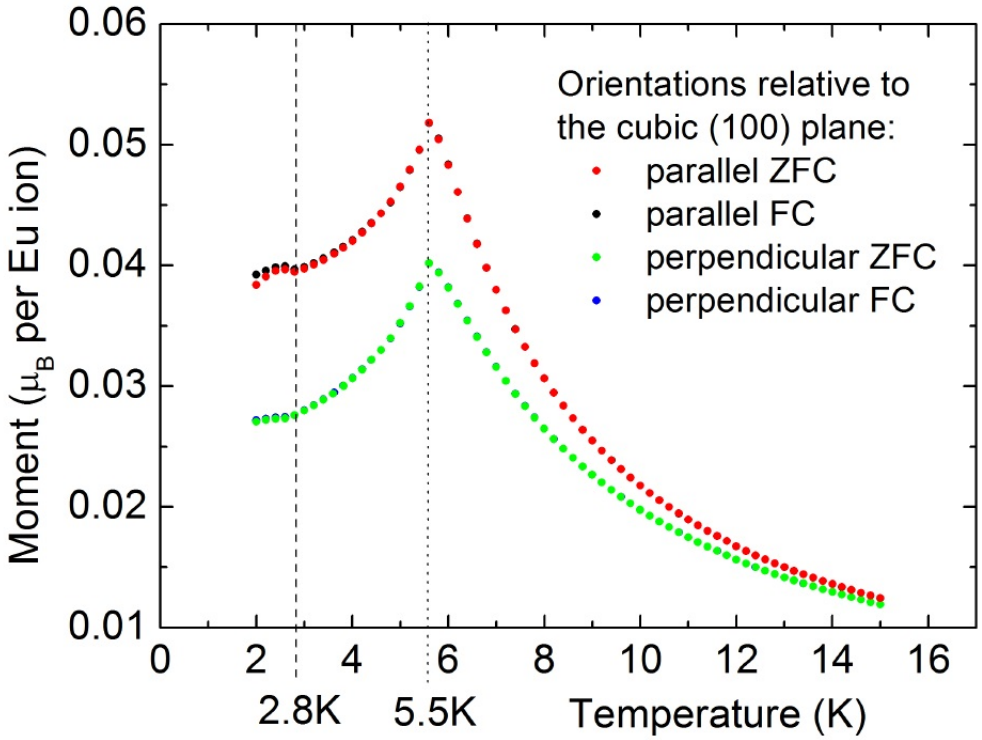

Figure 4.7: Magnetic anisotropy with an onset below 15 K. The measurements were taken with $\mu_0 H_0 = 0.01T$. The antiferomagentic transition at 5.5 K and the 2.8 K shoulder are visible. ZFC and FC stands for zero field cooled and field cooled representing the two different cooling protocols that were used. The magnetization reaches different values with each one of them. [15]

may be understood through the existence of a ferromagnetic component of the magnetization within the antiferromagnetic phase.

4.2.2 Dielectric properties

Low temperature measurements of the dielectric constant has shown a linear increment below 100 K and a saturation point at T$\sim$ 30 K with $\epsilon \sim$ 400. The Barret formula [15] fits best the temperature dependence of the dielectric constant:

$$\epsilon(T) = A + \frac{C}{[(\frac{T_1}{2}) \cdot \coth(\frac{T_1}{2T})] - T_c} \tag{4.1}$$

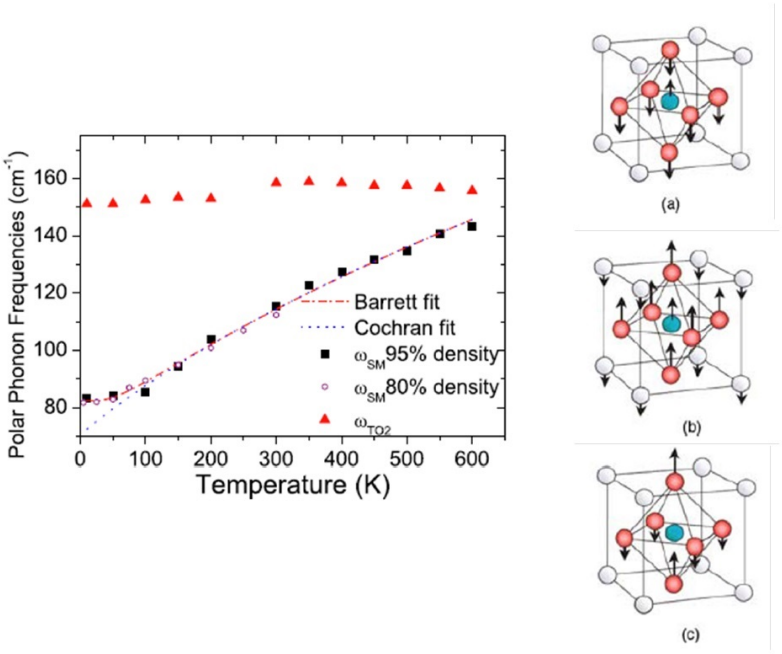

Figure 4.8: Left: The temperature dependence of the two transverse optic modes. The softening of the TO1 mode is apparent as well as its saturation. Lines represent different fits to the data. Right: Schematic of the three q=0 transverse optic modes. a) TO1, b) TO2, c) TO4. [8]

where $A = 181, C = 2.34 \cdot 10^4 K^{-1}, T_1 = 162K$, and $T_c = -25K$ indicating a possible antiferroelectric ordering [15]. At very low temperatures the dielectric constant decreases with the onset of antiferromagnetism at 5.5 K. A fully polarized state appears at 1.5 T and 2 K with the full $7\mu_B$ moment of the europium anions. The dielectric constant has $\epsilon(H_a)/\ \epsilon(H_0))$=7% at 2K, a quantum paraelectric behavior up to 1.5 T, and a double peak structure at intermediate field values. The increment of dielectric constant with the applied magnetic field causes a mode hardening, which drives the system away from any long range order. The correlation of the dielectric constant with nearest neighbors spin could be formulated with the following formula [15] $\epsilon(T, B) = \epsilon_0'(T)(1 + \alpha < S_i \cdot S_j >)$ where $\epsilon_0'(T)$ is the bare dielectric constant and α is the coupling constant between i, j nearest neighbors spins.

Infrared reflectivity and time domain transmission measurements revealed three q=0 phonons. The first one (TO1) (in order of increasing frequency) is the movement of titanium anions against the movement of the oxygen octahera, the second one (TO2) is the movement of the europium anions against the oxygen octahedra, and the third one (TO4) is the octahedra

bending (see Fig.4.4). The most interesting is the first phonon since it is the soft mode which drives the ferroelectric transition. The TO1 softens with decreasing temperature and saturates below ∼30 K (see Fig.5.4). The application of the classical Cochran formula for the paraelectric phase yields :

$$\omega_{SM}(T) = \sqrt{C(T - T_c)} \tag{4.2}$$

where C=(27.06 ±0.8) $cm^{-2}K^{-1}$ and T_c=(-184.5 ± 15.4) K. The fact that the soft mode does not actually freeze is attributed to the effect of quantum fluctuations [15]. This explains the low temperature saturation of the soft mode and that the temperature dependence cannot be described better by the Cochran law at this range of temperature but it can be fitted best by the Barret formula with parameters C=(27.45 ±1.3) $cm^{-1}K^{-1}$, T_1=(154.6 ± 9.8) K and T_c=(-170 ±29.3) K [15].

In figure 4.9 we observe broad frequency-dependent maxima in the real part of the dielectric function and associated features in the imaginary part. Those features shift to higher temperatures with increasing frequency and the peaks of the real part of the dielectric function broaden.

At extremely low temperatures we can see in figure 4.11 evidence of quantum paraelectric behavior of $EuTiO_3$ due to the saturation of the real part of the dielectric constant at high values below ∼ 30 K. Also high frequency permitivity contribution to the dielectric constant as extracted from IR reflectivity measurement shows purely quantum paraelectric behavior as shown in figure 4.12 .

In figure 4.13 we can see that there is a kink in the dielectric constant associated with the antiferromagnetic transition at T_N=5.5 K whereas the lower temperature slope change is most probably a signature of the uncovered magnetic anisotropy discussed earlier. The kink in the dielectric constant presented at Neel temperature is an evidence of the magnetoelectric coupling which give us a hint about the multiferroic nature of $EuTiO_3$.

4.3 Structural phase transition

Powder X-ray diffraction showed a structural phase transition when the temperature is lowered [15] as shown in Figure 4.14. The two (002) split peaks show a 1/2 intensity ratio suggesting a transition into a tetragonal phase. So the initial cubic space group Pm-$\bar{3}$m to the tetragonal I4/mcm [15]. This structural phase transition is an antiferrodistortive one which has to do with an antiphase (between neighbor oxygen octahedras) tilting of the oxygen octahedra and has to do with the softening of a zone corner (at the R and M points of the brillouin zone) acoustic mode [23],[22], [25], [20]. From

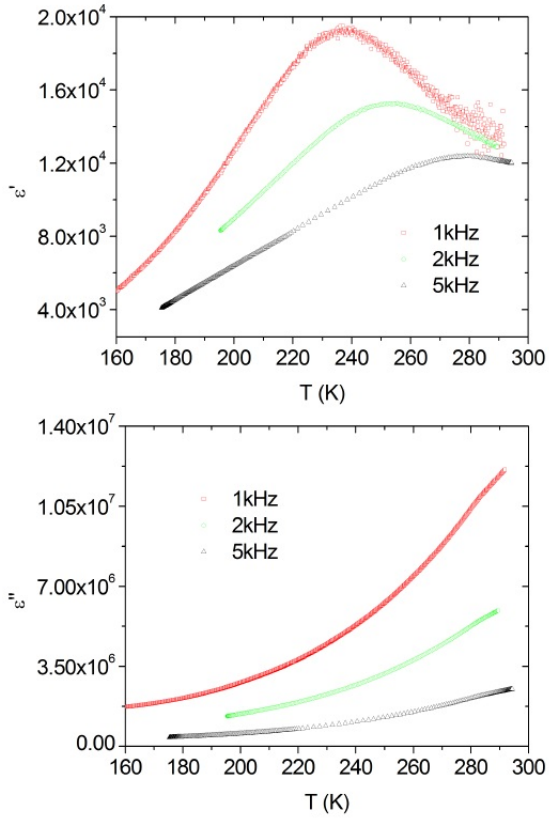

Figure 4.9: Temperature dependence of the real and imaginary part of the dielectric function for different frequencies. The $\epsilon^{'}$ maximum occurs at T$\approx$ 240 K for the lowest frequency of 1kHz and gradually shifts towards higher temperatures with increasing frequency [15]

.

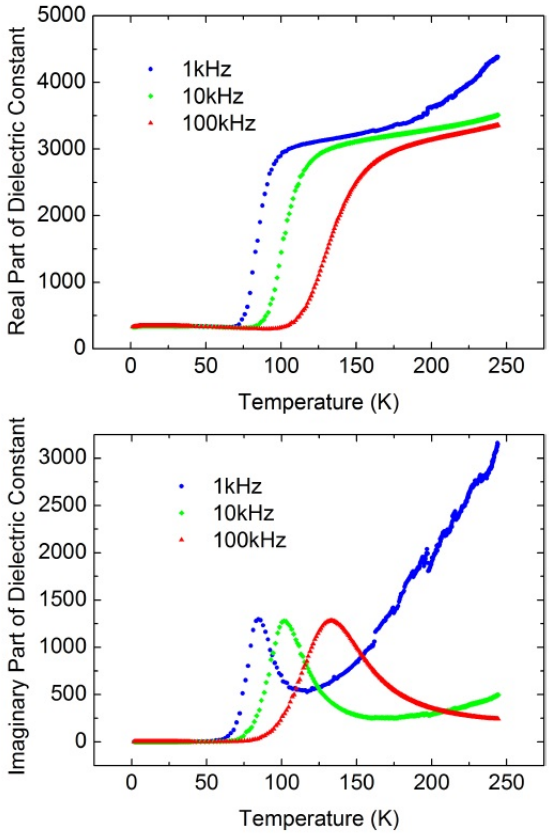

Figure 4.10: Broad step like features in the real part of the dielectric constant. Frequency dependent maxima in the imaginary part of the dielectric constant. An external variable voltage with amplitude of 10^{-2} -1 V (corresponding to $\sim 10^{-1}$-10 V/cm) seems to has no effect [15]

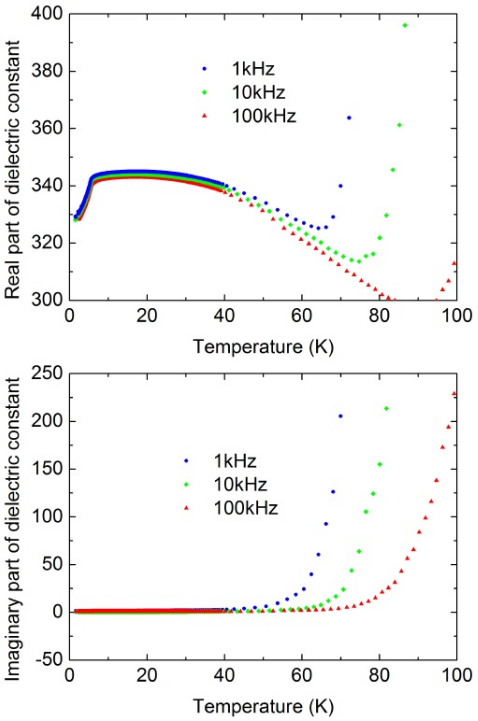

Figure 4.11: The real and imaginary part of the dielectric function at low temperatures. We can see the saturation of the real part at around 30 K which is an evidence of quantum paraelectric behavior of $EuTiO_3$ [15]

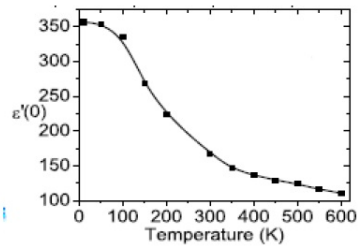

Figure 4.12: The real part of the dielectric constant extracted from FIR results for f >100 kHz [15]

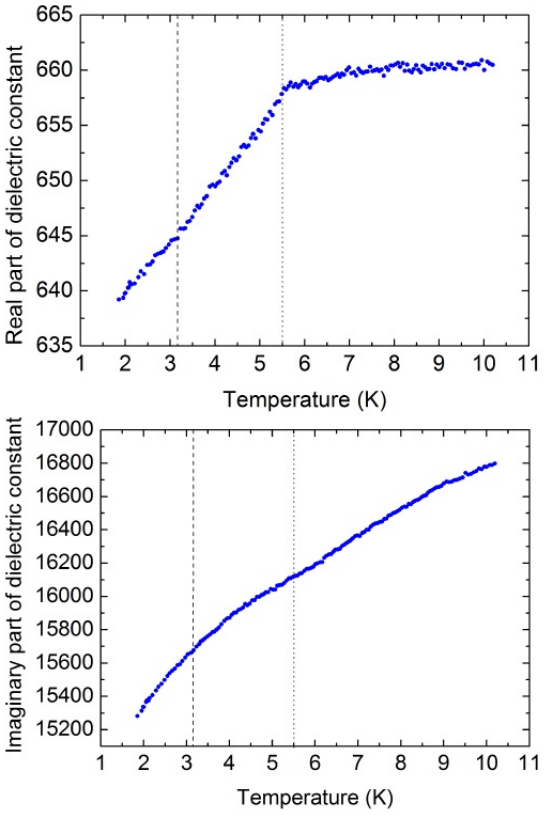

Figure 4.13: The low temperature evolution of the dielectric constant. As a trend $\epsilon^{'}$ decreases gradually on lowering temperature below T_N. The higher temperature kink is associated with the antiferromagnetic transition at T_N=5.5 K whereas the lower temperature slope change present itself most probably due to the magnetic anisotropy discussed earlier. [15]

all the octahedra tilt patterns the ones with the lower energies are the already mentioned I4/mcm tetragonal phase, the orthorombic Imma and the rombhedral R$\bar{3}$c. The inversion symmetry seems to be retained in the average global tetragonal phase. However there is no need to remove the inversion symmetry in order to interpret those results. The α axis length shows a sharp decrease and is smaller compared to $SrTiO_3$ below 200 K. Consequently the tetragonal strain is bigger in $EuTiO_3$. Figure 4.15 shows the temperature dependence of the α axis length [15]. Also the c length is presented which does not show any significant temperature dependence. Site group analysis gives the following optical phonons (in the Γ point of the Brillouin zone) for each one of the three crystal systems [20]. In the cubic structure we have $3F_{1u}+F_{2u}$ modes in total. From those the triple degenerate F_{1u} modes are IR active and the F_{2u} is silent. Following the Brillouin zone folding in the cubic to tetragonal transition we acquire: $5E_u+3A_{2u}+A_{1g}+3E_g+2B_{1g}+2A_{2g}+B_{2g}+A_{1u}+B_{2u}$ for the tetragonal 4/mcm space group. In the tetragonal phase we have $5E_u+3A_{2u}$ eight IR active modes, $A_{1g}+3E_g+2B_{1g}+B_{2g}$ seven Raman active modes and $2A_{2g}+A_{1u}+B_{2u}$ four silent modes. In the orthorombic phase (Imma space group) we have $5B_{1u}+4B_{2u}+4B_{3u}+3A_g+3B_{2g}+4B_{3g}+2A_u+2B_{1u}$ modes in total. From those the thirteen $5B_{1u}+4B_{2u}+4B_{3u}$ are IR active modes , the twelve $3A_g+3B_{2g}+4B_{3g}+2B_{1u}$ are Raman active modes and two $2A_u$ modes are silent. In the rhombohedral phase (R$\bar{3}$c space group) we have $5E_u+3A_{2u}+A_{1g}+4E_g+3A_{2g}+2A_{1u}$ modes. The eight $5E_u+3A_{2u}$ modes are IR active, the three $3A_{2u}+A_{1g}$ modes are Raman active and the five $3A_{2g}+2A_{1u}$ modes are silent. The measured transition temperature varies from 200 K to 283 K or even room temperature.There are some hints that the tetragonal phase might be slightly more energetically favorable in comparison to the cubic structure. The I4/mcm structure is $\sim$ 27 meV per formula unit lower in comparison to the Pm $\bar{3}$m, the orthorombic Imma $\sim$ 26 meV per formula unit lower and the rhombohedral R$\bar{3}$c is 25 meV per formula unit lower [21]. The small energy differences make us expect the coexistence (especially near 300 K) of those structural phases in the same system.Experiments have shown that the crystal quality (oxygen vacancies, trivalent europium ions, fluctuations of lattice parameters and strains) can alter significantly the antiferrodistorsive transition temperature [20]. It is well established that this antiferrodistorsive order competes with the (anti)ferroelectric transition arising from the off centering of the B-site ion (in the case of $EuTiO_3$ the titanium anion) in tetravalent perovskites. In some XRD spectra there were seen satellite peaks which were not part of the spectrum corresponding to the tetragonal phase. A possible explanation is that those satellite peaks result from a long range modulation of the antiferrodistortive octahedral rotation [24]. The movement of the oxygens perpendicular to the axis of rotation is

constrained to 1/2 due to the fact that each oxygen is shared with the neighbor unit cell. Diffuse scattering associated to the (001/2) ordering, which is in conjunction with the antiferodistortive ordering, is attributed to antiferroelectric distortions arising from the titanium displacements [24]. In figure 4.16 we clearly see the competition between those different kinds of ordering. The short range AFE ordering rises where the AFD ordering is minimum. The two kinds of ordering achieve stability via the formation of the superstructure shown in figure where the two instabilities are alternatively interwoven. The correlation length f the AFD ordering is $\sim$ 11 nm(28 unit cells) and $\sim$ 22 nm (56 unit cells) parallel and perpendicular to the rotation axis whereas the correlation length of the FE ordering is only $\sim$ 6 unit cells [24]. Also the modulated AFD ordering showed large time constant meaning that there is a dynamic process where the system fluctuates between the modulated AFD and the AFE order whereas a simple AFD ordering is a static effect. The simple AFD structure disappears at $\sim$106 K whereas the modulated AFD structure persist up to $\sim$ 285 K [24]. These competition between the two types of ordering can be harnessed in order to control the topography of the antiferrodistortive domains. The application of an external electric field (and a perpendicular magnetic field) ensures that there would be a tendency towards the formation of domains with the rotation axis perpendicular to the external electric field [26] as shown in figure 4.17.

The interatomic distances within the unit cell as a function of temperature are shown in figure4.18 . The T1-O1 distance (where O1 is the oxygen in the apical position of the octahedron) decreases with temperature in the cubic phase and then increases shadowing the α-axis tetragonal distortion commented above. The Ti-O1 and Ti-O2 distances split below the tetragonal phase transition temperature reflecting the basal oxygen O2 displacement. The Eu-O2 and Eu-O2$'$ denote the near and far distances following the octahedral rotation. The Eu-O1 distance remains fairly temperature independent. In perovskites, the out of phase tilting angle ϕ of the TiO_6 octahedra (calculated from the values of the x[O(2)] position with tanϕ= 1-4x[(O2)]) has been proposed as the primary order parameter for the Pm-3m to I4/mcm structural phase transition. In figure4.19 we can see the temperature dependence of the $EuTiO_3$ order parameter alongside with the $SrTiO_3$ data. The octahedral rotation angle ϕ increases with decreasing temperature and appears to be saturating around 60 K [15]. The value of the distortion amplitude is almost double that found in $SrTiO_3$ at the lowest temperatures reported.

The heat capacity of a $EuTiO_3$ single crystal at temperatures between 0.385 K and 300 K and with a magnetic field applied parallel to the (100)

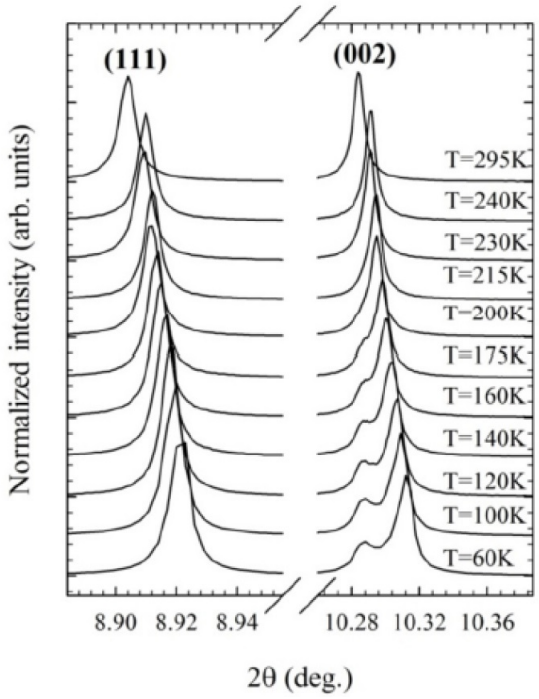

Figure 4.14: Temperature evolution of the Miller index (111) and (002) obtained via powder X-ray diffraction. The peak splitting of the (002) at about 200 K gives us a hint about a cubic to tetragonal structural phase transition

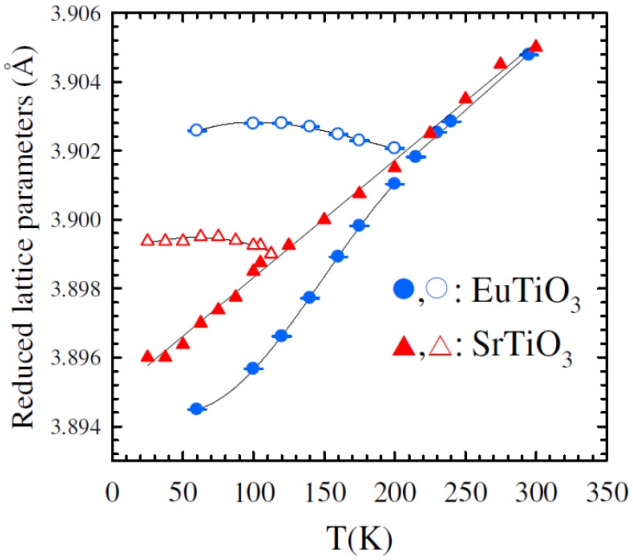

Figure 4.15: Reduced lattice parameters of $EuTiO_3$ and $SrTiO_3$ as a function of the temperature. The full and open circles are α- and c- axis of the $EuTiO_3$, respectively. Full and open triangles correspond to the α- and c-axis of $SrTiO_3$

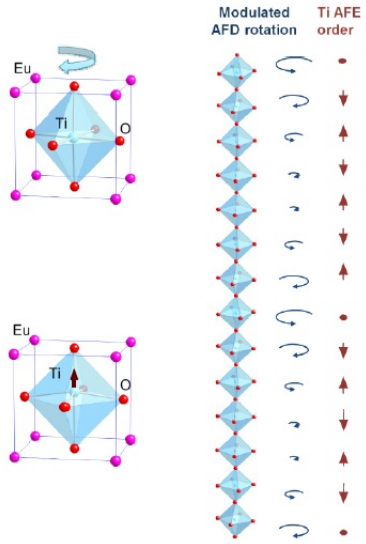

Figure 4.16: Illustration of the modulation of the antiferrodistortive titling of the oxygen octahedra in comparison with the antiferoelectric displacement of the titanium anions [24]

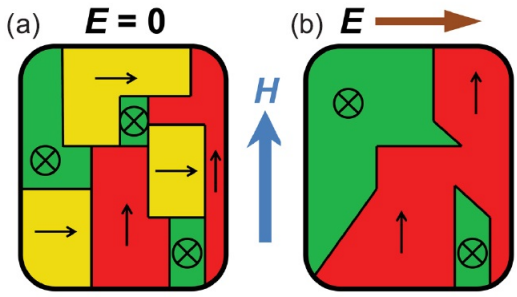

Figure 4.17: Zero-electric field cooling exhibits many orthogonal domains, whose c-axis orientations are indicated by arrows and shading. When a magnetic field H is applied domains with c⊥H (shaded green and yellow) will undergo a spin-flop transition. Cooling in an electric field E realigns structural domains with c\\E reducing the total proportion of the crystal with c⊥H and hence suppressing the spin flop. [26]

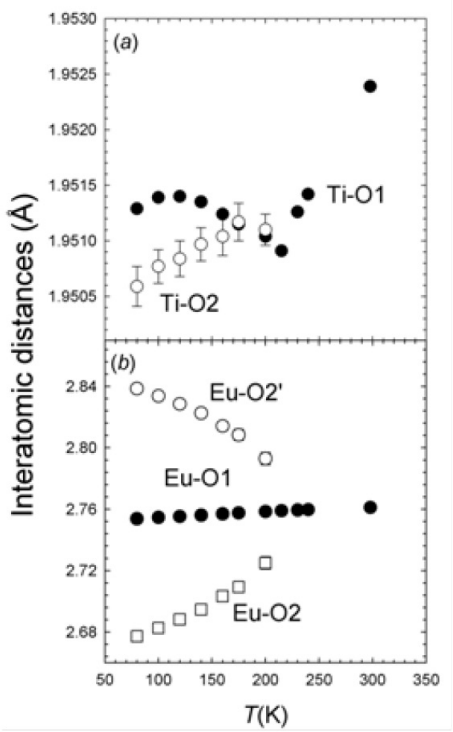

Figure 4.18: The interatomic distances within the unit cell as a function of temperature. O1 is the oxygen in the apical position whereas O2 is the basal plane oxygen in the octahedron. The Ti-O1 and Ti-O2 splitting follows the tetragonal distortion below the transition temperature. Eu-O2 and Eu-O2$'$ reflects the oxygen octahedron rotation [15]

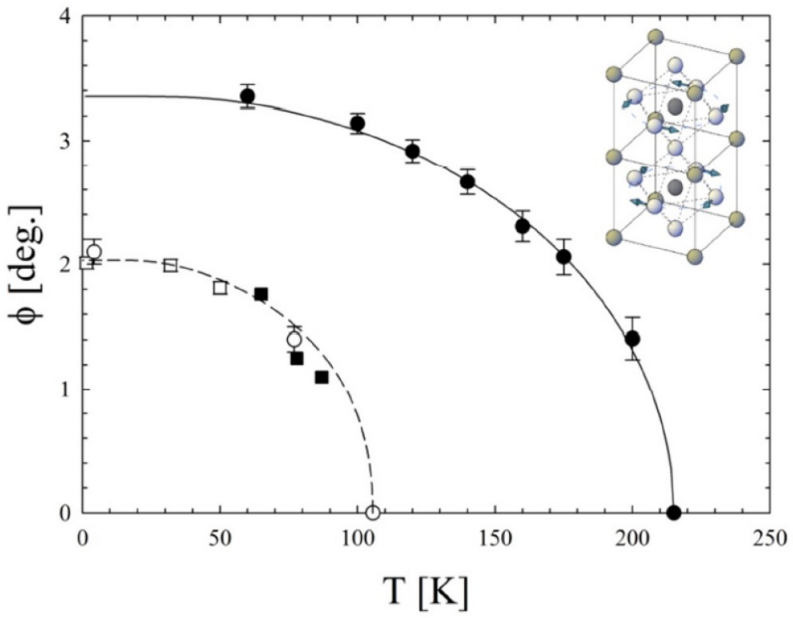

Figure 4.19: In this figure we see the angle of the oxygen octahedra ϕ. Full circles represent results for $EuTiO_3$. Open circles, open squares and full squares represent data from three studies of $SrTiO_3$. The inset depicts the mode corresponding to the oxygen displacements [15].

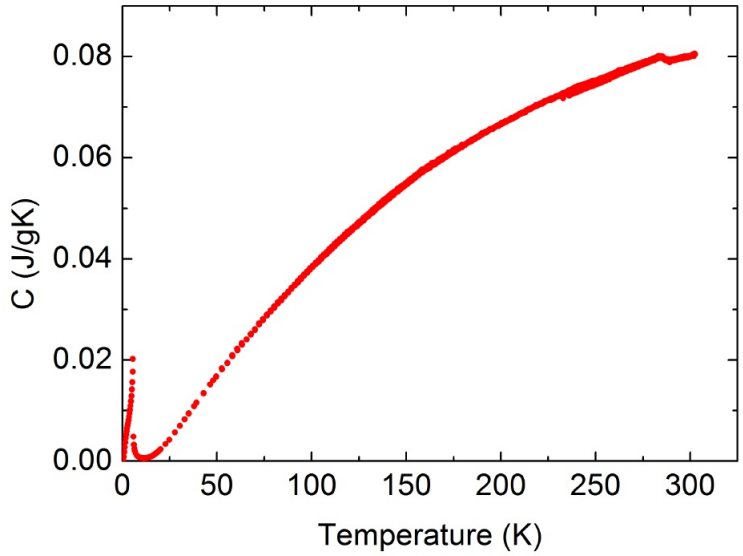

Figure 4.20: Zero magnetic field specific heat capacity of single crystalline $EuTiO_3$ as a function of temperature [15]

plane is presented in figure 4.20 . At very low temperatures we can see a $C_V \sim T^3$ temperature dependence followed by a crossover to the classical behavior at $\sim$ 3 K . This crossover can be attributed to the magnetic anisotropy mentioned above. In figure 4.21 we can see clearly a peak at 284 K corresponding to the structural phase transition.

One interesting thing is that there is a discrepancy between the transition temperature measured with X-ray diffraction ($\sim$ 200 K)and the heat capacity method ($\sim$ 283 K). The tilting angle is found to be randomly distributed (for temperature higher than 200 K) from one nanoregion to the next averaging out to a cubic space group. On further decreasing the temperature the correlation length of the tetragonal tilting diverges so the instruments resolution starts to pick up the distortion. So this discrepancy can be attributed to the scale evolution of the correlation length of the structural phase transition [15].

4.4 Spin-lattice coupling

Strontium Titanate is a well studied incipient ferroelectric. So, it is reasonable to look for a new compound which might incorporate the ferroelectric qualities of strontium titanate as well as magnetic ordering. That is the rea-

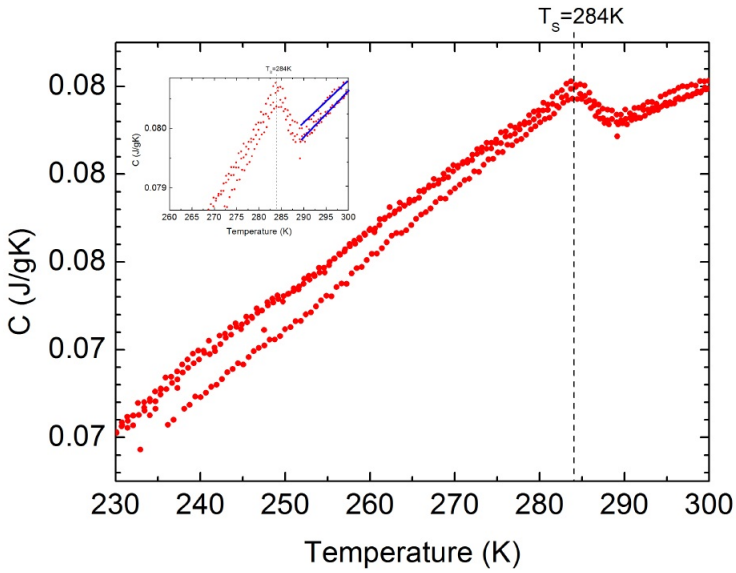

Figure 4.21: The heat capacity data as seen in the vicinity of the structural phase transition. A relaxation trend is present above and below the structural transitions. On cooling from room temperature the first two series of datapoints have lower values compared to the third. This relaxation trend vanishes at the transition and is reversed below. This relaxation trend could be attributed to the existence of local structural distortions terminating at the temperature corresponding to the appearance of the structural order parameter or the observed effect may be attributed to metastable phases coexisting within this region of the phase diagram [15].

son why ($EuTiO_3$) is of such interest. The reason why it is believed that europium titanate would have the same ferroelectric behavior as strontium titanate is because the two materials share a remarkable amount of similar properties [9]. They are both cubic at ambient conditions, they have similar lattice constants, they exhibit a tetragonal phase transition with lowering temperature, and both have a Ti^{4+} inside a oxygen octahedra as well as A^{2+} cation on the A-site. One major difference is the presence of $4f$ electrons in europium titanate (which make it magnetic also). The fact that $4f$ electrons are well localized and shielded by the much "larger" $5s5p$ electrons ensures a great similarity between the electron band of the two materials. Moreover the antiferrodistortive continuous structural transition that both materials undergo (and makes them tetragonal) differ greatly at the temperature of transition (100K for strontium titanate and almost 300K for $EuTiO_3$). One other striking difference is the great discrepancy between the dielectric constants: $SrTiO_3$ has $\epsilon \sim 10^4$ at low temperatures when $EuTiO_3$ has only $\epsilon \sim 10^2$. Despite some differences it is more reasonable to expect that $EuTiO_3$ would also be an incipient ferroelectric so the question is : why bulk $EuTiO_3$ does not exhibit ferroelectricity? Recent theoretical studies [28] from first principles calculations have revealed a giant spin-lattice coupling which is responsible for the absence of a distinctive ferroelectric transition for a bulk $EuTiO_3$. A Hubbard model was used for the 4f electrons of europium. In figure 4.23 we see that the frequency of the soft mode is being affected severely be the change of the Hubbard potential; a result peculiar because the soft mode is driven by the off centering of the titanium cation and so there is no obvious reason why it is so sensitive to the energy of the Eu bands. A logical explanation is that there is a spin lattice coupling with the 4f orbital playing a role in this. As shown in figure 4.24 there is a hybridization between Eu-f orbitals and the unoccupied Ti-d orbitals. This hybridization creates also a pathway for the superexchange interaction which leads to the antiferromagnetic ordering.

What is even more interesting is that this hybridization depends on the Hubbard potential applied to the Eu-f states as shown in figure 4.25. This dependence brings out the underlying physics of the spin-phonon coupling.

Considering the maximally localized Wannier functions (MLWF) in Figure 4.26 we see two examples of (MLWF) for the occupied f orbitals. The cubic harmonics corresponding to those orbitals are proportional to $z(4y^2 - x^2 - z^2)$ and xyz respectively. The more interesting of the two is the f_{xyz} because, except from the main lobes that are around the core, there is a small but nonzero part of the lobes around the Ti cation, which presents exactly the hybridization of Eu-f orbitals and the normally unoccupied Ti-d orbitals.

So the key question is how exactly this orbital hybridization affects the

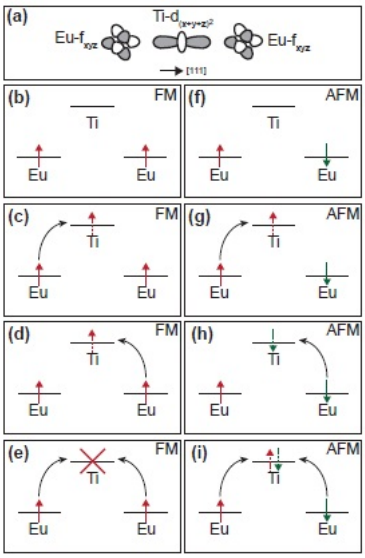

Figure 4.22: a) f_{xyz} orbital and 3^{rd} neighbor Eu ions with the intermediate titanium $d_{(x+y+z)^2}$ orbital. b) energy level of the three orbitals in the ferromagnetic configuration. c), d) lowest excitations where one electron hops onto the Ti cation. e) forbidden configuration due to the Pauli exclusion principle. However in the antiferromagnetic case also the i) configuration is allowed [28].

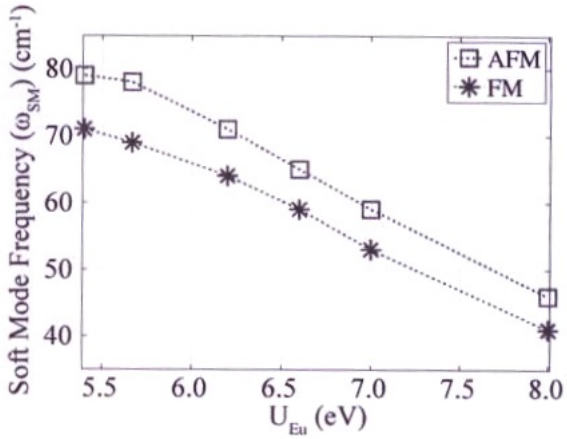

Figure 4.23: Polar soft mode frequency vs U_{Eu} for the Eu-4f orbitals [28]

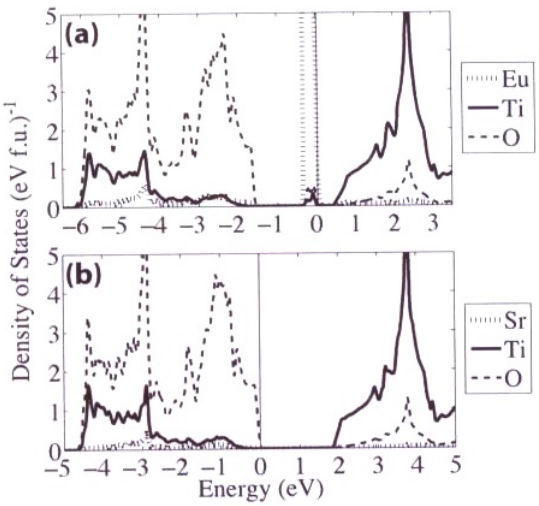

Figure 4.24: Comparison of the density of states between strontium titanate and europium titanate. One striking difference is the presence of a sharp peak corresponding to europium 4f orbitals just below Fermi level with some non-zero but smaller contributions from oxygen and titanium. This gives us the impression that the Eu-4f orbital hybridizes with both O and Ti atomic orbitals [28].

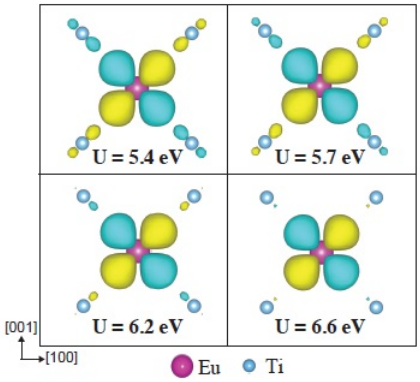

Figure 4.25: The MLWF of the europium f_{xyz} for different values of U_{Eu}. It is clear that as the potential increases the lobes near Ti shrink and consequently the hybridization decreases [28].

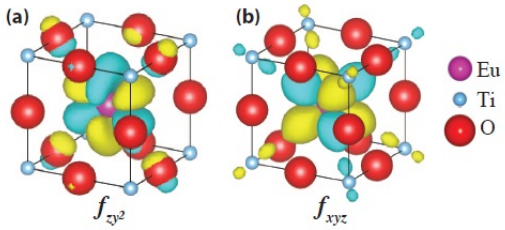

Figure 4.26: Two maximally localized Wannier orbitals of europium f electrons a) $f_{zy^2} \sim z(4y^2 - z^2 - x^2)$ b) $f_{xyz} \sim xyz$. Yellow and green parts of the Wannier functions correspond to isosurfaces of opposite sign [28].

soft mode frequency. The displacement of the Ti towards one of the oxygens increases the Ti-3d/O-2p hybridization and therefore the hybridized empty states are moving to higher energies while the occupied ones to lower energy, which leads to a tendency towards ferroelectricity. On the other hand when we have also a Eu-4f/Ti-3d hybridization the 3d orbital is not empty, and there is an additional energy cost which inhibits ferroelectricity (the same argument applies if the B site ion was magnetic) [13].

Chapter 5

Experimental methods

5.1 Experimetal apparatus

The apparatus consists of a T64000 Jobin-Yvon micro-Raman triple spectrometer equipped with a CCD detector. For the excitation an Argon laser was used. We have used mainly the 514.5nm line for our measurements.

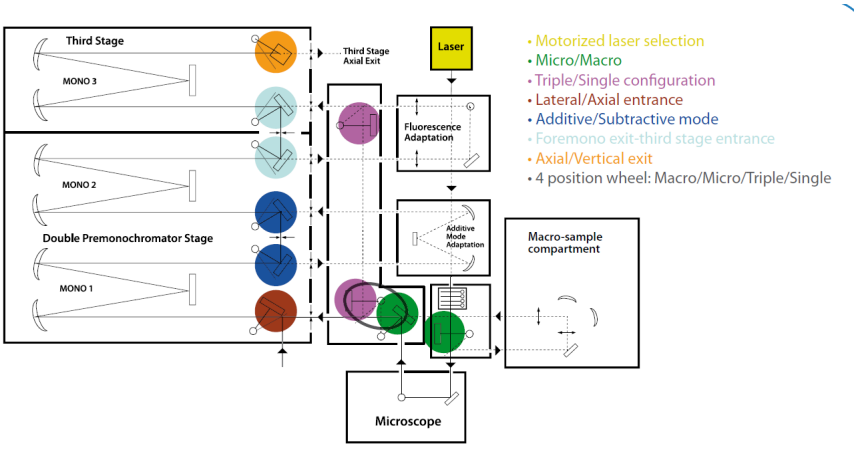

Figure 5.1: The main component of the T64000 Jobin Yvon triple spectrometer. We clearly see the three stages of the spectrometer, which are three monochromators in line. In the course of this experiment we used only the micro- Raman configuration.

The spectrometer

A monochromator is a configuration, which is used to analyze polychromatic light. It consists of some mirrors that guide the light in and out and

the main component is a grating (usually diffractive but it can also be reflective). The light after the grating is dispersed so it is analyzed to different wavelengths. Usually two or three monochromators are used in a typical Raman spectroscopy configuration. The triple spectrometer can be used in two different configurations, the additive and the subtractive. These two configurations correspond to the way the dispersed light from the first and the second grating reaches the third one. With the subtractive configuration the light after the second grating is collimated and it is dispersed again when it reaches the third grating. In the subtractive configuration we acquire a wide spectrum as the frequency is concerned. Practically in this configuration the first two stages just play the role of a 'filter' for the laser line.

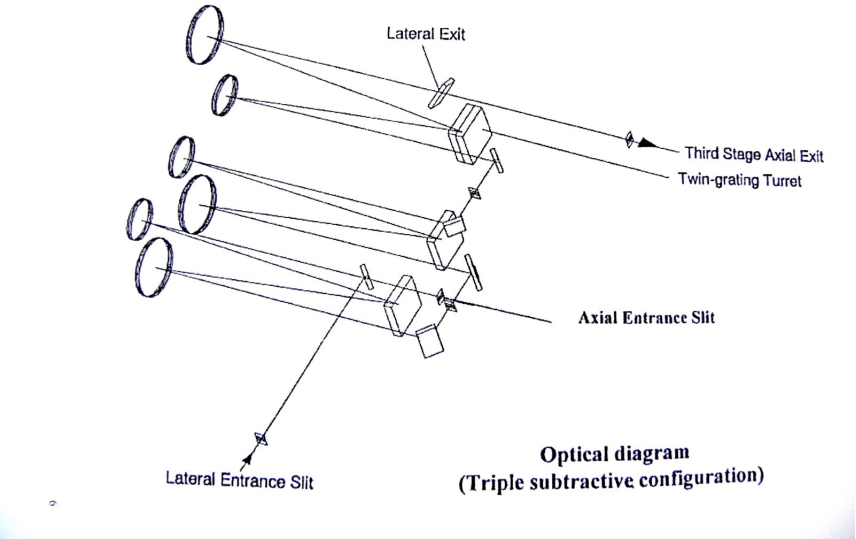

Figure 5.2: The subtractive configuration

In the additive configuration the light gets dispersed in every grating so at the end we have a spectrum which has very good resolution but it is not so wide. We used for our experiments exclusively the subtractive configuration.

Laser and optics

The laser we used was an Argon laser. The 488 nm, 514.5 nm lines are the more intense, but we exclusively used the 514.5 nm line. After the laser there was an attenuator to reduce the laser intensity to an accepted level so that no local heating of the sample is induced. The laser emits also plasma

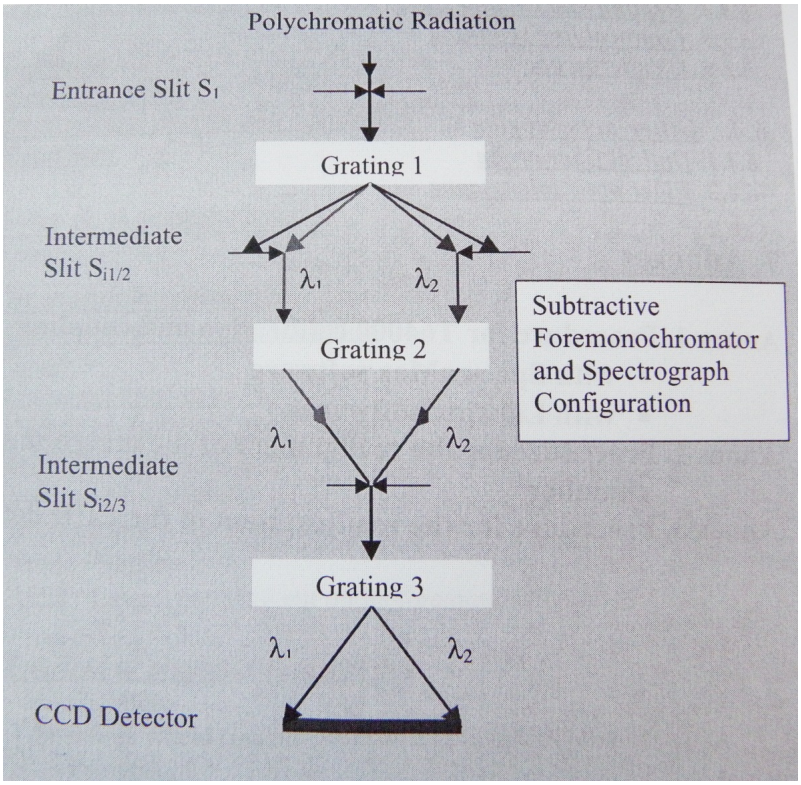

Figure 5.3: The way the light is dispersed in the path through the spectrometer when we use the subtractive configuration. We see how after the second grating the light is re-collimated

lines due to transitions of the argon ions inside the optical cavity. Those plasma lines correspond to additional peaks which can be detected in the spectrum. Furthermore there is a continuum signal due to the cathode discharge. It is crucial to cut off those noises from our spectrum so we used a SPEX 1450 tunable excitation filter. This filter consists of a mirror that increases the spot size of the laser before it hits the diffraction grating. The grating had 1200 grades/nm and 12.7 $\times$ 12.7 nm dimensions. It works for wavelengths between 400-633 nm and it has a bandwidth of 0.5 nm. After the light is dispersed from the grating it hits a mirror, which refocuses it and then passes through a slit, which 'cuts' the plasma lines. We can choose which wavelengths are excluded by micrometric movements of the diffraction grating. After the plasma line filter there is a compensator, which enabled us to choose the polarization of the incident light. Furthermore we can use an analyser after the microscope in order to choose scattered light with a given polarization. This enables us to apply selection rules for the Raman

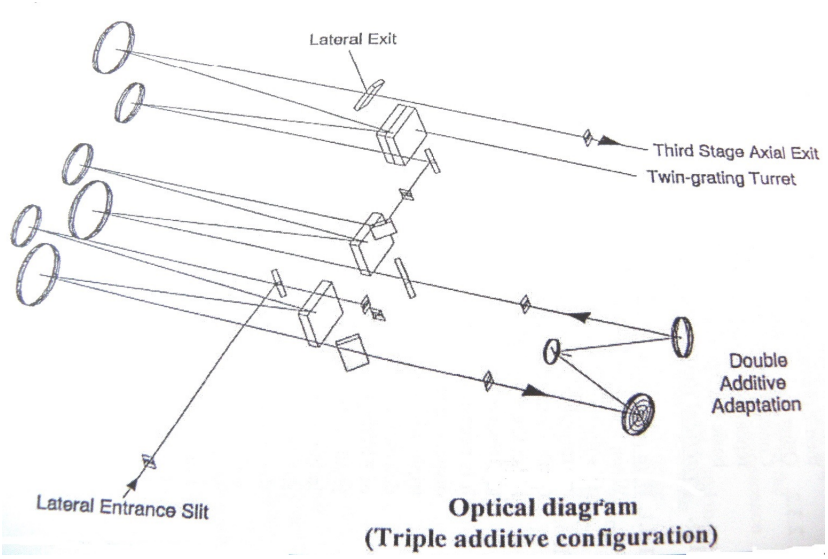

Figure 5.4: The additive configuration

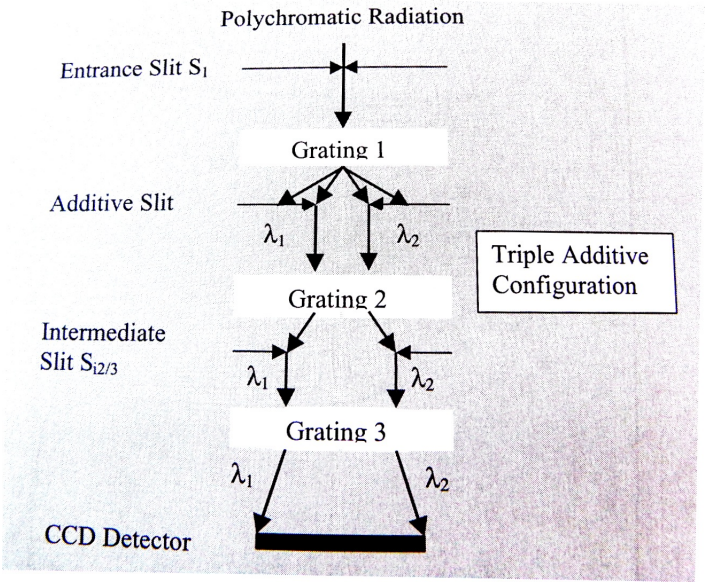

Figure 5.5: The way the light is dispersed in its path through the spectrometer when we use the additive configuration

scattering and measure specific elements of the Raman tensor. This means that we can detect phonons with different symmetry if we choose the incident light polarization properly. The spectrometer responds differently to different polarization of the incoming light. The key factor is whether the light

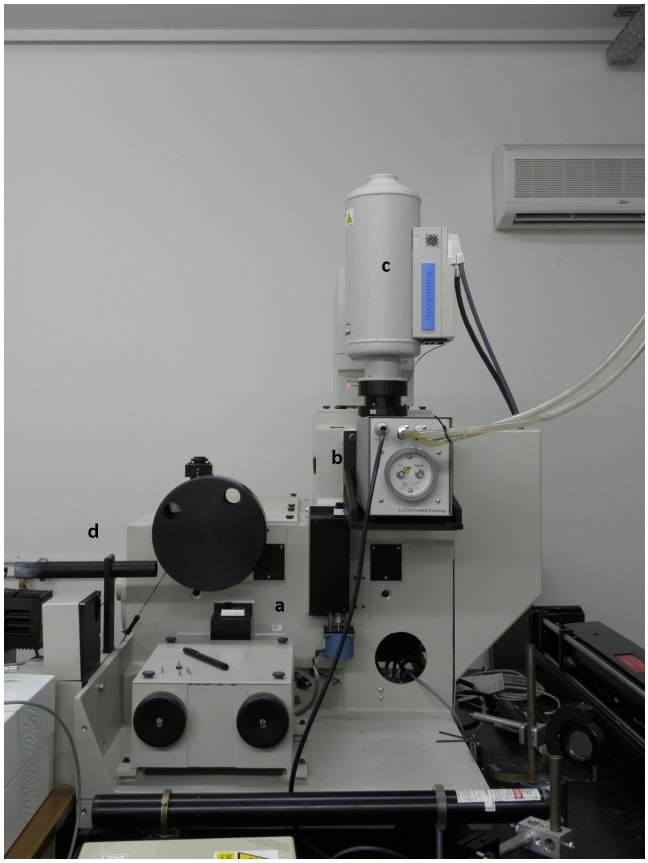

Figure 5.6: a) The first two monochromators b) the third monochromator c) The CCD and its liquid nitrogen dewar d) The light entrance from the microscope

polarization is vertical or parallel to the gratings. It is important to know for a given laser line which orientation suffers from the low response of the spectrometer in order to extract correct information from the measurements.

5.2 Direct current apparatus

The idea behind this apparatus was to connect the sample with a DC source and let a small current pass through. This current would correspond to an electric filed inside the sample as the formula $\overrightarrow{J} = \sigma \overrightarrow{E}$ postulates. So the sample was glued on a plastic plate and two copper wires glued on it with a conductive paint. Later due to the fact that the samples resistance is significantly lowered with the application of voltage an in-line 560 Ω resistor was added in order to limit the current. Also the sample and the resistor were

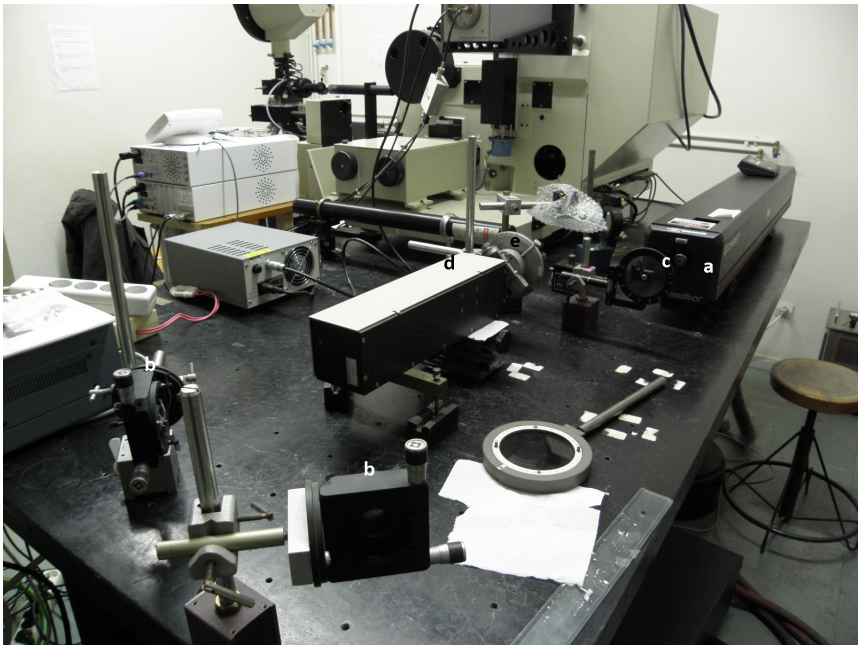

Figure 5.7: a) Laser tube. b) Mirrors. c) Compensator. d) Plasma line filter. e) Polarizer.

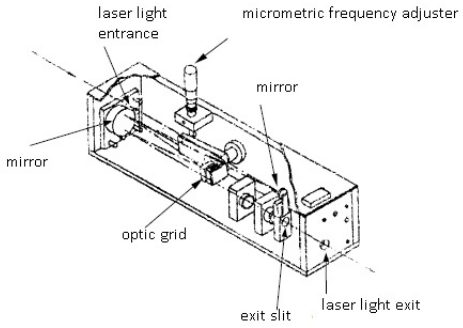

Figure 5.8: The plasma line filter.

placed on a piece of a PCB board. The DC source had maximum output 30 V so we did our measurements in a 0-30V range with 1V step. The voltage source had a built-in voltmeter and an amperometer but we have used also an amperometer in series to monitor the μA passing current that was too small compared with the built-in instrument's sensitivity.

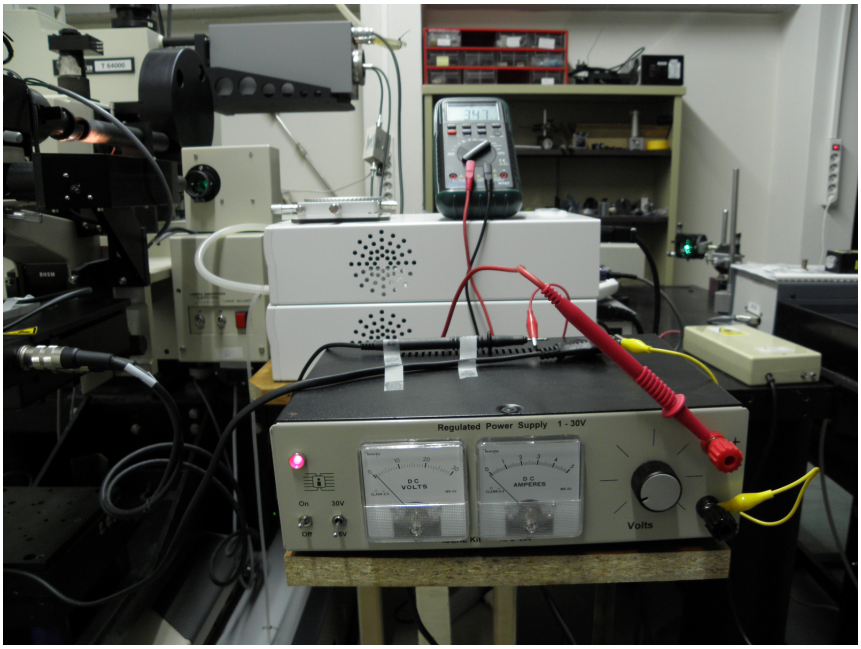

Figure 5.9: DC Power source with maximum output 30V-DC and an in series amperometer to monitor the current.

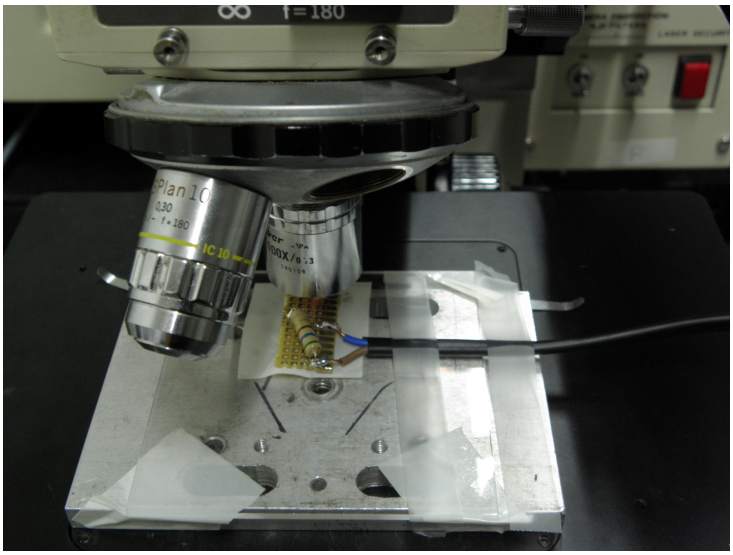

Figure 5.10: The apparatus with the in line compliance resistor. The sample is under the lens.

5.3 High electric field measurements

The high voltage apparatus had three main components. The first one was a DC high voltage power supply which was part of a He-Ne laser. We

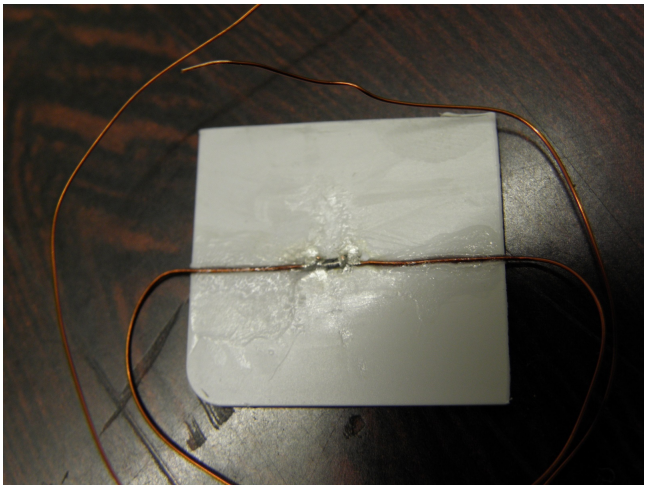

Figure 5.11: The sample is between the two wires and conductive contact was established with the use of conductive paint at the edges of the sample where the wires were glued.

calculated that the maximum voltage output was approximately 9.430 kV. The second component was a voltage divider which was made by twelve 1.2 MΩ resistors soldered in line. The voltage divider gave us the opportunity to select the voltage that we wished to apply on our sample. The last part was the electrodes which were put inside a type of rails in order to adjust the distance between them. At first the distance was set to 1 cm. One electrode could be moved in order to tune the distance between them. The electrodes were glued on a piece of plexiglass to ensure the electrical insulation of the apparatus against vertical discharges to the metallic base of the microscope.

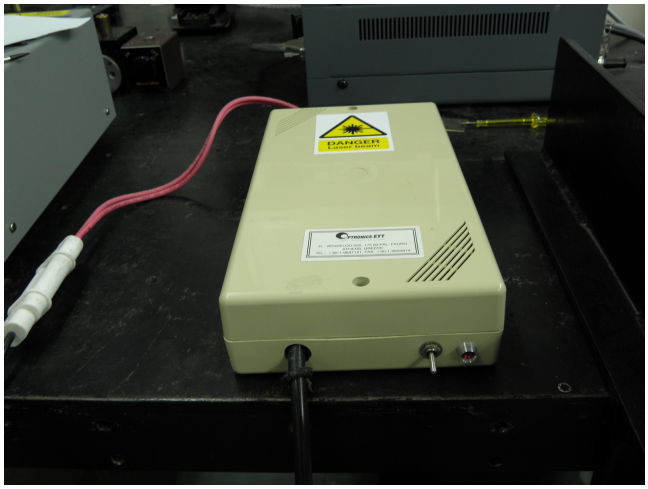

Figure 5.12: DC power supply which provides the high voltage to our apparatus.

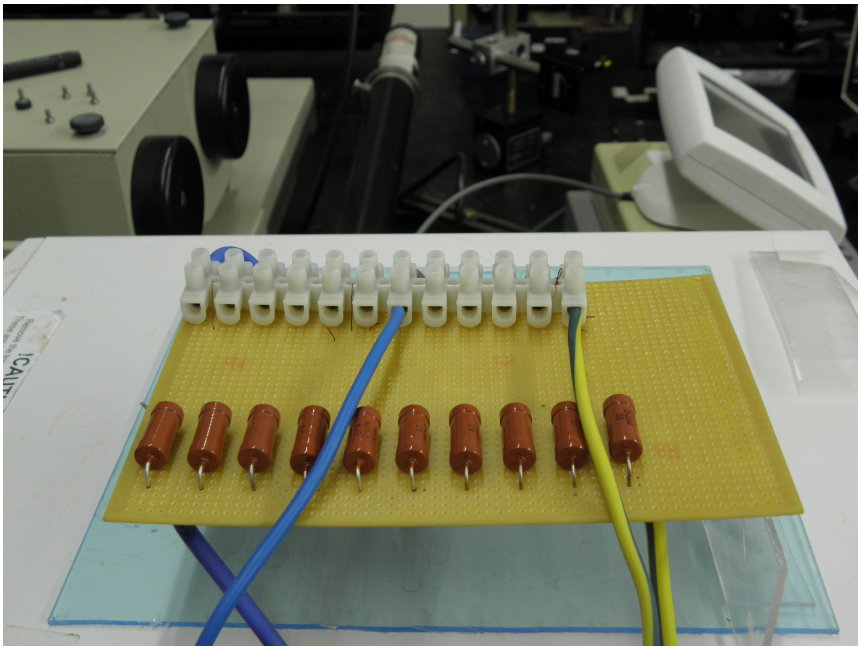

Figure 5.13: The voltage divider. The two cables shown were connected to the electrodes and by choosing different inputs we could adjust the output voltage.

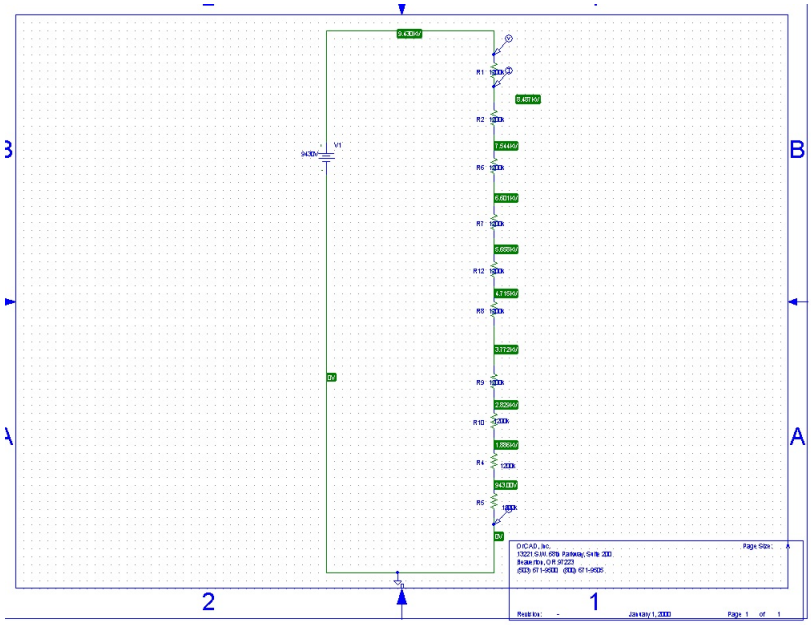

Figure 5.14: This is the schematic of the voltage divider, which was simulated with the SPICE suite. The voltage at the ends of every resistor is 943V. We see the different voltages that we can acquire.

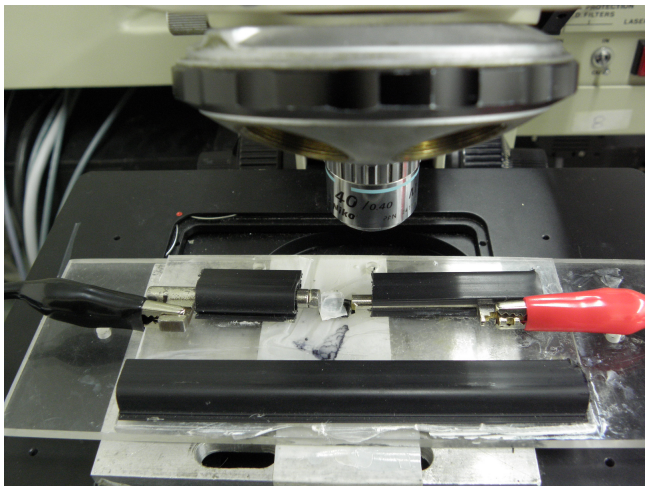

Figure 5.15: The electrodes. Between them the sample was placed. A small piece of plexiglass was used to adjust the height of the sample to the most homogeneous place of the field.

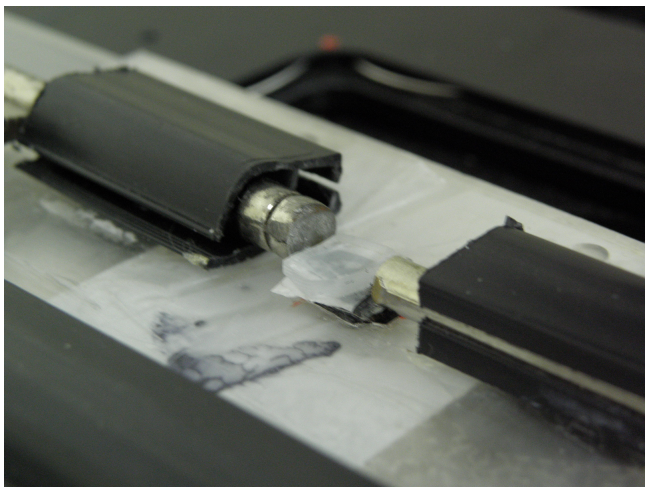

Figure 5.16: Close-up of the electrodes.

Chapter 6

Results and discussion

6.1 The sample

Basically we had two samples the first one was a small single crystal and the second one was a large polycrystalline. The polycrystalline sample was cut in two (Figs 6.1 - 6.2), with one piece polished (thus thinner than the other one). The whole sample had electric resistance of 1KΩ and its dimensions were approximately 1.64 cm in length, 0.25 cm in width, and 0.14 cm in height. So we can estimate that the resistance of each piece has value half of that of the whole piece. Both the single crystal and the polycrystalline are black and opaque. Under the microscope we were able to see little well oriented crystallines (on the polycrystalline sample), which were shiny and therefore easily spotted among the black rest of the sample's surface. Their dimensions varied from few microns to some tens of microns. The single crystal was a cubic piece of a few hundred microns. It was also polished and so it appeared uniformly lustrous under the microscope.

6.2 Intrinsic spectrum and first efforts

The Raman spectra should not show any peaks as expected due to the fact that each site in the unit cell is an inversion center. Therefore we expect three IR active modes at: 110 cm^{-1}, 160 cm^{-1}, and 530 cm^{1}. Those frequencies have been obtained from IR reflectivity measurements [7]. The direct application of voltage upon the sample limited significantly the volts that we could apply. This happened because the sample exhibits a significant decrease in its resistance when an external voltage is applied, which leads to overheating. The voltage that could be applied without overheating was less than 8 volts. Electrical measurements were done in order to un-

Figure 6.1: The unpolished sample. Its length was approximately 0.8 cm.

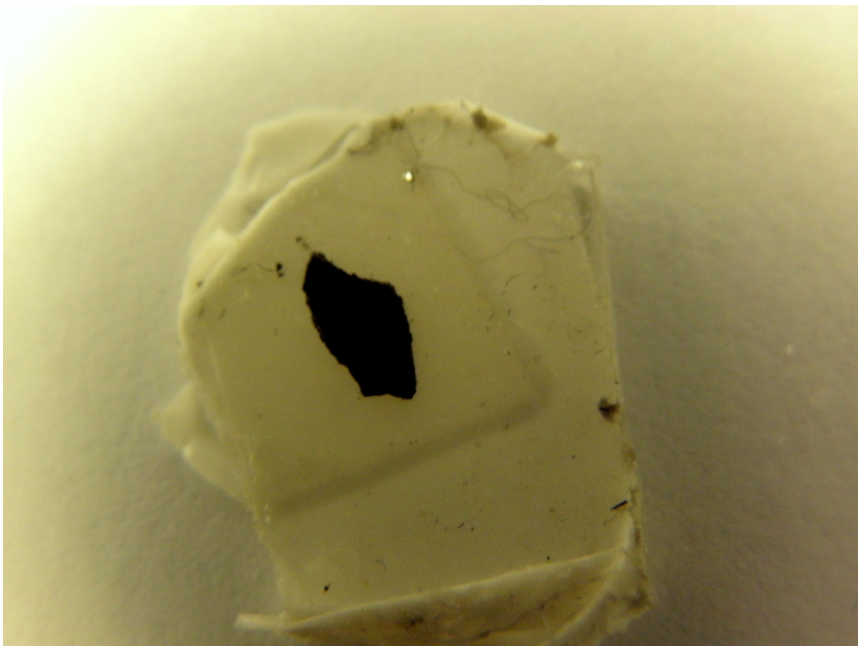

Figure 6.2: The polished sample. Due to the polishing the sample was significantly reduced in size, it became much thinner in comparison to the other piece.

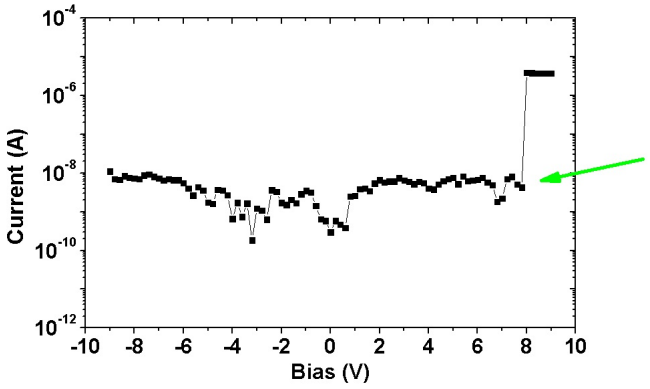

Figure 6.3: The decrease in resistance manifests itself as a 'jump' in the current at 8 volt. For the measurements, we did not make special electric contacts on the sample but instead we touched directly the electric pins on the surface. This definitely introduced some parasitic phenomena but still provides a qualitative information about the electric response of the sample.

derstand if this overheating was indeed part of the response of the material to the voltage. Indeed a rapid decrease in the resistance (almost by three orders of magnitude) was observed for 8 volt bias (figure 6.3). In figures 6.4 and 6.5 we see no significant change in the spectra of the materials with the application of the voltage. There is no new peak appearing or other spectral modification indicative of a symmetry breaking. Apparently, the electric field induced inside the material was not strong enough to induce any symmetry breaking. Therefore, a much more stronger electric field was needed.

In order to avoid the high currents from the lowering of the resistance, a resistor was introduced in series. In this way, higher voltages could be reached.

6.3 High voltage measurements

Unpolished sample

For these measurements we took spectra from those crystallites of the sample that were well oriented with respect to the incident light polarization. They had smooth shiny surfaces reflecting more light. We have tried to choose crystallites as big as possible in order to avoid loosing them during the measurements and also we have chosen crystallites whose surfaces were as reflective and homogeneous as possible.

As shown in figure 6.6 the spectrum with no external field did not show

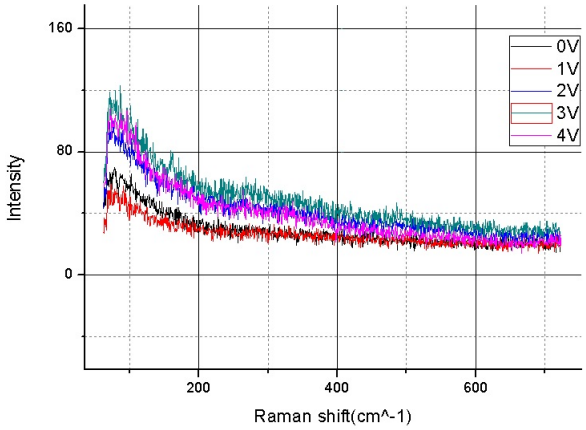

Figure 6.4: Those spectra were taken with the direct current apparatus. No radical change was observed.

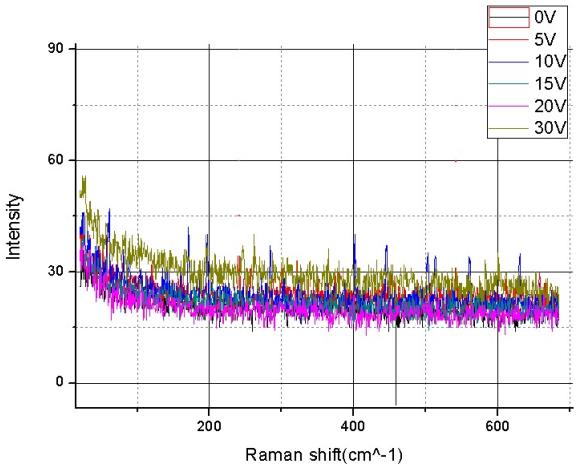

Figure 6.5: This figure corresponds to the direct current apparatus with the in line compliance resistor and the 30 V DC power supply. Again no significant changes were observed. For the 30 V we see something like a broad peak at ~ 100 cm^{-1} but this must be something random because it had never be seen afterwards, under the same conditions neither from a different crystalline.

any peaks or spectral modifications. When the high voltage source were turned on at ~ 6.5 kV the spectrum showed the peaks depicted in figure 6.7. The same peaks were shown in spectra from other crystallites from different parts of the sample. Besides, when the electric field was applied the sample was turning trying somehow to align itself with the applied field. Once the field was applied for the first time and the sample was reoriented, switching it off and on did not induce any movement of the sample. This happened in all relative measurements forcing us to believe that the application of the electric field really induced a polarization of the material accompanied with the expected symmetry lowering.

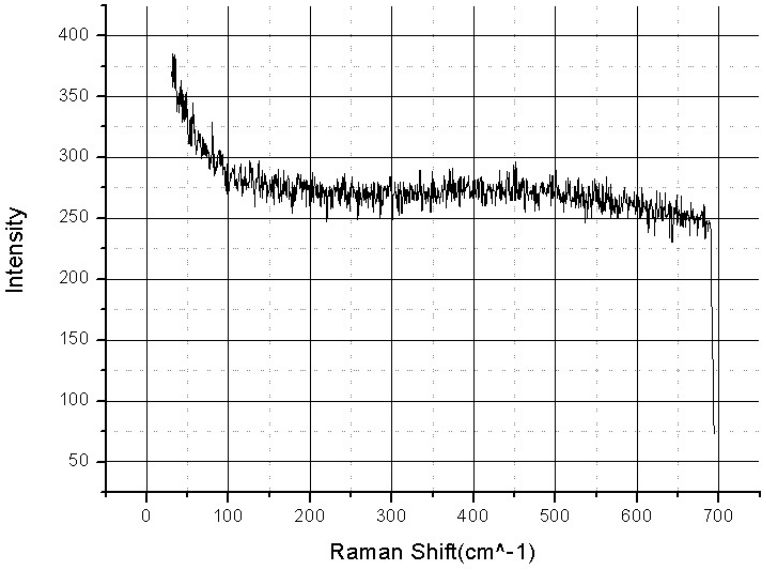

Figure 6.6: Spectrum of sample with no applied field

In Fig. 6.8 we present the data from a sample that was modified by the application of an external field of 6.5 kV/cm. As can be seen (Fig. 6.8) the effect of the electric field is not permanent but it fades out after some time. Two days later the spectral modifications in the recovered sample could not be induced even by applying a much higher electric field of 9kV/cm. Meaning that those crystallites, which initially gave spectra like in Fig. 6.7 did not show any new peaks nor did the same peaks reappeared with the application of the electric field. It must be pointed out that this sample was also used in the direct current measurements, so it had been already exposed to some electric field, which of course was small in comparison to that used for inducing spectral changes. It is possible that the previous treatment of the material might have affected its behavior.

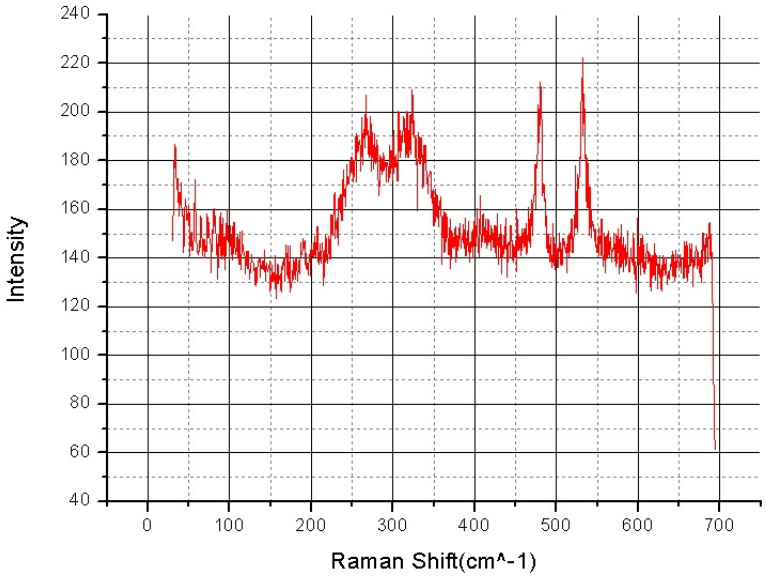

Figure 6.7: Same crystalline and accumulation time with the application of 6.5kV/cm

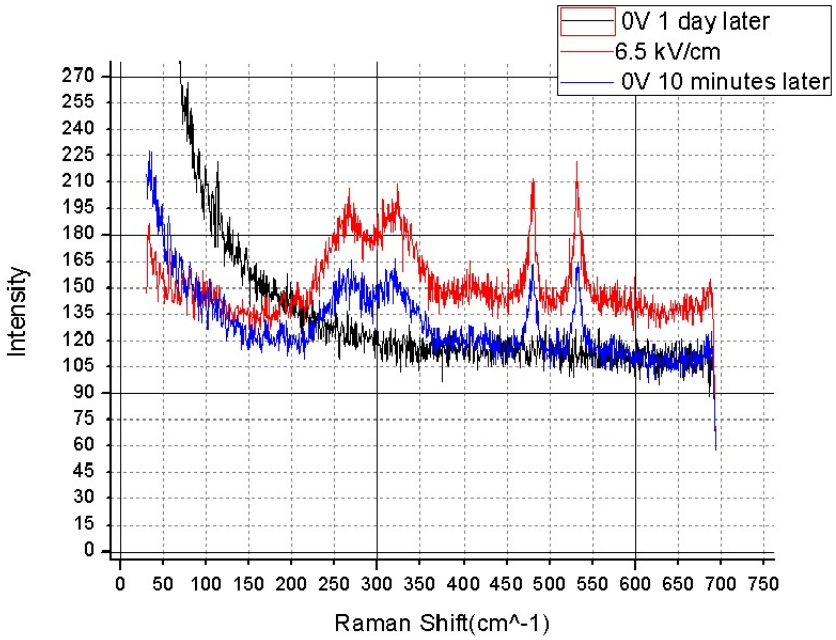

Figure 6.8: Comparison of the spectrum shown in 6.7 after relaxing for 10 minutes and one day without an external electric field. There seems to be an overall decrease of the signal, which eventually fades out one day later.

Polished sample

The other piece of the polycrystalline sample (which had been polished) was never treated before by an external electric field and flowing current. When this piece was exposed to the same high voltage as the unpolished one, the same peaks appeared as shown in figure 6.9 .

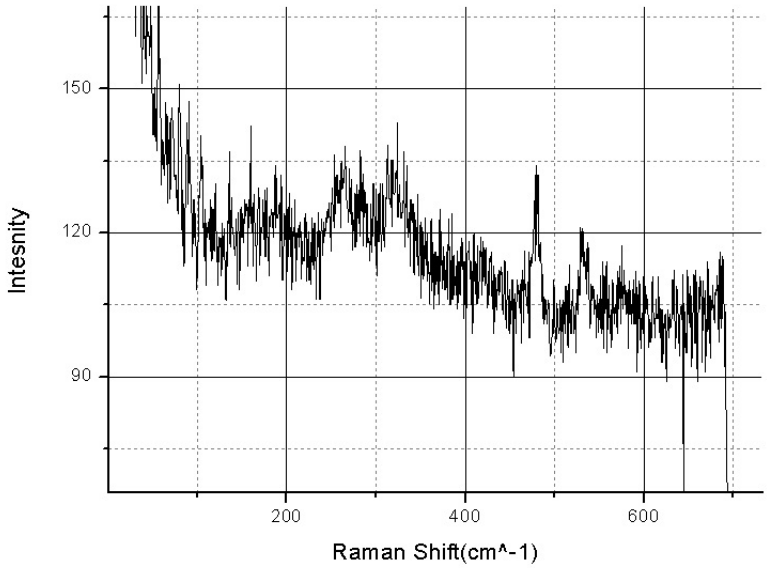

Figure 6.9: The same peaks reappeared in the polished sample too with the application of 6.5 kV/cm and accumulation time $2 \times 300''$.

As we can see in figure 6.10 the signal from the polished sample seems not to fade out as quickly as in the case of the unpolished one. This might have to do with the fact that the polishing procedure had introduced strains inside the sample, which would lead to the pinning of the induced deformations. After two days there were crystallites that did not show any peaks (just like the unpolished sample) but the vast majority did show the same peaks but significantly lowered as shown in figure 6.11 .

The application of the electric field to those crystallines lead to a clear enhancement of the peaks as shown in figure 6.12. This gives us further evidence that the appearance of the peaks is an induced effect.

We conducted low temperature measurements in order to understand how the spectrum is altered due to temperature changes (figure 6.13).What is more interesting is the fact that the $480cm^{-1}$ peak is affected differently from the lowering of temperature than the other ones.

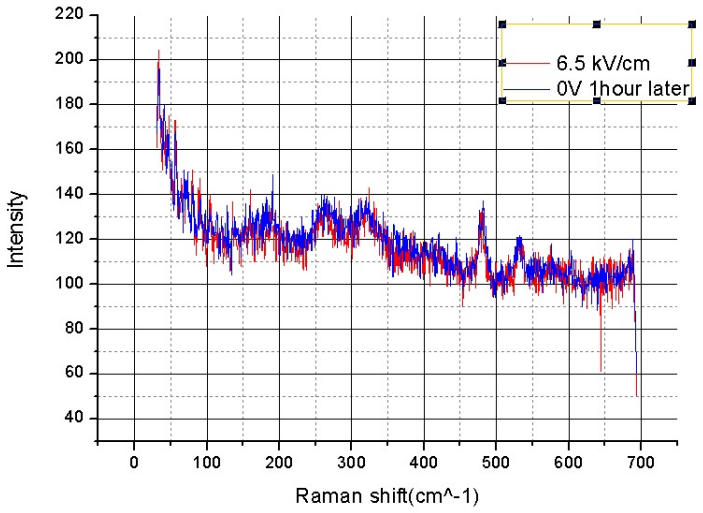

Figure 6.10: The two spectra was obtain from the same crystalline in electric field and one hour later under the same conditions and accumulation time.

The fact that only some peaks were observed for vertical polarization of the incident light (figure 6.14) reflects the different symmetry of the corresponding phonons.

Some strange spectra

In both samples we have detected some surface spots, which gave peculiar spectra (Fig. 6.16). The peaks seemed different from the ones obtained from the rest of the samples. Moreover, those areas were few and localized and they could be identified even by simple inspection by eye under the microscope due to the slightly different color and texture from the original one. Those areas had not been observed prior to the application of the high voltage, they might be secondary phases of the material, which might brought up by the electric field (due to symmetry constrains) or they might be local chemical changes, which were a byproduct of the application of a high electric field. Although quite a few of the peaks from those spectra (especially from spectrum c) seems to have some relevance, especially with the peaks that we expect from the orthorombic and rombohedral phase (figure 6.26), the fact that we could not detect them except from specific spots called for further investigation. Also they did not present any alternation with time or application of the electric field. This static character further enhances our thoughts of a local alternation or a secondary phase.

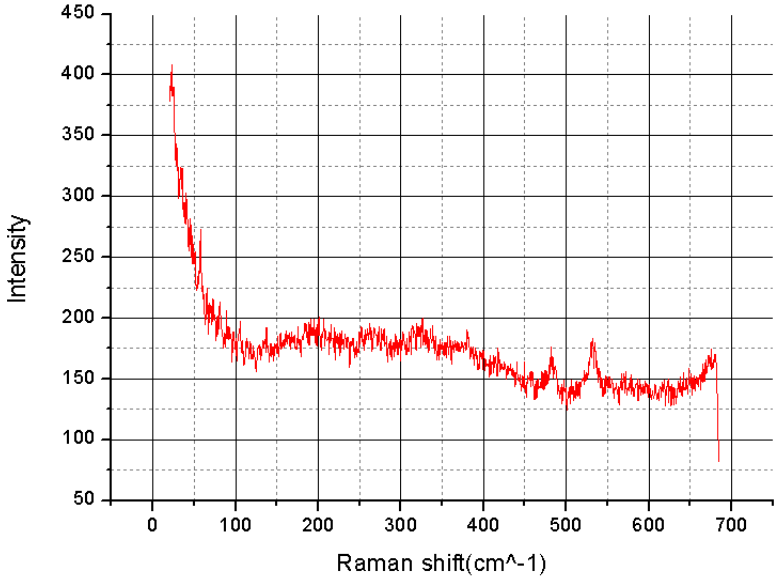

Figure 6.11: Two days after the system relaxed but the peaks are still observable.

Single crystal

Due to the fact that we did not know the crystallographic orientation of the faces of the single crystal we tried different orientations in order to find the appropriate alignment with the electric field. When the electric field was applied, the sample was turning again until its polarization was aligned with the field. The spectra that we got are in figures 6.17-6.20. We see that the spectra are not the same as the polycrystalline was. Despite that the appearance of peaks in the spectrum enhances the odds that we have electric field induced Raman scattering but also demands explanation about the discrepancies between the spectra of the two samples. The fact that different orientations of the crystal gave us different peaks may be explained by the fact that the selection rules would allow only specific phonons to be measured each time depending of the relevant orientation of the crystal axis with respect to the polarization of the incident light. We see that the peaks that appeared are not so intense as the ones in the polycrystalline sample. This means that the induced effect is weaker in the single crystal than the pollycrystalline sample. Also the fact that this sample is also polished gives longer relaxation time due to the pinning of the deformations from the microstrains in the sample.

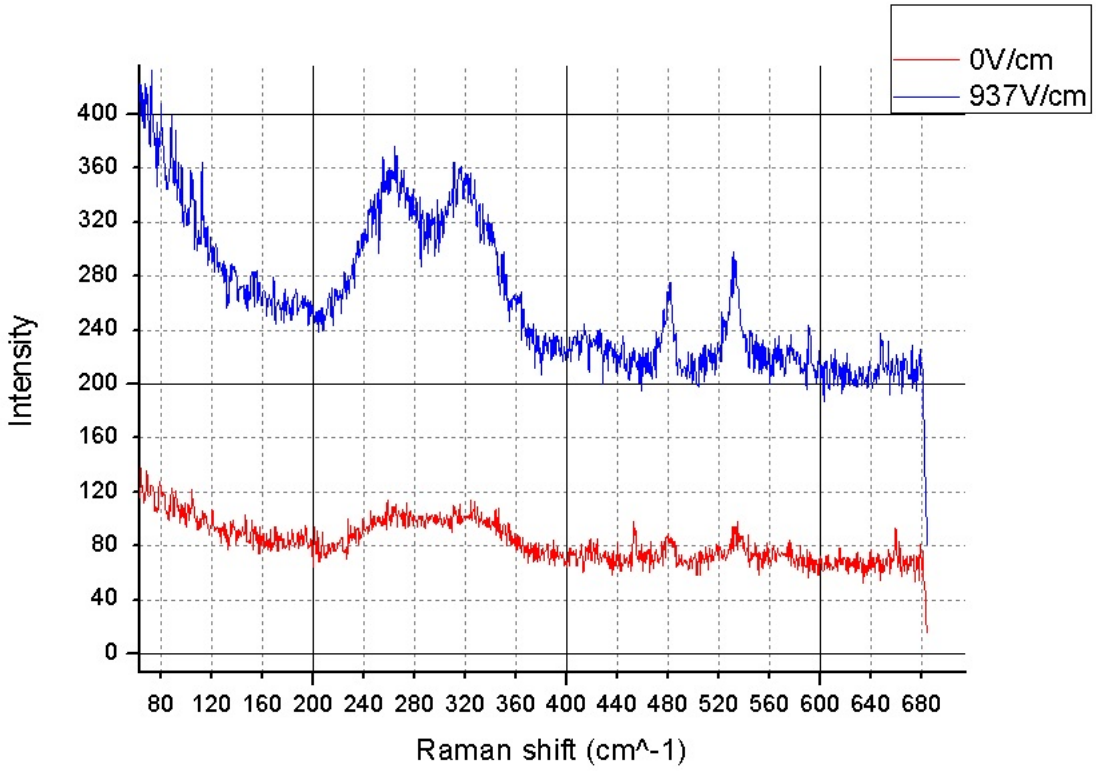

Figure 6.12: We can see that the effect reappears with the application of an electric field. The accumulation time and the conditions in general are the same for the two spectra. We also observe that now the $480cm^{-1}$ peak is not stronger than the $532cm^{-1}$ as it were in the initial spectra of the polished sample. This means that the orientation of the crystalline determines the relative strength of the peaks

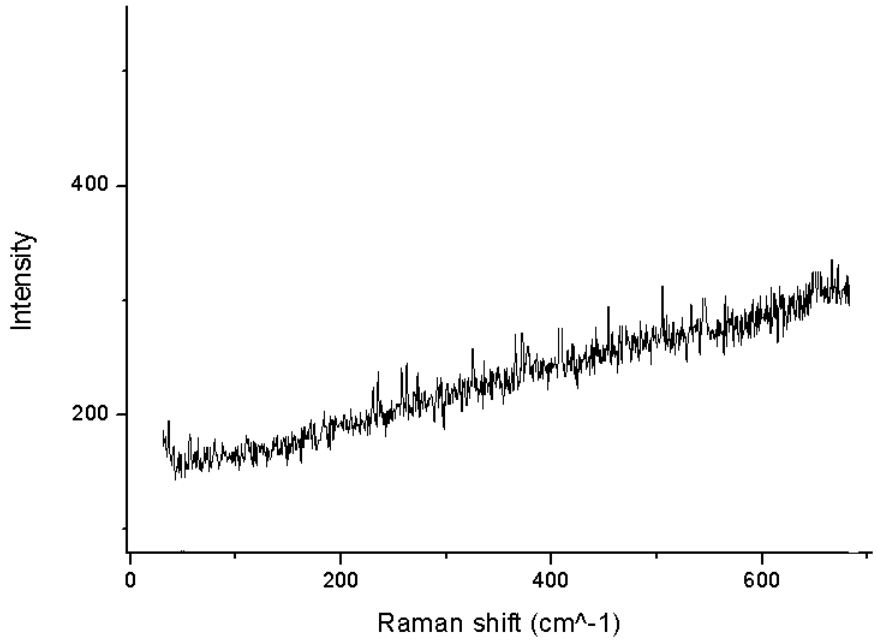

Figure 6.13: The low temperature measurements revealed that the $\sim 260cm^{-1}, \sim 321cm^{-1}$ have different temperature dependence from the rest of the peaks. The relative intensity of the two remaining peaks increases significantly with the $480cm^{-1}$ being the strongest. The accumulation time was $2 \times 1200''$

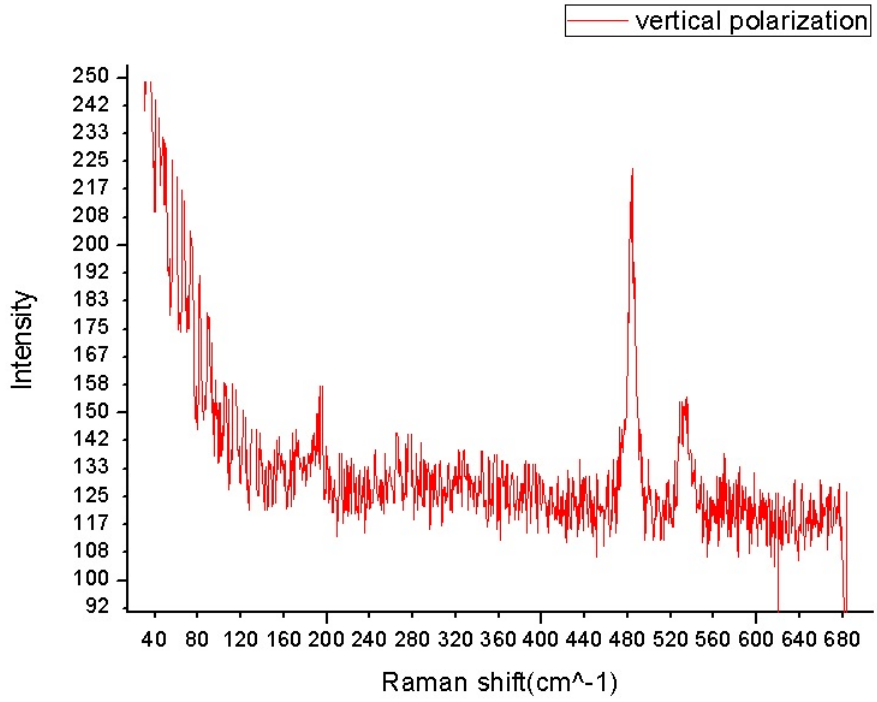

Figure 6.14: Spectrum of the same spot with vertical polarization of the incident light. We can see that only the $480cm^{-1}$ and $532cm^{-1}$ "survive" also a peak at $\sim 193cm^{-1}$ is visible. This peak is also barely detectable in some previous spectra such as in Figs 6.9 and 6.10. The accumulation time was $1 \times 1200''$.

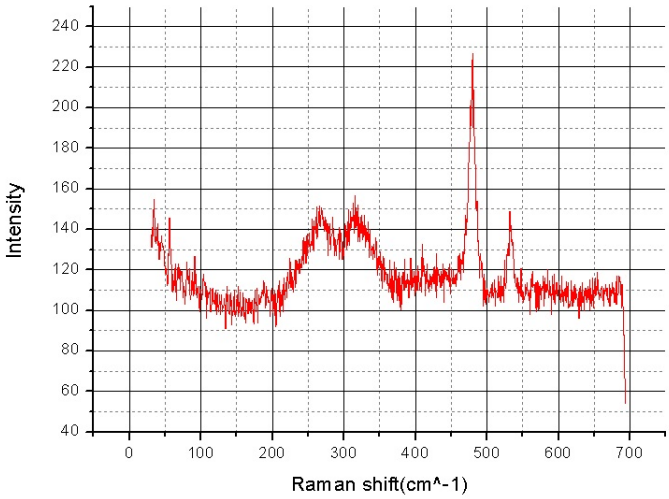

Figure 6.15: Different spot from the polished sample which gives better signal from the initial one. Comparing these with the corresponding spectra from the unpolished sample we also see that the third peak is intenser from the other ones in the polished sample. This discrepancy might be a hint that this peak has a different origin than the other ones.

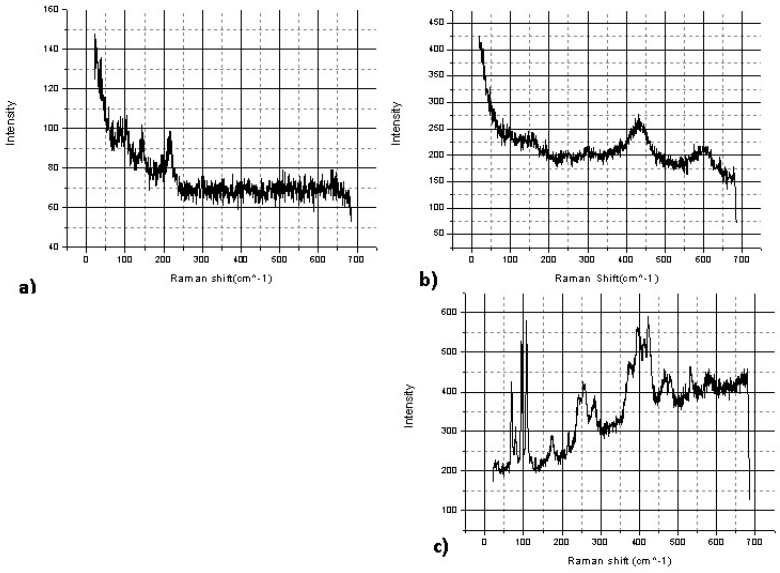

Figure 6.16: Spectra obtain from both samples which might belong to phases different from the main one.

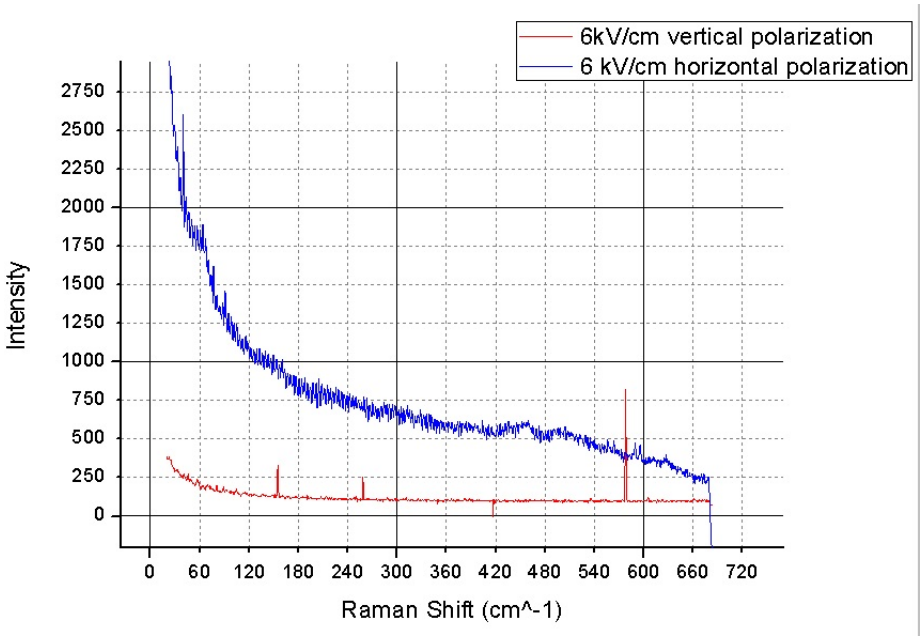

Figure 6.17: Different orientation of the crystal, different spot. The discrepancy between the horizontal and vertical polarization is striking. The $\sim 65cm^{-1}$ peak seems like the soft mode but it has very low frequency for ambient conditions.

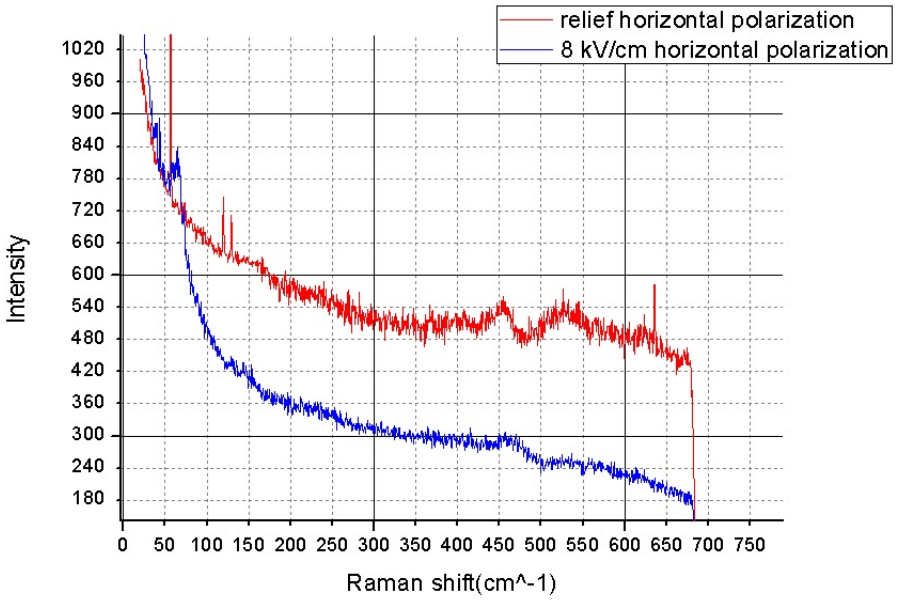

Figure 6.18: In comparison with figure 6.17 we see that the $65cm^{-1}$ peak disappears in the relief process something that points out that it might be induced by the electric field.

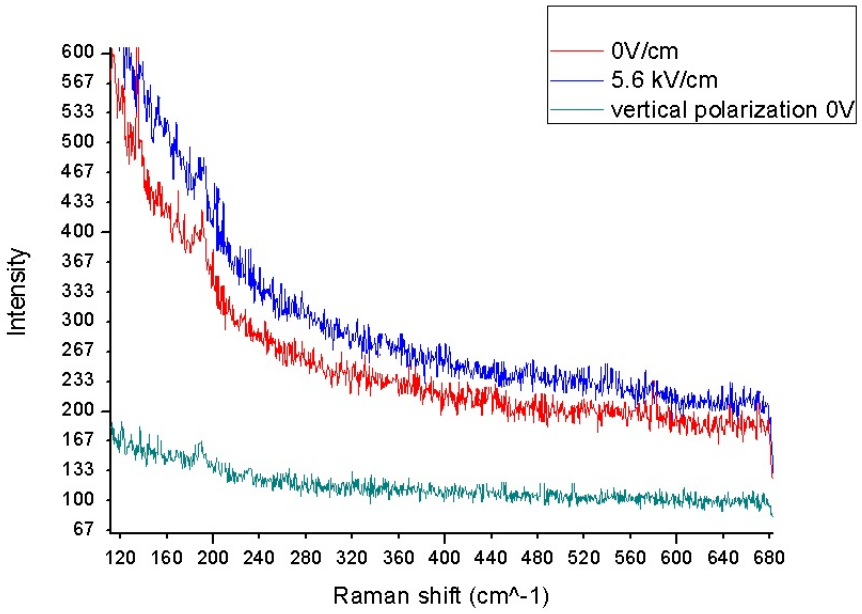

Figure 6.19: Spectrum from the single crystal material. We can see the $193cm^{-1}$ peak observed also in the precious samples and there is a hint of the $480cm^{-1}$ peak in the spectrum with the 5.6 kV/cm field. The rotation of the incident light polarization reduced the signal as expected, but the $193cm^{-1}$ peak 'survived' again. The accumulation time was 2×1200

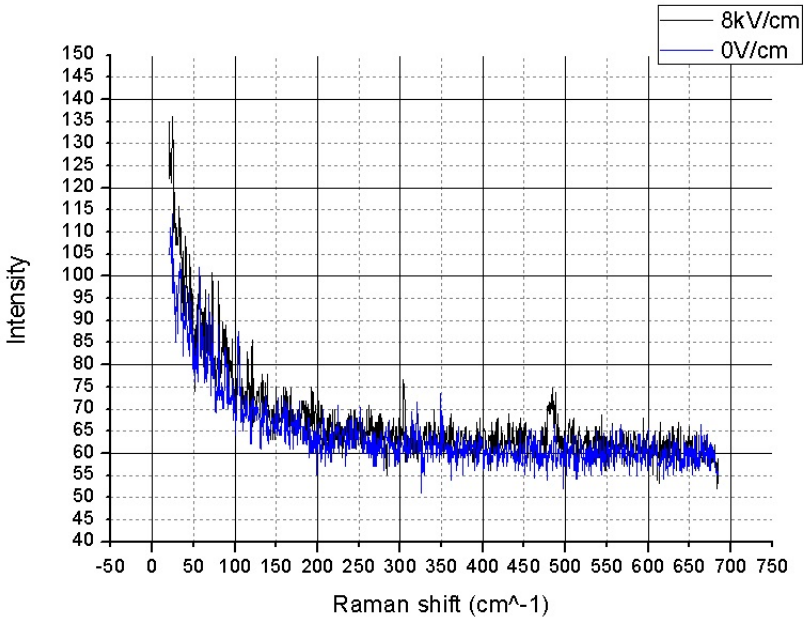

Figure 6.20: Vertical polarization. One spectrum was taken with no field and accumulation time 2 ×1200" and the other one with ∼8kV/cm and accumulation time 2 ×600". We see that the difference in the accumulation time the intensity of the signal is equal and there seems to appear a peak at $\sim 480 cm^{-1}$ similar to the one we saw in the polycrystalline sample.

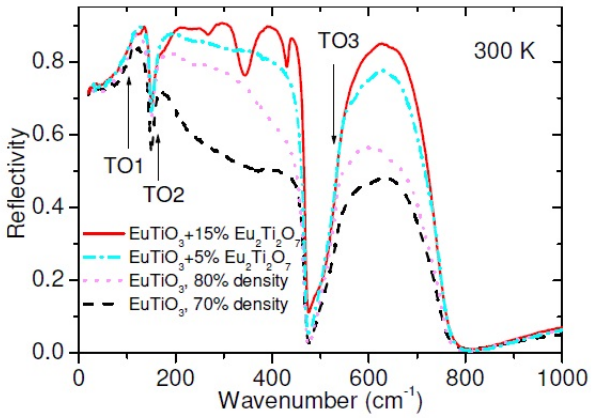

Figure 6.21: Reflectivity measurements of $EuTiO_3$. We can see that we expect the third transverse optic phonon at $\sim 480cm^{-1}$ and the second one at $\sim 180 - 190cm^{-1}$. The first one (which is also the soft mode) is rather weak and it has lower frequency $\sim 110cm^{-1}$ at ambient conditions. The rest of the peaks $310cm^{-1}, 400cm^{-1}250cm^{-1}$ belong to the pyroclore phase of the material $Eu_2Ti_2O_7$ [7]. More recent studies [20] have revealed that those peaks do not originate from the secondary pyrochlore phase but the TO1 and TO4 modes split at low temperatures and generate those new peaks.

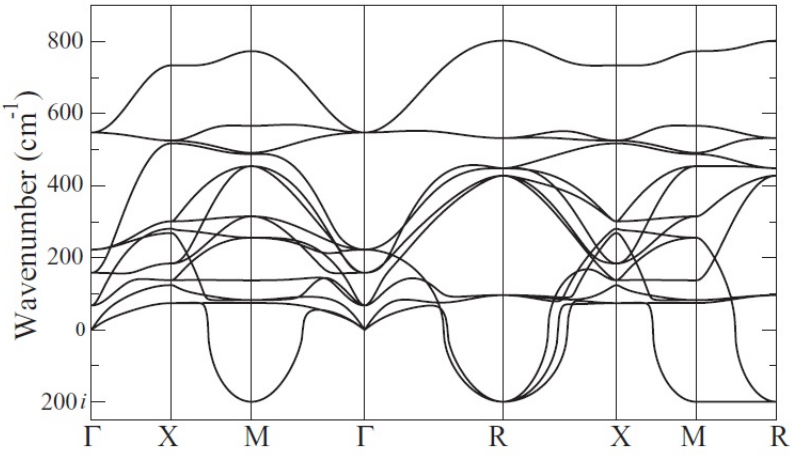

Figure 6.22: Dispersion curve for the cubic $Pm\bar{3}m$ structure [21]

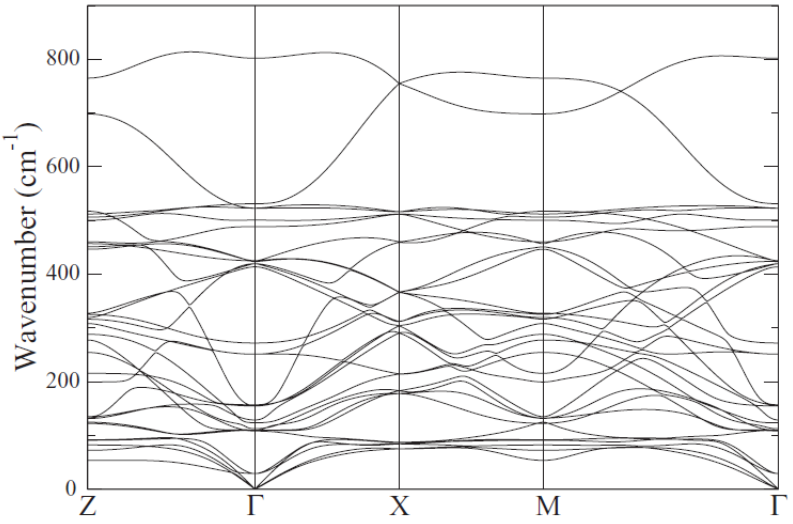

Figure 6.23: Dispersion curve for the tetragonal I4/mcm structure [21]

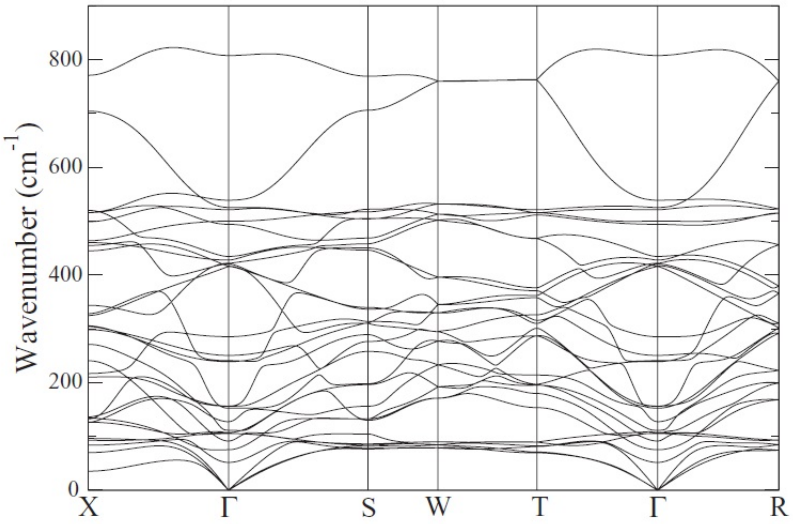

Figure 6.24: Dispersion curve for the orthorombic Imma structure [21]

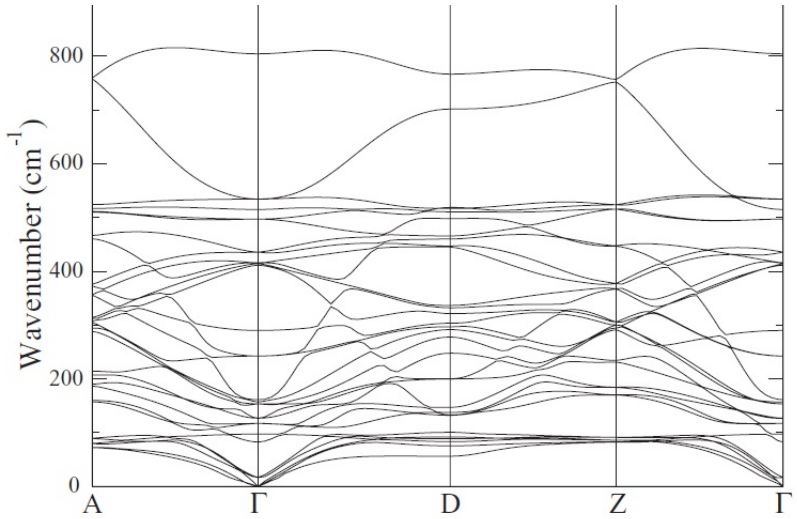

Figure 6.25: Dispersion curve for the rombohedral R$\bar{3}$c structure [21]

Modes (cm^_1)	Unpolished	Polished	Single crystal	Highpressure	Cubic theoritical	Tetragonal theoritical	Orthorombic theoritical	Rombohedral theoritical
1							36	
2			65		(F1u)67		40	
3							98	80
4							104	
5						107	106	
6							110	
7							110	
8						128	131	124
9						154	154	153
10					(F1u)155	156	155	
11							159	160
12	196	196	193			164	164	164
13							237	
14	268	268				251	249	242
15	323	323					283	
16							413	
17							414	
18							416	
19	420	420				419	418	419
20							424	
21			450				436	
22	480	480					491	
23							499	
24							516	514
25						523	523	
26	532	532	533		(F1u)537	531	537	533
27						802	801	803

Figure 6.26: This table shows the observed peak frequencies and the calculated phonon frequencies in the Γ point of the Brillouin zone for each one of the proposed crystal systems. The frequncies were calculated from the dispersion curves of each crystal system. [21]

6.4 Discussion

First of all the fact that some kind of change in the material was introduced with the application of the electric field is obvious (for example the comparison of figures 6.6 and 6.7 give us an idea of this change). Both samples were thoroughly checked before the experiments and neither had shown any peaks in their spectrum, as expected, so these peaks are induced from the field. The fact that those peaks were shown from a number of different crystallites, which were chosen randomly and they did not share any special characteristic, implies that those peaks must not descent from an impurity or some secondary phase of the material. If all those peaks were from a secondary phase then crystallites, which show them, should not be found so frequently and so unbiased. In figure 6.7 we see that there are five peaks detectable at $\sim$ 268 cm^{-1}, 323 cm^{-1}, 400 cm^{-1}, 480 cm^{-1}, and 532 cm^{-1}. From those the 480 and 532 peaks are narrow and intense so they are definitely first order lattice scattering. The other peaks are broader but this is not enough to decide whether they are second order scattering. Also if we see figure 6.10 a peak at $\sim$190 cm^{-1} is present, which seems rather weak. Figures 6.8 , 6.10 show us that the effect is not permanent and it fades out with time.

The fact that the peaks re-appeared when we applied again the electric field (figure 6.12) states that those peaks are indeed induced and so they do not have to do with same chemical alteration of the sample or any other parasitic phenomenon. But we did not manage to re-induce the phenomenon to the unpolished sample (and also in some crystallites of the polished sample). One possible explanation is that after the total relaxation of the sample there is a permanent effect where the phase with no Raman active phonons is preferable and more stable than before making it harder to re-produce the lattice instability.

Figure 6.13 gives us very useful information about the changes in the relative intensities of the peaks with the lowering of the temperature. From the change of the relative intensities (shown in the following table) between the peaks, taken with respect to the 480 cm^{-1} peak, we can see that all peaks are enhanced upon cooling except for the 190 cm^{-1} and the 400 cm^{-1} peaks. Also the 480 cm^{-1} is the most intense peak at 77 K. Taking also into account the relative reducement of the 190 cm^{-1} 400 cm^{-1} and we can say that those two peaks seem to have different mechanisms from the rest of the peaks.

Temperature	190 cm^-1	268 cm^-1	323 cm^-1	400 cm^-1	480 cm^-1	532 cm^-1
300 K	1.73	1.22	1.22	1.68	1	1.09
77 K	1.27	1.29	1.28	1.53	1	1.28

Figure 6.14 corresponds to a vertical polarization of the incident light. We can see that the 480 cm^{-1} and 190 cm^{-1} peaks had been enhanced in comparison to the rest (the 268-323 cm^{-1} have almost vanished). In general we can say that the data from the polycrystalline sample show us that an applied electric field can induce Raman scattering. The expected TO4 phonon has been detected with good agreement (in comparison with the IR measurements) to its frequency and we have strong indications that the TO2 phonon has been detected but in this case we have a significant difference to its frequency (up to $\sim$ 20 %) with respect to the frequency measured with other techniques.

The spectra obtained from the single crystal (figures 6.17-6.20) are different from those obtained from the polycrystalline sample. The application of the electric field revealed peaks that were not seen before. The 65 cm^{-1} (figure 6.17) disappears when the polarization is vertical. This resembles the behavior that we expect from the soft mode but with much lower frequency than we expected (110 cm^{-1} at ambient conditions). In figure 6.18 we can see that the 65 cm^{-1} peak is not present when the samples is relaxed.

In figure 6.19, which corresponds to a different orientation of the crystal with respect to the electric field, we see a 190 cm^{-1} peak, as the one seen to the polycrystalline sample. This had been induced by the field. After the removal of the voltage the peak did not disappear at once and by the re-application of the field it did not change significantly. At this point we have seen that by trying different orientations of the crystal we detected two polar phonons that might be the two lowest transverse optic phonons. In figure 6.20 we see that another peak was induced (for a third orientation of the crystal) which is at $\sim$ 482 cm^{-1}. This resembles the expected TO4 mode, the two wavenumber difference is insignificant and can by explained by miscalibration of the instrument.

The fact that the single crystal had much better quality gave us spectra with no secondary phases and parasitic effects. In contrast, the spectra in figure 6.16 (of the polycrystalline sample) should be from secondary phases or local chemical changes of the sample because they were found in specific spots which shared different characteristics from a normal crystalline of the sample. Also the electric field did not affect them. If there were indeed secondary phases of the sample one could think why they had not been detected before the high voltage experiments. A possible explanation is that those secondary phases have the same symmetry, which means that they do not have Raman active phonons and eventually the application of the electric field revealed them as well as the main phase.

In Figure 6.26 we can see a comparison of the frequencies of the modes from our spectra from the expected ones for each one of the potential crystal

structure. We can see that there is a similarity especially with the modes of the tertragonal and orthorombic phase. The 532 cm^{-1} 268^{-1} and 420^{-1} and 480 $^{-1}$ peaks have good agreement with the expected values. The 196 and 323 peaks differ significantly the the theoretical values that can be matched. If we have indeed seen the Raman spectrum of $EuTiO_3$ this discrepancy can be explained by a modulation of those modes frequencies by the applied electric field. This effect hints that those modes correspond to movements of ions with different valencies, which leads to strong coupling of those modes with the field. Also what is very interesting is the 65 cm^{-1} peak in the single crystal sample which resembles the frequency of optic soft mode of the cubic structure but in low temperatures. A better match of this mode might be the orthorombic 74 cm^{-1} mode.

6.5 Conclusions

In our study we show that the application of an external high electric field induced a symmetry lowering of the crystal structure which allowed us to acquire its Raman spectrum. We believe that those spectra did not come from a secondary phase of the material because they had not been observed prior the application of the electric field and they show signs of an induced effect (reappearance in the polished sample). Also the fact that those spectra were acquired from different (not special or peculiar) spots on the sample make us thing that they are not some irrelevant impurities and secondary phases. Also the fact that the peaks that we observed showed dynamic behavior (they changed with time) makes the case of a large scale chemical alternation of the sample due to the electric field unlikely. What is very interesting is the fact that we were not able to see the antiferrodistortive phase transition with the lowering of the temperature despite the fact that there are quite a few other experiments (with x-ray diffraction etc) which confirm the existence of this phase transition.

We make the hypothesis that at ambient conditions the cubic, tetragonal, orthorombic, and rombohedral phases coexist. As the energy difference between them is comparable [21] to the thermal energy the structure of the material fluctuates dynamically between these four structures. So nanodomains are formed at ambient conditions and the fluctuations between the four different structures make this dynamic effect very difficult to be observed with Raman spectroscopy. So the crystal seems as if it has perfect cubic structure. When we applied an electric field, due to the antagonism between the antiferrodistortive transition and the displacement of the titanium anions [26] there would be a formation of larger domains with the tetragonal axis

oriented perpendicular to the field. The electric field drives the system towards the formation of larger domains where the low symmetry structures dominate and are fairly static. This hypothesis explains the fact that there were spots that seemed to undergo structural transitions and others that did not maybe due to 'bad' alignment between the crystallographic axis and the electric field at those crystallites. But we can not explain why when the crystal (especially the unpolished one) was relaxed fully we could not re-induce the effect. Maybe there is a permanent alternation in the structure of the sample, with the cubic becoming more stable than the other phases and consequently being strongly preferred .

We tried to obtain IR spectra in order to 'see' if something changes in the IR spectrum after the application of the electric field. The low reflectivity of the sample did not allow us to have conclusive results. Also more extensive high pressure measurements would give us better insights to the antiferrodistortive phase transition.

Bibliography

[1] J.A Koningstein:Introduction to the theory of the Raman Effect.D.Reigel Publishing Company (1972)

[2] Max Born Kun Huang:Dynamical Theory of Crystal Lattices. Clarendon press Oxford

[3] W.Cochran: The Dynamics of Atoms in Crystals.Edward Arnold

[4] William Hayes Rodney Loudon: Scattering of Light by Crystals. John Wiley and Sons(1978)

[5] Daniel Khomskii: Classifying multiferroics: Mechanisms and effects. American Physical society(2009)

[6] T. Katsufuji Y. Tokura. Transport and magnetic properties of a ferromagnetic metal: $Eu_{1-x}R_xTiO_3$. Physical Review B. Volume 60,Number 22 (1999)

[7] S. Kamba D. Nuzhnyy P. Vanek: Magnetodielectric effect and optic soft mode behavior in quantum paraellectric $EuTiO_3$ ceramics. EPL journal, 80(2007)

[8] V. Goin S.Kamba J.Hlinka: Polar phonon mixing in magnetoelectric $EuTiO_3$. The European Physical Journal B 71(2009)

[9] A.Bussmann-Holder J.K*ö*hler R.K Kremer J.M Law: Analogies of stuctural instabilities in $EuTiO_3$ and $SrTiO_3$

[10] S.E Rowley L.J Spalek R.P Smith: Quantum criticality in ferroelectrics

[11] P.A Fleury J.M Worlock: Electric Field-Induced Raman Scattering in $SrTiO_3$ and $KTaO_3$. Physical Review Volume 174, Number 2 (1968)

[12] P.A Fleury J.F Scott and J.M Worlock: Soft phonon modes and the 110 ^{0}K phase transition in $SrTiO_3$. Physical Review Letters. Volume 21, Number 1 (1968)

[13] R.Luzzi: On Magnetism in Insulators. Revista Brasileira de Fisica Vol 3 $N^0 2$ (1973)

[14] P.G Radaelli L.C Chapon: Symmetry constrains on the electrical polarization in multiferroics materials. Physical Review B 76 (2007)

[15] J.L Spalek: Emergent Phenomena Near Selected Phase Transitions. Shoenberg Laboratory for Quantum Matter Cavendish Laboratory and Jesus College Cambridge (2012)

[16] L.D landau E.M Lifshitz: Electrodynamics of Continuous Media Course of theoretical Physics . Pergamon Press

[17] P.Chandra and P.B Littlewood. A Landau Primer for Ferroelectrics. arXiv:cond-mat/0609347v1 (2008)

[18] W. Cochran. Crystal stability and the theory of ferroelectricity. Advances in Physics, 9:36, 387-423.

[19] D.L Rousseau, R.P Bauman, S.P.S Porto. Normal Mode Determination in Crystals. Journal of Raman Spectroscopy, Vol10, 1981

[20] V.Goian, S.Kamba , O.Pacherova. Antiferrodistorsive phase transition in $EuTiO_3$. Physical Review B 86 , 054112 (2012)

[21] Konstantin Z. Rushchanskii, Nicola A. Spaldin and Marjana Lezaic. First Principle predictions of oxygen octahedral rotations in perovskite-structure $EuTiO_3$. Physical Review B 85 104109 (2012)

[22] Jerry L. Bettis, Myuang-Hwan Whangbo, Jureng Kohler, Annette Bussmann-Holder, and A.R Bishop. Lattice dynamical analogies and differences between $SrTiO_3$ and $EuTiO_3$ revealed by phonon-dispersion reletions and double-well potentials. Physical Review B 84 184114 (2011)

[23] D.Bessas, K.Z. Rushchanskii, M.Kacklik, S.Disch, O.Gourdon. Lattice instabilities in $EuTiO_3$. Physical Review B 88 144308 (2013).

[24] Jong-Woo Kim, Paul Thompson, Simon Brown, Peter S.Normile, John A. Schlueter, Andrey Shkabko. Emergent superstructural dynamic order due to competing antiferroelectric and antiferrodistortive instabilities in bulk $EuTiO_3$. Physical Review Letters 110 027201 (2013)

[25] David S.Ellis, Hiroshi Uchiyanna Satoshi Tsutsui, Kinihisa Sugimoto, Kenichi Kato. Phonon softening and dispersion in $EuTiO_3$. Physical Review B 86 220301 (2012)

[26] A.P Petrovic, Y.Kato, S.S Sunku, T.Ito, P.Sengupta, L.Spalek, M.Shimuta, T. Katsufuji, C.D Batista. Electric Field modulation of the tetragonal domain orientation revealed in the magnetic ground state of quantum paraelectric $EuTiO_3$. Physical Review B 87 064103 (2013).

[27] V.V Shvartsman, P.Borisov, W. Kleeman, S.Kamba, T.Katsufuji. Large off-diagonal magnetoelectric coupling in the quantum paraelectric antiferromagnetic $EuTiO_3$.

[28] Turan Birol Craig J. Fennie. Origin of giant spin-lattice coupling and the suppresion of ferroelectricity in $EuTiO_3$ from first principles. arXiv:1305.7201v2

[29] I.A Sergienko E. Dagotto. Role of Dsyaloshinskii-Moriya interaction in Multiferroic perovskites. Physical Review B 73 (2006)

[30] Robert A. Evarestov, Evgeny Blokhin, Denis Gryaznov Eugene A. Kotomin, Joachim Maier. Phonon calculations in cubic and tetragonal phases of $SrTiO_3$: A comparative LCAO and plane wave study. Physical Review B 83 (2011)

[31] Hiromoto Uwe Tunetaro Sakudo. Stress-induced ferroelectricity and soft modes in $SrTiO_3$. Physical Review B volume 13 number 1 (1976)

[32] G.J Conduit B.D Simons. Theory of quantum paraelectrics and the metaelectric transition. Physical Review B 81 (2010)

[33] R.Roussev A.J Millis. Theory of the quantum paraelectric-ferroelectric transition. Physical Review B 67 (2003)